Spring 2013

On the effect of silicon and phosphorus during the precipitation of K-carbide in Fe-Mn-Al-C alloys

Laura Bartlett

Department: Materials Science and Engineering

ON THE EFFECT OF SILICON AND PHOSPHORUS DURING THE PRECIPITATION OF κ-CARBIDE IN Fe-Mn-Al-C ALLOYS

by

LAURA NICOLE BARTLETT

A DISSERTATION

Presented to the Faculty of the Graduate School of the

MISSOURI UNIVERSITY OF SCIENCE AND TECHNOLOGY

In Partial Fulfillment of the Requirements for the Degree

DOCTOR OF PHILOSOPHY

in

METALLURGICAL ENGINEERING

2013

Approved by

David C. Van Aken, Advisor
Kent D. Peaslee
Von L. Richards
Simon Lekakh
Julia E. Medvedeva

PUBLICATION DISSERTATION OPTION

This dissertation has been prepared in the form of four manuscripts for publication. Pages 23-51 were published in the Transactions of the American Foundry Society 2010. Pages 52-89 have been prepared in the style utilized by the Metallurgical and Materials Transactions A. Pages 90-126 have been prepared in the style utilized by the Metallurgical and Materials Transactions A. Pages 127-177 have been submitted to the Transactions of the American Foundry Society 2013. The Introduction and Appendix have been added to provide supplemental information to select experimental procedures and calculations.

ABSTRACT

Implementation of lightweight high manganese and aluminum steels for use in high energy absorbing applications requires a detailed knowledge of how alloying additions and impurities affect age hardening and high strain rate fracture properties. Dynamic fracture toughness is an important design criterion but has not been reported previously in these alloys. In addition, previous studies have shown that silicon and phosphorus increased the strength and aged hardness; however, the mechanism was unknown. This research mainly focuses on the effect of silicon and phosphorus on the precipitation of κ-carbide and alloy partitioning during aging.

Short range ordering, SRO, of Fe-Al-C into relative atomic positions described by the $E2_1$ superlattice structure preceded and occurred concurrent to spinodal decomposition. Short range diffusion of phosphorus increased the kinetics of ordering resulting in a decrease in the time required for subsequent spinodal decomposition and an increase the amplitude of carbon concentration with time. Silicon increased the strength and hardness as a result of increased carbon partitioning into the κ-carbide during aging.

Dynamic fracture toughness was found to depend upon aluminum and carbon. Increasing the amount of solid solution carbon increased the dynamic fracture toughness in solution treated specimens. However, increasing carbon in aged specimens increased the amount of κ-carbide and produced brittle fracture. Additions of aluminum from three to nine weight percent decreased toughness regardless of the heat treatment. Dynamic fracture toughness was a strong function of AlN content. A good combination of high strength and dynamic toughness with a corresponding density reduction of 10 to 12% is obtained with aluminum additions between 6 and 7% and carbon below 1.2%.

ACKNOWLEDGEMENTS

First and foremost, I would like to thank my husband, Chris, for his unwavering support in allowing me to complete this important step in my career. I also appreciate all of the sacrifices my family has made to make it possible for me to finish my degree. It has been my greatest honor to work with my advisor, Dr. David Van Aken, on this project. I am enormously grateful to Dr. Van Aken not only for his outstanding knowledge, dedication, and guidance during the completion of this project but also for helping me to cultivate my professional career. I would also like to thank Dr. Kent Peaslee for serving as my co-advisor for the first few years of my graduate studies and for his tremendous support. Many thanks to Dr. Simon Lekakh who has helped me enormously with my experimentation and thermodynamic modeling. I would like to also thank the rest of my committee members, Dr. Richards and Dr. Medvedeva for their excellent guidance throughout the course of this research. In addition I am very grateful to all of my fellow undergraduate and graduate students for their help with heat treatments and experiments. I would especially like to thank Mr. Jack Jones and Mr. Nathan Inskip for all of their good advice and help with sample preparation. In addition I would also like to thank the U.S. Department of Education for their financial support in awarding me the G.A.A.N.N. I am also very appreciative to Dr. Dieter Ishiem and the Northwestern University Center for Atom Probe Tomography for their help with funding and instruction in completing the 3-D atom probe tomography which was an integral part of my research. I would like to give a special thanks to Dr. Eric Bohannan for his help with x-ray diffraction experiments.

TABLE OF CONTENTS

Page

LIST OF ILLUSTRATIONS

PAPER 2

PAPER 3

PAPER 4

LIST OF TABLES

1. INTRODUCTION

Lightweight steels in the Fe-Mn-Al-C system show great promise as lightweight foundry alloys for use in high energy absorbing applications when tightly controlled for maximum cleanliness. The combination of high work hardening rates, high strengths, and excellent ductility makes these steels very promising for both ballistic and automotive applications. Howell et al.[1] studied the mechanical properties of a cast Fe-30Mn-9Al-1Si-0.9C-0.5Mo steel and determined that this composition meets the Army's MIL-PRF-32269 ballistic requirements and reduced the weight of P900 armor by almost 15%. Aged materials with a nominal composition of Fe-30Mn-9Al-1Si-0.9C-0.5Mo have equivalent tensile properties as quench and tempered 4130 steel with an almost 15% weight reduction.[1] However, in the formerly mentioned study by Howell et al., only variations in the silicon content of cast alloys with a base composition of Fe-30Mn-9Al-1Si-0.5Mo were considered with regard to tensile properties.[1] All compositions in the following text are expressed in terms of weight percent unless specified otherwise. Silicon is added to improve castability and silicon decreases the melting point by 30C°/wt.%Si.[2] Adding silicon has additionally been reported to stabilize $D0_3$ and B_2 iron aluminide precipitation and to prevent or severely retard the precipitation of brittle β-Mn, which is deleterious to impact toughness in age hardened materials.[3] Increasing silicon in cast alloys has been shown to increase the strength and hardness of aged alloys. Bartlett et al. reported a 50 to 70 MPa increase in the yield and ultimate tensile strengths of a Fe-30Mn-9Al-0.9C-0.5Mo alloy as the amount of silicon was increased from 1 to 1.56% Si.[4] The exact mechanism by which silicon increases hardness and prevents β-Mn in these steels is a subject of debate. Acselrad et al. reported that silicon increases the kinetics of

zone formation during spinodal decomposition.[3] Although no mention was made on the composition of homogeneously precipitated κ-carbide, they proposed that silicon partitions manganese from the austenite matrix into grain boundary κ-carbide during aging, preventing β-Mn formation.[3] In a later study by Acselrad et al., it was reported that increasing silicon to 1.4% shifted the boundary for high temperature (< 700°C) nucleation and growth of κ-carbide to shorter times and this was suggested to be the result of silicon increasing the activity of carbon in solid solution austenite.[6] An atom probe tomography study of lamellar κ-carbide in a mostly ferritic Fe-1.2C-3.2Mn-10Al (in at.%) steel by Seol et al.[5], revealed that the κ-carbide was manganese rich. They suggest that the partitioning of alloying elements in the κ-carbide is dependent on the abutting phase and that manganese substitution for iron would make the κ-carbide harder and stronger because of stronger bonding between Mn-C couples in comparison to Fe-C pairs.[5]

Phosphorus sharply increases the aged hardness but in levels greater than 0.006%, phosphorus can reduce the notch toughness by 80%.[7] Ab initio calculations showed that phosphorus substitutes for aluminum atoms in the κ-carbide structure and produces open volume defects along <100> contributing to a 45% reduction in the cleavage stress.[8] However, no direct evidence on the effect of silicon addition or impurities such as phosphorus on the size, composition, and morphology of κ-carbide has been reported. Most studies concerning mechanical properties of age hardenable lightweight steel have centered around slight variations of the fully austenitic composition of Fe-30Mn-9Al-1Si-0.9C-0.5Mo because at this composition these steels are almost 15% less dense and have properties that are equivalent to or exceed that of Q&T 4130 castings.[1,4] High strengths

of up to 1000 MPa with total elongations of 35% and room temperature CVN breaking energies greater than 135 J have been reported for aged low phosphorus (<0.007%P) cast steels of the Fe-30Mn-9Al-1Si-0.9C nominal composition.[4,7]

Aluminum has been shown to decrease the work hardening rate in both wrought and cast steels as evidenced by tensile tests.[9,10] Lai et al.[9] studied the tensile properties of solution treated and quenched Fe-30Mn-0.8C alloys with regard to aluminum additions of 0, 5, and 8.5%. The results of are shown in Table 1.1. Increasing the amount of aluminum to 8.5% slightly increased the 0.2% offset yield strength but decreased the ultimate tensile strength by almost 200 MPa. Adding aluminum decreased the elongation by 14% and decreased the amount of work hardening as determined by the difference in the ultimate and yield strengths.

Table 1.1. Tensile properties of solution treated Fe-30Mn-0.8C alloys with different aluminum contents as reported by Lai et al.[9]

Percent Al	UTS, MPa	YS, MPa	Elongation, %	$\Delta\sigma$, MPa
0	993	423	72	168
5	841	435	59	124
8.5	814	440	58	106

Chang et al. studied the effects of solid solution carbon content on the tensile and fatigue properties of a wrought Fe-30Mn-9Al-(0.26-1.1)C steel.[11] The results are shown in Table 1.2. Increasing the amount of carbon in solid solution from 0.2 to 1.1% simultaneously increased both the strength and ductility.[11]

Table 1.2 Tensile properties of a Fe-30Mn-9Al alloy as a function of solid solution carbon content[11]

Percent carbon	UTS, MPa	0.2% YS, MPa	Total Elongation, %
1.06	888	552	59
0.60	786	390	51
0.26	784	472	35

There have been limited studies on the effect of aluminum and carbon on the high strain rate fracture of these alloys. For a given composition, high strain rate fracture in Fe-Mn-Al-C steels is mainly dependent on heat treatment and cleanliness.[4] Age hardening sharply reduces toughness and promotes both transgranular and intergranular cleavage fracture which is associated with κ-carbide precipitation as well as precipitation of grain boundary intermetallic phases.[12] Notch toughness of high strength steel under impact loading has traditionally been characterized by the CVN breaking energy, which is only a qualitative measure of high strain rate toughness. To qualify lightweight Fe-Mn-Al-C steels for high energy absorbing applications, knowledge of the high strain rate fracture toughness, or dynamic fracture toughness, in the presence of a sharp crack is desired.

There are two main objectives of this research. The effect of silicon and phosphorus on the precipitation and composition of κ-carbide will be investigated utilizing hardness measurements, transmission electron microscopy, X-Ray diffraction, and 3-D atom probe tomography in order to understand the mechanism of increased hardening with silicon and phosphorus content. Dynamic fracture toughness will be evaluated with respect to composition, heat treatment, and cast cleanliness.

2. LITERATURE REVIEW

Research in the development of Fe-Mn-Al-C steels began in the late 1950's with the work of Ham and Cairns.[13] These early Fe-Mn-Al-C steels utilized aluminum with the goal of improving corrosion resistance and providing a cost saving alternative to Cr-Ni stainless steels. Aluminum also reduces the density, making Fe-Mn-Al-C steels 12-18% lighter than traditional steels.[14] The high manganese and carbon contents, which usually range from 20 to 30% and from 0.7 to 1.2%, respectively, stabilize an austenitic matrix with less than 15% δ-ferrite.[1] In the solution treated condition, these alloys have excellent ductility with greater than 80% true fracture strain and tensile strengths in the range of 800 MPa.[14,15] Alloys that contain greater than 5% aluminum and 0.3% carbon are age-hardenable.[1,13,16] In the age hardened condition, these lightweight steels display a wide range of mechanical properties with recently recorded cast tensile strengths as high as 1,085 MPa.[1] Aged hardened wrought tensile strengths as high as 1,210 MPa have been reported by Acselrad et al.[17] In the solution treated and cold worked condition these steels can reach strengths greater than 2 GPa.[18] Notch toughness of Fe-Mn-Al-C steel decreases with the precipitation of κ-carbide during age hardening. Solution treated notch toughness values as high as 220 J/cm^2 at room temperature were reported for a cast Fe-30Mn-9Al-0.9C-1Si-0.5Mo steel with less than 0.007% P.[7] Aging produces a reduction in notch toughness and a tendency toward brittle fracture by cleavage. The room temperature Charpy V-notch (CVN) impact energy decreased to 115 J/cm^2 for the formally mentioned steel that was aged for 10 hrs at 530° C. Although these steels will undergo a ductile to brittle transition, an average Charpy impact energy of 39 J/cm^2 at -40° C is obtainable in the aged condition with phosphorus contents of 0.006% or below.[7]

Thus, the mechanical properties and especially the toughness associated with lightweight steels in the Fe-Mn-Al-C system are a function of age hardening. The following is a literature review of age hardening in the Fe-Mn-Al-C system and the effect of variables such as composition and heat treatment on toughness.

2.1. AGE HARDENING

Fe-Mn-Al-C steels with greater than 5% Al and 0.3% C are age hardenable when heat treated in the range of 400 to 700°C.[16] During aging, the increases in strength are the result of homogeneous and coherent precipitation of nano-sized κ-carbide.[3,6,15,19] κ-carbide, $(Fe,Mn)_3AlC_x$, has the $E2_1$ crystal structure in which aluminum occupies corner positions, iron and manganese occupy face positions, and carbon is at the body center interstitial octahedral site.[1,6,20] κ-carbide is known to have a cube orientation relationship with the austenitic matrix with $<100>_\kappa//<100>_\gamma$ and $\{001\}_\kappa//\{001\}_\gamma$[3,15,19,21,22]

The first step in the age hardening process is solution treatment. Solution treatment is performed to dissolve any carbide that may be present in the as-cast alloy in addition to reducing or eliminating ferrite in the microstructure. Goretskii and Gorev studied the structure and equilibrium phase constitution of Fe-(20-25)Mn-10Al-(0.4-1.4)C alloys.[23] They determined that for compositions of Fe-30Mn-10Al-(0.9-1.2)C, isothermally holding at a temperature above 900° C produced a fully austenitic microstructure.[23] However, most researchers have used a solution treatment temperature of greater than 1000° C with holding times of 2 hrs or greater for better homogenization.[1,4,6,16,19,21,24]

Solution treatment is followed by a rapid water or high pressure gas quench. Fe-Mn-Al-C steels have similar quench sensitivity as age hardenable aluminum alloys and a rapid quench is necessary to prevent heterogeneous κ-carbide precipitation on grain boundaries that would lead to a commensurate loss in notch toughness. Howell[7] studied the quench sensitivity of a Fe-30Mn-9Al-1Si-0.9C-0.5Mo alloy and found that reducing the cooling rate increased both matrix and dendrite boundary precipitation and this was correlated to an increase in the quenched hardness and a decrease in the room temperature notch toughness. Howell[7] found that phosphorus had the greatest influence on notch toughness in solution treated alloys and that increasing the amount of phosphorus from 0.006% to 0.07% P decreased the room temperature notch toughness from 190 to less than 35 J for specimens quenched in water corresponding to the maximum cooling rate of 337 °C/s.

Subsequent age hardening is typically performed in the temperature range of 400 to 700° C.[16] Acselrad et al.[6] performed a comprehensive study of phase transformations in a Fe-28Mn-8.5Al-1C-1.25Si. They determined that homogenous precipitation of κ-carbide occurred via spinodal decomposition of the austenite matrix before heterogeneous grain boundary precipitation at temperatures below 700° C.[6] For temperatures greater than about 700° C, the system shifts such that higher concentrations of carbon and aluminum are soluble and precipitation of κ-carbide occurs by a mechanism of nucleation and growth with discontinuous precipitation of κ-carbide occurring over grain boundaries for isothermal holds greater than about an hour.[6] Hale and Baker[19] in their study of a Fe-30Mn-8Al-1C steel report both fine grain boundary κ-carbide precipitates and precipitate free zones developing during aging after only 30 min at 600° C.

To avoid widespread grain boundary precipitation and a reduction in mechanical properties, most researchers have used an aging temperature of 550° C or below.[1,4,7,12,25] Both Hale and Baker[19] and Kayak[16] suggest that the optimum aging treatment for alloys of composition Fe-(25-30)Mn-(8-10)Al-1C resulting in high strength and good ductility with strengths in the range of 830 to 1050 MPa and elongations of 10 to 25% can be achieved by aging for 16 hrs at 550° C. In their study of a cast Fe-30Mn-9Al-(1-1.6)Si-0.9C-0.5Mo (< 0.003% P) alloy, Bartlett et al.[4] used a lower aging temperature of 530° C to obtain strengths as high as 1000 MPa with total elongations of up to 30% for specimens aged from 20 to 60 hrs.

There is some ambiguity in literature as to the exact stages leading to the formation of κ-carbide. It is generally accepted that first stage hardening in Fe-Mn-Al-C alloys is the result of compositional modulation that is accomplished by spinodal decomposition into carbon rich[17,22,26,27] or carbon and aluminum rich[3,6,15,21] and depleted zones followed by ordering of carbon and aluminum into the $E2_1$ κ-carbide structure. The initial precipitates are cuboidal, but with continued aging the κ-carbide coarsens into elongated rectangular prisms along austenite <100>. Han and Choo[25,28] studied the homogenous precipitation of κ-carbide in Fe-33Mn-8Al-0.9C alloys and reported the precipitation sequence to be compositional modulation of carbon, followed by ordering of aluminum into a metastable $L1_2$ superlattice structure, and subsequent precipitation of equilibrium κ-carbide with the $L'1_2$ structure. It should be noted that $L'1_2$ is the nomenclature used by some studies to describe the ordered κ-carbide structure and it is identical to the $E2_1$ structure. Ferrite and β-Mn precipitation at grain boundaries was observed after extended aging times.[25,28]

In contrast, Sato et al.[21] studied phase transitions in Fe-(30-34)Mn-(11.8-4.9)Al-(0.5-1.0)C alloys and determined that spinodal decomposition involving carbon and aluminum was the initial decomposition stage followed by concurrent ordering of aluminum and carbon into the $L'1_2$ κ-carbide structure. Other studies have observed $L'1_2$ superlattice reflections in the as-solution treated and quenched state suggesting the carbon and aluminum ordering takes place previous to all other stages of decomposition.[6,29,30] Choo et al.[29] studied austenite decomposition in a Fe-30Mn-7.8Al-1.3C steel and reported the presence of superlattice reflections in the as-quenched state. Sidebands around main austenite reflections, which are an indication of spinodal decomposition, were not observed until after 10 min of aging at 550° C.[29] Additionally, in a study by Karakishev et al. evidence was shown of $E2_1$ superlattice reflections in an as-quenched Fe-29Mn-9.3Al-0.95C-0.71W-0.42Nb-0.37Mo steel and using nuclear gamma resonance methods, they showed SRO of aluminum in solution treated austenite.[31] It has been suggested that short range ordering is responsible for the absence of an incubation time during the first stage of age-hardening (spinodal decomposition).[6] Additionally, work by Medvedeva et al.[32] shows by first principles calculations that ordering of Fe-Al-C corresponding to the $E2_1$ structure is energetically favorable in solid solution austenite. In another study, Prodhan and Chakrabarti[33] utilized XRD and electron microscopy to study Fe-30Mn-(5-10)Al-(1.5-1.7)Si-(0.91-2.7)C cast alloys aged from 500 to 800 C.

They reported several peaks in hardening curves and concluded that precipitation took place first by ordering into a $L1_2$ Fe_3Al superlattice followed by carbon ordering and precipitation of κ-carbide. Later stages consisted of coarsening of κ-carbide along <100> with precipitation of a $Mn_{12}Si_7Al_5$ intermetallic on grain boundaries. Prodham and Chakrabarti make no mention of spinodal decomposition.[33]

The kinetics of κ-carbide precipitation in Fe-Mn-Al-C alloys have been studied by a number of researchers. Sato et al.[21] studied the kinetics of the growth of the wavelength of spinodal decomposition in a Fe-30Mn-9Al-0.9C (0.016P) alloy utilizing XRD and electron diffraction. They determined an activation energy of 180 kJ/mol for the growth of the modulated structure, which they attributed to an average activation energy based upon the diffusion of both carbon and aluminum during spinodal decomposition. The growth of the wavelength of the modulated structure during spinodal decomposition was shown to fit a coarsening model according to the following.

$$\lambda^n - \lambda_0^n = kt \qquad (1)$$

Where λ_0 is the initial wavelength and λ is the wavelength at a time t. The parameter k is a constant and n is the scaling constant. Sato found a value of n between 3.4 and 4.8. The hardening rate, however, was found to be a function of the compositional amplitude during spinodal decomposition which was associated mainly with diffusion of carbon.[21] In a previous study by Sato et al.[34] they showed that the increase in strength and hardness in Fe-Mn-Al-C alloys during aging is related to the increase in the amplitude of the carbon concentration which increases the strain amplitude as a function of time. This can

be explained by the theory of spinodal hardening by Kato et al.[35] who considered the increase in strength during aging to be the result of coherency stress associated with the growth in the composition amplitude.

Choo et al.[29] studied the kinetics of austenite decomposition in a Fe-30Mn-7.8Al-1.3C steel aged for up to 4 months at 550° C. During the early stages of aging corresponding to times less than 100 min at 550° C, the κ-carbide particles were smaller than 2 nm and consisted of ordered zones.[29] Ordered zones coarsened into cuboids with periodic spacing along <100> having an average wavelength of 8-12 nm after 180 min at 550° C.[29] They reported that the growth of the modulation wavelength with aging time fit the same coarsening model as previously used by Sato et al.[21] Choo et al.[29] used electron diffraction during the early stages of spinodal decomposition to determine an n value of 4.6 while later stages of aging for times greater than 100 min were characterized utilizing x-ray diffraction with a corresponding n value of 2.6. They attributed first stage slow growth of the wavelength to an increase in the size of the spinodally decomposed zones and particle coalescence. This is followed by an increase in the growth rate of the wavelength after 100 min that was the result of coarsening along <100> directions with n values approaching 3.[29] An n value less than 3 (2.6) was attributed to preferential coarsening along <100> directions. During later stages of aging, the elastic misfit between the κ-carbide and the matrix reached up to 2% and after more than 33 days of aging at 550° C, the κ-carbides coarsened into plates with habit planes parallel to {100}.[29]

Silicon is one of the most common alloying additions to Fe-Mn-Al-C alloys and is generally added to improve castability.[2] Most importantly, adding silicon has been reported to prevent or severely retard the precipitation of β-Mn, which is brittle and deleterious to impact toughness in age hardened materials.[3] β-Mn is reported to precipitate on grain boundaries in the temperature range of 550 to 750°C in alloys without silicon.[36] Increaseing the silicon content from 1.0 to 1.4% in a alloy of nominal composition Fe-30Mn-9Al-0.9C-0.5Mo has also been shown by Howell et al.[1] to increase the strength and hardness during aging at 530° C. Acselrad et al. used resistivity measurements to characterize phase transformations in a Fe-28Mn-8.5Al-1C-1.25Si steel and suggested that silicon increased the rate of zone formation during spinodal decomposition.[3] They additionally proposed that silicon partitions manganese from the austenite matrix into the κ-carbide during aging and experimental evidence was presented that grain boundary carbides were enriched in Mn.[3] It was suggested based upon these observations that after sufficient aging times the austenite was depleted of enough manganese to prevent β-Mn precipitation and $D0_3$ or B_2 iron aluminide phases formed instead.[3] Acselrad determined the lattice parameter of the $D0_3$ phase to be 5.86 Å.[6] Tan et al.[37] report that silicon additions favor the formation of $D0_3$ iron aluminide and $D0_3$ was reported in the as-quenched state in a Fe-10Al-30Mn-1.2Si-0.5C steel. Chu at al.[38] studied the growth kinetics of κ-carbide in a Fe-30Mn-10Al-1C-1Si alloy aged at 550 and 700° C. They found that the kinetics fit a coarsening model with an activation energy of 196 kJ/mol that was correlated to the activation energy of bulk diffusion of carbon in austenite.

Chu at al. attributed the uncharacteristically high activation energy to elastic effects and strain energy interactions between the particles and the matrix reducing the driving force for coarsening.[38] The composition of extracted κ-carbides were determined to be 50Fe-30Mn-20Al (at.%) which was close to matrix chemistry of 54Fe-27Mn-19Al (at.%), but rich in Mn when compared with matrix.[38] Additional evidence that silicon influences manganese partitioning comes from a study by Chao et al. who reported manganese rich grain boundary κ-carbides in a Fe-28.6Mn-9.8Al-0.8Si-1.0C steel after aging for greater than six hours at 600°C.[39] The concentration of manganese in the κ-carbide was determined by energy dispersive X-ray spectroscopy (EDS) to be 46.5 wt.%, which was almost 18% more manganese than the austenitic matrix composition.[39] Manganese rich grain boundary κ-carbides were also observed in a Fe-8Al-31.5Mn-1.05C alloy without silicon addition.[40] Interestingly, β-Mn was not observed, even after extended aging for 24 hours at 550°C.[39] In a later study by Acselrad et al., it was reported that increasing silicon to 1.4% shifted the boundary for nucleation and growth of κ-carbide to shorter times and this was suggested to be the result of silicon increasing the activity of carbon in solid solution austenite.[6] Acselrad et al. used EDS analysis to determine a manganese content of 47wt.% for the grain boundary κ-carbides, which was well above the concentration of matrix manganese at 28wt.%.[6] Most recently, Seol et al. have utilized LEAP to study the composition of a lamellar structure of κ-carbide and ferrite in a Fe-1.2C-3.2Mn-10Al (in at.%) steel.[41] These κ-carbides were also found to be manganese rich with an aluminum concentration that was close in composition to the adjoining ferrite. They suggest that manganese substitution for iron would make the κ-carbide

harder and stronger because of stronger bonding between Mn-C couples in comparison to Fe-C pairs.[41]

In conclusion, most sources agree that precipitation of κ-carbide is the result of first stage spinodal decomposition of the austenite into carbon or carbon and aluminum rich and poor zones. Ordering into the $E2_1$ κ-carbide structure takes place within the zones concurrently or immediately after spinodal decomposition. Initially, κ-carbides consist of a high density of ordered zones. With time, coarsening of the κ-carbides results in a cuboidal morphology with periodicity along austenite <100>. Silicon increases the strength and hardness of Fe-Mn-Al-C alloys during aging and prevents or retards β-Mn formation; however, the mechanism for this is unknown. The most popular theories suggest that silicon partitions manganese into the κ-carbide during aging or that silicon increases the activity of carbon in solid solution austenite and increases the kinetics of zone formation.

2.2. DEFORMATION MECHANISMS

Deformation behavior in high manganese austenitic steels is reported to depend mainly on the stacking fault energy, SFE. TRIP is associated with ε-martensite formation, which can act as a nucleus for α'-martensite during deformation of unstable austenite with SFE less than 12 mJ/m^2.[41] ε-martensite formation is reported for SFE below 18 mJ/m^2 and mechanical twinning is reported for SFE between 12 and 35 mJ/m^2.[42] TWIP and TRIP in austenitic manganese steels is reported to be responsible for the simultaneous enhancement of strength and formability.[43] Dumay et al.[41] determined the influence of alloying elements on the stacking fault energy in the Fe-Mn-C system and showed that aluminum had the greatest effect on increasing SFE.

Tian et al. studied the effects of aluminum on the work hardening behavior of a solution treated Fe-25Mn-(0.57-5.02)Al-0.15C alloy.[44] They found that increasing the aluminum content decreased both the work hardening exponent and the work hardening rate. The work hardening exponent decreased from 0.89 to 0.76 as the aluminum content increased from 0.57 to 5.02% Al and mechanical twinning and ε-martensite formation was suppressed. Frommeyer et al. calculated the stacking fault energy of Fe-28Mn-12Al-1.2C steel to be 110 mJ/m^2.[14] Howell et al.[1] reported a SFE of 100 mJ/m^2 for a Fe-30Mn-9Al-(1.0-1.4)Si-0.9C steel. Dumay et al.[41] show that silicon also increases SFE for additions up to 4 wt.%, but silicon decreases SFE in amounts greater than 4 wt.%. It is traditionally accepted that the deformed microstructure of FCC alloys with low SFE exhibits a planar array of dislocations while dislocation cell formation is observed during the deformation of FCC materials with high SFE. Recently, Park et al.[45] reported planar glide is dominant during deformation of fully austenitic high Mn steels with relatively high SFE over 70 mJ/m^2. The effect of Al on the plastic deformation of a fully austenitic Fe-22Mn-(0-6)Al-0.6C steels with SFE between 20 and 50 mJ/m^2 was studied by Park et al.[30] It was determined that the dominant deformation in all of the steels was planar glide before the occurrence of mechanical twinning and this tendency became more evident with increasing SFE. It was thus determined that SFE is not a critical material parameter in determining the glide mode.[30] The occurrence of planar glide in high SFE austenitic manganese steels has been reported by several authors to be the result of "glide plane softening" associated with short range ordering in solid solution.[30,46,47] Short range ordering of Fe-Al-C clusters with spatial distribution described by the $E2_1$ superlattice structure in a solution treated Fe-28Mn-9Al-0.8C was also reported by Park et al.[30]

Dastur and Leslie[48] showed that the principal mechanism of rapid work hardening in Hadfield steel was dynamic strain aging caused by the interaction of Mn-C couples with dislocations. Additionally, Medvedeva et al.[32] used first principles calculations to show that the binding energy between Mn-C pairs was strongly attractive and increased from 29 to 85 meV as the amount of manganese was increased from 3 to 6 at.%. Addition of Al to Hadfield's steel was shown to shift dynamic strain aging to higher temperatures and Zudiema et al. concluded that Al decreased the diffusivity of carbon.[46] Correspondingly, a first principles study of aluminum in an Fe-30Mn-XC alloy showed that the most energetically favorable positions of aluminum and carbon in austenite corresponded to the $E2_1$ perovskite structure of Fe_3AlC structure of κ-carbide.[32] They found that short range order in Fe-Al-C alloys strongly decreases the energy barrier for the nucleation of dislocations but does not increase SFE. They show that short range ordering in Fe-Al-C alloys strongly reduces the energy barrier for the nucleation of dislocations and suggest that this is the mechanism behind glide plane softening.[32]

2.3. FRACTURE BEHAVIOR

The effects of age hardening on (Charpy V notch) CVN toughness of a Fe-30Mn-8Al-1C alloy were first investigated by Hale and Baker.[19] In the solution treated condition, the room temperature breaking energy was 206 J which decreased to 106 J at -196°C. The fracture surface of the solution treated specimens tested at -196°C showed regions of transgranular brittle cleavage and this was suggested to be the result of crack nucleation at the intersection of deformation twins within the FCC matrix at low temperatures.

After aging for 6 hrs at 550° C, the toughness reduced to less than 10 J for specimens broken at room temperature. Aged specimens failed in a brittle intergranular manner. The reduced breaking energy and intergranular mode of fracture was attributed to brittle grain boundary precipitation at extended aging times.[19] Additionally, Howell showed that Charpy specimens of a Fe-30Mn-9Al-1Si-0.9C (0.006% P) steel that was aged for 10 hrs at 530° C displayed behavior consistent with a material that undergoes a ductile to brittle transition with a lower shelf energy of 39 J and an upper shelf energy approaching 120 J for specimens tested in the temperature range of -40 to 25° C.[7]

Howell et al.[7] studied the simultaneous effects of quench rate from solution treatment and phosphorus content on the CVN toughness of a cast 30Mn-9Al-1Si-0.9C alloy.[7] Results showed that decreasing the cooling rate from 337 °C/s to 0.4 °C/s decreased the room temperature notch toughness from 190 J to 137 J for solution treated specimens with low phosphorus, 0.006% P. The strongest factor influencing notch toughness was the effect of tramp amounts of phosphorus. Phosphorus was found to segregate to the grain boundaries and promote a hard and brittle phosphide eutectic phase which was detrimental to notch toughness. For specimens with high phosphorus, 0.07% P, increasing the cooling rate from 0.4 to 337 °C/s during the quench increased toughness from 5 to 32 J at room temperature. Thus, for specimens quenched in water at the fastest cooling rate of 337 °C/s, increasing the amount of phosphorus from 0.006 to 0.07% in the same nominal composition alloy led to a 150 J reduction in the breaking energy from 180 to 30 J.[7] Aging also leads to a sharp decrease in notch toughness and the 0.006% P alloy was shown to have a reduction in toughness from 180 J to 120 J for specimens aged for 10 hrs at 530° C to a hardness of 305-310 BHN.[7]

In comparison, high phosphorus specimens with greater than 0.04% P that were aged for 10 hrs at 530° C had much higher hardness values, greater than 340 BHN, than low phosphorus (<0.006 % P), less than 310 BHN.

Medvedeva et al.[8] used first principles calculations to show that phosphorus substitution of aluminum corner positions in the κ-carbide structure is energetically more favorable than in face positions or substitution in the matrix austenite as shown in Table 2.1. They show that phosphorus substitution may be responsible for the embrittling mechanism during aging in high phosphorus specimens. Under the application of stress the P substitution produces open volume defects along <100> which may contribute to nearly a 50% reduction in the cleavage stress of the κ-carbide as shown in Figure 2.1.[8]

Table 2.1. Phosphorus substitution in Fe_3AlC: solution enthalpy ΔH_s, lattice parameter a, and distances between P and the nearest Fe (R_{Fe-P}) or C atoms (R_{C-P}).[8]

	ΔH_s, eV	A, Å	R_{Fe-P}, Å	R_{C-P}, Å
Fe_3AlC: P_{Fe}	2.40	3.758	2.66	1.96
Fe_3AlC: P_{Al}	0.67	3.752	2.58	
Fe_3AlC: P_C	1.22	3.797	2.02	
γ-Fe: P_{Fe}	2.43	6.621	2.53	
γ-Fe: P_{int}	5.21	3.654	2.07	

Schulte et al.[49] showed that phosphorus mitigation in a Fe-30Mn-9Al-1Si-0.9C-0.5Mo steel is possible using additions of Ca and rare earth additions in the form of misch metal. The Ce and La in the misch metal additions tied up the phosphorus as complex rare earth inclusions prior to solidification and increased the -40° C breaking energy from 22 to 38 J for specimens aged to a hardness in the range of 320 BHN.

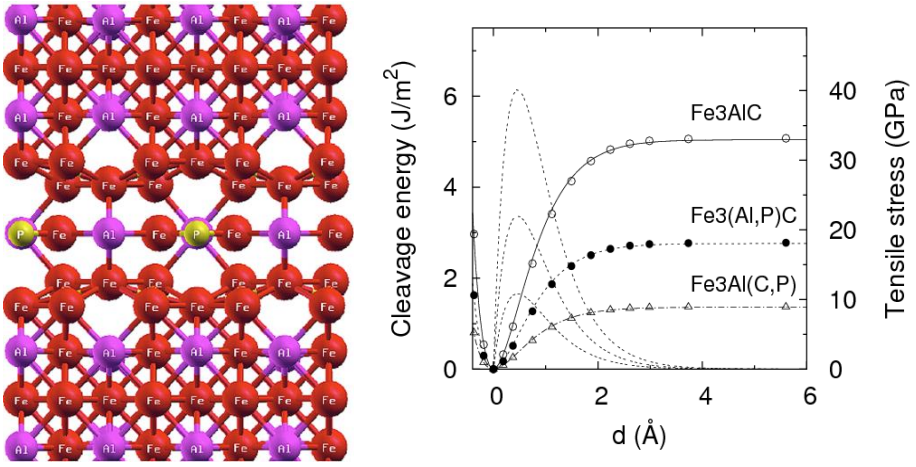

(a) (b)

Figure 2.1. (a) The (101) projection of the relaxed κ-carbide structure showing a relaxed structure in the vicinity of aluminum substitution by phosphorus. (b) Cleavage energies $G_C(x)$ (solid line), cleavage stress σ(x) (dotted line) versis cleavage separation in Fe_3AlC and $Fe_3(Al,P)C$.[8]

Notch toughness was a strong function of aluminum nitride content and aged specimens with more than 40 AlN particles/mm^2 had -40° C breaking energies less than 25 J. In contrast, using a teapot style ladle for pouring the castings reduced the amount of AlN to less than 10 particles/mm^2 and improved the -40° C breaking energy to almost 40 J.[49] However, adding more than the required amount of cerium needed to tie up phosphorus can also be detrimental to both notch toughness and ductility. Bartlett et al.[50] studied the effects of cerium addition on a nominal Fe-30Mn-9Al-1Si-0.9C-0.5Mo composition alloy with high phosphorus, 0.03% P. It was determined that increasing the amount of cerium addition from 0.01 to 0.052 produced a brittle Laves phase corresponding to (Ce,La)Si_2 with a commensurate reduction in room temperature notch toughness from 214 J to 90 J in solution treated specimens and from 92 to 26 J at room temperature for specimens aged for 22 hrs at 530° C to a hardness in the range of 300 BHN.[50]

The fracture toughness of high strength steel can be characterized by either a stress intensity or a J-integral approach to fracture mechanics. For materials with low toughness and failure by cleavage fracture, there is restricted plastic deformation around the crack tip and thus linear elastic fracture mechanics (LEFM) can be used to evaluate toughness .[51] Toughness is then determined as a critical stress intensity factor, K_{Ic}. For sufficiently ductile materials, such as austenitic Fe-Mn-Al-C steels, failure is governed by the flow properties around the crack tip and the LEFM approach is no longer valid.[51] There will be extensive plastic deformation and the material will exhibit crack tip blunting. In the formerly mentioned case, an elastic-plastic fracture mechanics (EPFM) approach is required and the fracture behavior can be best described by the path independent J integral, which is equivalent to the energy release rate in elastic-plastic materials.[51] The fracture toughness of ductile materials, J_{Ic}, is defined as the critical value of J near the onset of stable crack growth.[52]

In both of the above determinations of fracture toughness, the material is assumed to be under quasistatic loading conditions of less than 2 MPa$\sqrt{m}$/s.[53] A material's resistance to fracture is often dependent on the loading rate; thus, the static J_{Ic} may not be representative of material behavior at high loading rates. Instrumented Charpy impact tests provide a reproducible way of measuring the time dependency of force and crack displacement at elevated loading rates; and thus, provides a means of measuring DFT. Schindler[54] has proposed a method of determining toughness from instrumented Charpy impact tests that is based on the crack tip opening displacement (CTOD) and crack tip opening angle (CTOA) models of crack nucleation and growth. This results in an algebraic expression for the dynamic J-R curve from which J_{1d} can be evaluated in an

analogous way to the determination of J_{Ic}.[52] This method is a single specimen approach with experimental inputs of the peak load (P_{max}), the energy up to peak load (E_{max}), and the total facture energy (E_{tot}), which are easily determined from the instrumented Charpy results. The Schindler[54] method has been used by several authors to determine the dynamic fracture toughness of high strength steels.[55-58] Appendix I gives an abbreviated description of the test procedure, a more complete description of may be obtained from a reading of Schindler[54], ASTM E 1820[53], and ASTM E 813[52].

Toughness also depends on the loading rate. Elevated loading rates tend to elevate the flow stress. The effect of flow stress on fracture toughness is a function of the failure mechanism. High strain rates promote cleavage fracture, which is stress controlled.[51] Steels whose fracture mechanism is strain controlled will often show an increase in toughness as the loading rate is increased.[51] An austenitic matrix and high work hardening rates, which are characteristic of Fe-Mn-Al-C steels, contribute to high energy absorption rates under impact loading.[14] Saxena et al.[59] calculated a value of 187kJ/m^2 for the quasi-static fracture toughness, J_{Ic}, of a hot rolled Fe-17Mn-3Al-0.45C-0.5Cr-0.5Ni steel. The apparent fracture toughness, K_A, of a Fe-28Mn-8.5Al-1C-1.25Si steel was evaluated by Acselrad et al.[12] as a function of heat treatment and by using instrumented Charpy tests. In the solution treated condition, the alloy had an appreciably high toughness of 330 MPa$\sqrt{m}$ (527 kJ/m^2) at room temperature. After aging at 550ºC for 15 hrs, the toughness decreased to 84 MPa$\sqrt{m}$, (34 kJ/m^2).[12] In addition, Acselrad observed cleavage-like fracture in aged specimens marked by linear striations in three different directions along the cleavage facet surface. Cleavage fracture in FCC alloys has been explained by microcrack nucleation and growth at the intersections of deformation

twins[59], microcrack formation caused by epsilon martensite plates[60], or by "slipping-off" of slip planes with a high density of dislocations.[61-63] In the later fracture mechanism, slip band cracking is facilitated by planar slip which can be produced by short range ordering or shearable precipitates.[63] In the "slipping-off" mechanism, a slip band develops and glide plane softening associated with short range ordering can make activation of a secondary slip system difficult. Shear strain accumulates within the narrow slip band. Dislocation induced defects weaken the band to the extent that the tensile component of the force on the band can cause separation along <111> slip planes.[63] This type of cleavage-like fracture has been observed at low temperatures in nitrogen bearing (17-18%) Cr and (13-18%) Mn steels[61-63] and was attributed to SRO of nitrogen producing a glide plane softening effect. Deformation twinning and epsilon martensite was not observed by Acselrad et al.[12] and the cleavage-like fracture of the Fe-28Mn-8.5Al-1C-1.25Si alloy was thus attributed to "slipping-off" along the slip plane in aged specimens where the deformation mechanism was by planer slip. Although cleavage fracture was not reported in all aged specimens, fracture by the "slipping-off" mechanism it was suggested, but not proven to be the result of hardening of the matrix from a high density of fine, <10 nm, and closely spaced κ-carbide.[12]

PAPER

1. Effect of Phosphorus and Silicon on the Precipitation of κ-carbides in the Fe-30%Mn-9%Al-X%Si-0.9%C-0.5%Mo Alloy System

L.N. Bartlett, D.C. Van Aken, K.D. Peaslee, and R.A. Howell

Missouri University of Science and Technology

Department of Materials Science and Engineering

Army Research Lab

Rolla, MO 65409

Tel.: 573-341-4717

E-mail: dcva@mst.edu

Key Words: Fe-Mn-Al-C, lightweight steel, age hardenable, phosphorus, silicon

Published in the Transactions of the American Foundry Society (2010).

ABSTRACT

An investigation of the age-hardenable Fe-30%Mn-9%Al-1%Si-0.9%C-0.5%Mo cast alloy has shown that small increases of phosphorus, 0.001 to 0.043 wt.%, produced an increase in hardness during age hardening in the temperature range of 530- 600°C (986 -1112°F). As the phosphorus level increased, the time to achieve peak hardness was also found to decrease by 50% and 60% for specimens aged at 530°C and 600°C, respectively. Kinetic analysis determined that phosphorous lowers the activation energy for the precipitation of κ-carbide, $(Fe,Mn)_3AlC$, by 120 kJ/mol as the phosphorous level is increased from 0.001 to 0.018 wt% and above. Calculated time temperature transformation (TTT) diagrams and comparison with kinetic data in literature suggests that phosphorus increases enthalpy of mixing for austenite and accelerates the initial spinodal decomposition. Phosphorous was also found to segregate to interdendritic areas and promote both the precipitation and growth of the κ-carbide on grain boundaries. The effects of silicon content on the aging characteristics at 530°C were also studied. As the amount of silicon was increased from 0.59 to 1.56 wt%, hardness increased an average of 34 BHN (Brinell Hardness number) for all aging times up to the peak aged condition. Increasing the amount of silicon is believed to increase the hardness of κ-carbide by displacing manganese from the austenite matrix into the κ-carbide.

INTRODUCTION

Lightweight and high strength austenitic manganese steels are currently being produced and evaluated as suitable material for cast P900 armor plate.[1] These alloys are in the Fe-Mn-Al-C system and are also being researched for structural applications because they offer a 12-15% weight reduction below that of traditional steels without

sacrificing mechanical properties. [2,3,4] Alloy chemistries that contain between 20 to 30 wt% Mn, 5 to 11 wt% Al, and 0.3 to 1.0 wt% C are age-hardenable.[5,6,2] All percentage values that appear in the following text are expressed in weight percent unless otherwise stated. In the as-cast and solution treated condition, the microstructure consists of an austenite matrix, which is supersaturated with carbon and aluminum and may also contain up to 15% of interdendritic δ-ferrite.[5,7,8] In the solution treated condition, these alloys also exhibit excellent ductility with reported elongations of up to 70% and ultimate tensile strengths in the range of 800 MPa.[3] Upon aging in the temperature range of 350 to 700°C (662 to 1292°F), strength is greatly improved by the homogeneous precipitation of nano-sized κ-carbide, $(Fe,Mn)_3AlC$, within the austenite matrix.[3-12] κ-carbide has the $E2_1$ perovskite crystal structure.[5,12] Recently, Howell et al. recorded tensile strengths as high as 1085 MPa in a cast Fe-29Mn-8Al-1.4Si-0.9C-0.5Mo alloy aged 30 hours at 530°C.[5]

It is generally agreed that the precipitation of κ-carbide commences with an initial spinodal decomposition of the austenitic matrix into carbon and aluminum rich and poor zones.[4,8-10,13-15] Upon further aging, a fine distribution of 20-30 nm sized κ-carbides form by ordering of the carbon and aluminum rich austenite. A cube on cube orientation relationship is observed. Extended aging times will produce a plate morphology where the κ-carbide plate is oriented along the <100> austenite.[11,16] Over aging will produce β-Mn and a loss of tensile ductility and notch toughness.[10] In silicon containing alloys, over aging produces intermediate compounds of B2 or $D0_3$ or both.[10]

Silicon is added to FeMnAlC alloys to lower the melting point, increase fluidity, and most importantly, to prevent the formation of brittle β-Mn during aging.[17,10] The

effects of silicon on the age hardening of an Fe-29Mn-8Al-XSi-0.9C-0.5Mo alloy have been recently studied by Howell et al.[5] It was demonstrated that as that amount of silicon was increased from 1.0% to 1.4%, the peak hardness increased from 372 to 384 BHN. Peak hardness was achieved after 30 hrs at 530°C and was independent of the silicon content. Also, the hardness was found to be higher for the 1.4% Si alloy for every aging time tested. However, it should be noted that these alloys were also high in phosphorus, 0.06% P; and, the effects of phosphorus on the age hardening characteristics of this alloy system have not yet been assessed. In the current study, an effort has been made to separate the effects of phosphorous and silicon on the age hardening response of a cast Fe-30Mn-9Al-XSi-0.9C-0.5Mo alloy.

EXPERIMENTAL PROCEDURE

To investigate the effects of phosphorus, four plates were cast with a nominal chemistry of Fe-30%Mn-9%Al-1%Si-0.9%C-0.5%Mo utilizing foundry grade alloys. All heats were prepared in an induction furnace under argon cover. Horizontal plate molds were prepared from phenolic no-bake olivine sand. The thickness of the plates measured between 1.5 and 1.9 cm (0.59 and 0.75 in.). Two of the plates were prepared from heats utilizing electrolytic manganese and were calcium treated during steelmaking. The other two plates were prepared from heats utilizing ferromanganese without any calcium additions. All chemical analyses were performed by ion coupled plasma spectrometry after sample dissolution in perchloric acid. Chemical compositions are listed in Table 1. The phosphorus levels were found to be 0.001 and 0.006% in the calcium treated heats using electrolytic manganese and 0.018 and 0.043% in the heats

prepared with ferromanganese. The ferromanganese used will contribute as much as 0.018% phosphorous if fully recovered during steelmaking.

Table 1. Chemistry Data, in Weight Percent, for Samples of Different Phosphorous Contents.

C	Mn	P	S	Si	Mo	Al	Fe
0.90	30.40	0.001	0.006	1.07	0.53	8.83	58.2
0.89	30.20	0.006	0.001	1.01	0.31	8.85	58.7
0.94	28.22	0.018	0.018	1.16	0.34	6.64	62.7
0.94	29.10	0.043	0.006	0.92	0.33	8.28	60.0

Each cast heat was sectioned into approximately 8×10 cm (3.15×4.0 in.) rectangular plates, solution treated for two hours ± 5 min at 1050°C ±5C°, and then water quenched. The plates were then ground flat and parallel per ASTM E18 in preparation for later hardness measurements. Each solution treated plate was then sectioned into 0.8 to 1.0 cm (0.32 to 0.40 in.) thick rectangular specimens. One specimen was retained from each heat to represent the solution treated condition. The other samples were separated by phosphorous content and aged at 530, 550, 570, and 600°C (986, 1022, 1058, and 1112°F). A Sentry Model "AL" salt pot furnace was used to conduct all aging experiments. Samples isothermally held at 530 to 570ºC were aged in a solution of 50% KNO_3 and 50% $NaNO_3$. Samples aged at 600°C were held in BaCl. The salt bath temperature was verified periodically during heat treatments by external thermocouple to be within ±3C° (±5.4F°) of the process temperature.

Upon removal from the furnace, the individual specimens were quenched in water and any residual salt was removed. The surface was then lightly ground to insure a clean surface for hardness measurements. Hardness measurements were taken using the Rockwell B and C scales and subsequently converted to a corresponding BHN (3000 kg load). All hardness values reported are representative of an average of 10 measurements and the reported uncertainty is reported as sample standard deviation. Metallographic specimens were prepared using standard practices and etched with 2% nital. Microstructural analyses were conducted by optical microscopy using a differential interference contrast technique, as well as utilizing a Hitachi S570 scanning electron microscope (SEM).

In order to separate the effects of silicon from phosphorus, three low-phosphorus heats were prepared in an induction furnace with a nominal chemistry of Fe-30%Mn-9%Al-0.9%C-0.5%Mo. These heats were produced with silicon contents of 0.5, 1.0, and 1.5% Si. To insure maximum cleanliness, all heats were melted under argon cover, triple calcium treated, and argon stirred. The resulting melt was cast into phenolic nobake silica sand molds in a similar manner as above. A zircon wash was applied to the molds to prevent reaction of the manganese with the silica sand. The chemistries of the Si modified material are listed in Table 2.

Table 2. Chemistry Data, in Weight Percent, for Samples of Different Silicon Contents

Si	C	Mn	P	S	Mo	Al	Fe
0.59	0.95	30.35	0.002	0.006	0.54	8.74	58.8
1.07	0.90	30.42	0.001	0.006	0.53	8.83	58.2
1.56	0.89	29.97	0.002	0.007	0.53	8.81	58.2

The cast plates were sectioned into smaller rectangular plates of approximately 8×10×2 cm (3.2×4.0×0.8 in.) in size using an abrasive saw. They were then solution treated at 1050°C ± 5C° for two hours and water quenched. Each plate was subsequently ground flat and parallel and cut into eight smaller rectangular specimens of thickness 0.8 to 1.0 cm (0.32 to 0.40 in.). One specimen from each sample chemistry was retained for hardness measurements and metallographic analysis of the solution treated condition. The remaining specimens were loaded into an air convection furnace and aged at 530°C. The furnace temperature was verified via independent thermocouple to be 529°C (984°F). After appropriate aging time, each specimen was withdrawn and quenched in a bath of room-temperature water. Hardness measurements were taken using the Rockwell B and C scales and subsequently converted to a BHN (3000 kgf load). Microstructural analysis was performed in a similar fashion as mentioned above.

RESULTS

Hardness measurements recorded during this study were used to construct hardening curves for each aging temperature. The aging curves for the 0.001, 0.006, 0.018, and 0.043% phosphorus samples are shown in Figure 1. Analysis of the aging data shows that as the amount of phosphorous increases, so does the hardness for each

corresponding aging time. The solution treated hardness, however, was found to be nearly the same regardless of chemistry (see Table 3). Increasing the phosphorous content also had the effect of decreasing the time to peak hardness for each aging temperature. As expected, an increase in the aging temperature produced a decrease in the time to reach peak hardness for all phosphorous levels. In addition, the peak hardness decreased as the aging temperature increased, thus displaying classic aging hardening behavior. Both the 0.001 and 0.006% P samples showed very similar trends at all aging times and temperatures. The highest hardness recorded for both the 0.001 and 0.006% P specimens was observed after 30 hrs at 550°C (1022°F) and measured 358 ± 5.4 BHN and 353 ± 4.0 BHN (95% CL), respectively. Peak hardness values for the 0.018 and 0.043% P samples occurred after 30 hrs at 530°C (986°F) and were recorded to be 379 ± 6.7 and 371 ± 3.9 BHN (95% CL) as shown in Table 4. On average, the 0.018 % P samples gave the highest hardness and hardening rates recorded for all aging temperatures. This is an unexpected result since the aluminum content of the 0.018 % P containing heat was low relative to the other samples.

Table 3. Recorded Solution Treated Hardness Values, BHN (3000 kg load)

Percent Phosphorus	S.T. Hardness, BHN
0.001	195 ± 3
0.006	194 ± 3
0.018	204 ± 2
0.043	203 ± 4

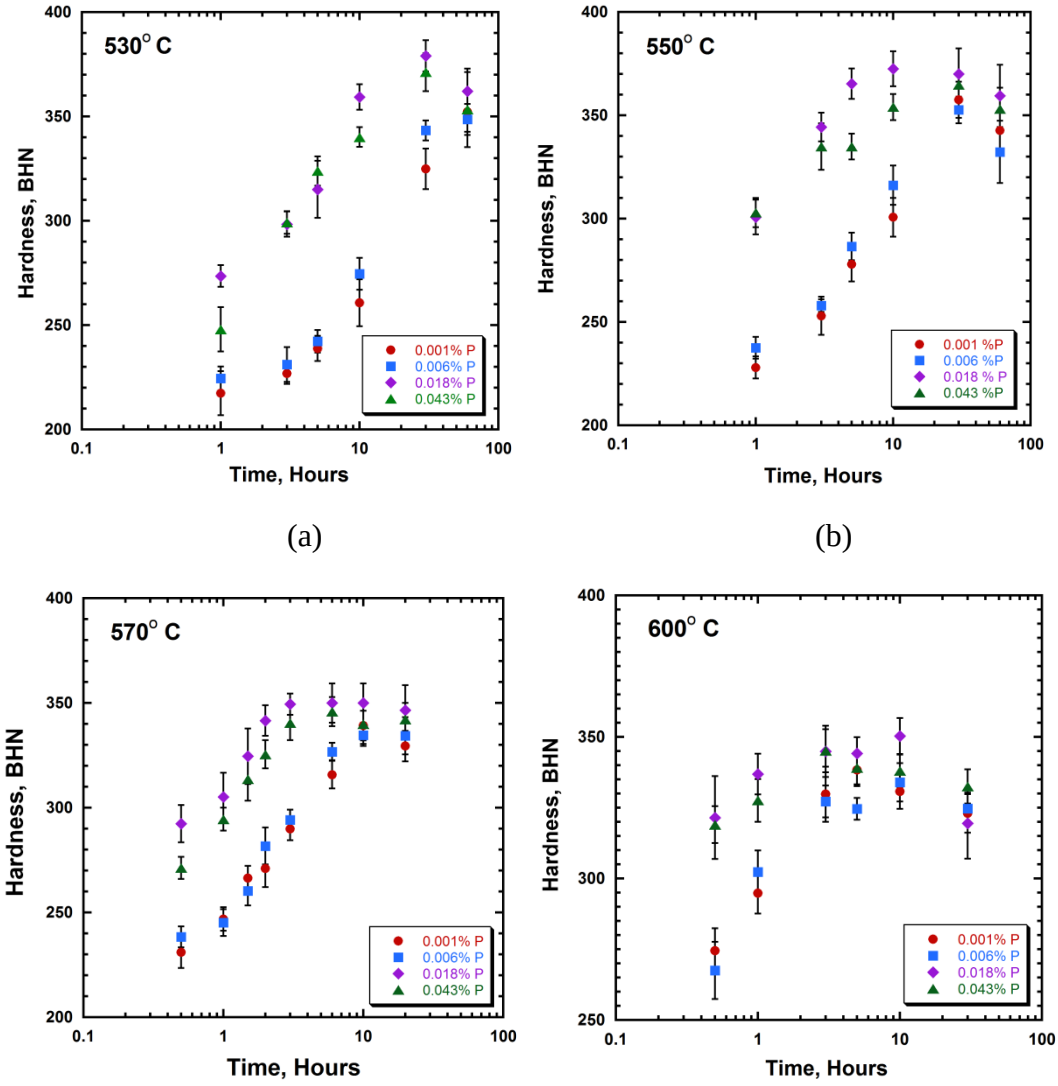

Fig. 1 Shown above are the various age hardening curves for the different phosphorus chemistry samples at (a) 530C, (b) 550C, (c) 570C, and (d) 600C. Both the 0.001 and 0.006% P samples gave similar hardness values. The 0.018 and 0.043% P samples consistently showed a much higher hardness than the 0.001 and 0.006% P samples for every time and temperature tested. In addition, rate of hardening increased with increasing amounts of phosphorus. Peak hardness was achieved after 30 hrs at 530C for the 0.018 and 0.043% P samples and not until after 60 hrs for the 0.001 and 0.006% P samples. The 0.018% P samples, in general, seemed to give greater hardness values than the 0.043% P samples, an unexpected result.

Table 4. Peak hardness values and time to achieve peak hardness for a temperature range of 530°C to 600°C and phosphorus contents of 0.001% to 0.043% with nominally 1%Si.

Temperature, °C	Percent Phosphorus	Peak Hdns, BHN	Time to Peak Hdns, hrs
530	0.001	352 ± 6.0	60
	0.006	348 ± 2.9	60
	0.018	379 ± 6.7	30
	0.043	371 ± 3.9	30
550	0.001	358 ± 5.4	30
	0.006	353 ± 4.0	30
	0.018	372 ± 5.2	10
	0.043	365 ± 3.5	30
570	0.001	339 ± 4.4	10
	0.006	335 ± 2.6	10
	0.018	350 ± 5.8	6
	0.043	346 ± 4.3	6
600	0.001	338 ± 3.5	5
	0.006	334 ± 4.1	10
	0.018	350 ± 3.9	10
	0.043	345 ± 4.7	3

Hardness measurements, as a function of aging, confirm that phosphorus increases not only the aged hardness, but also the hardening rate in FeMnAlC alloys. In order to better understand the role phosphorus plays in the nucleation and growth of κ-carbide, activation energies for κ-carbide precipitation in each of the different chemistry samples were calculated. To achieve this, an Avrami approach to transformation kinetics was utilized. Hardness values as a function of time for the different samples were used to generate a fraction of complete precipitation, f, according to the following equation.

$$f = 1- (H^f-H(t))/(H^f-H^0) \quad (1)$$

H^f is the peak hardness, H(t) is the hardness as a function of aging time, and H^0 is the solution treated hardness. When $H(t) = H^f$, $f = 1$, which corresponds to a maximum particle density. The volume fraction transformed was then used in the Avrami equation to determine an activation energy and rate constant for each chemistry sample. The following is one form of the Avrami equation. It is written so that the rate constant, k, is in units of reciprocal time. And n is the unitless time exponent, which typically varies from 0.5 to 4.

$$f= 1 – \exp[-(kt)^n] \quad (2)$$

The rate constant, k, can be defined by the Arrhenius relationship:

$$k = k_0\exp(-Q/RT) \quad (3)$$

In the above equation, R is the gas constant, T is the absolute temperature in Kelvin, and Q is the activation energy in J/mol.

The nucleation and growth process is isokinetic for a given temperature range if Q, k_0 and n are constant. Avrami plots were generated and activation energies where estimated for each chemistry sample by manipulating equations (2) and (3).

The rate constants as a function of temperature for each chemistry sample tested were determined from an Avrami log-log plot of $\ln(1/(1-V_f))$ vs. time in seconds. When $(kt) = 1$, $\ln(1/(1-V_f)) = 1$ and the corresponding rate constant for each temperature can be determined from the intersection of the isokinetic lines with the line $y = 1$. The slope of the isokinetic lines in Figure 2 gives values of the time exponent, n. Arrhenius plots were constructed to determine activation energies of the reaction assuming that the transformation was controlled by diffusional growth, i.e., transformation below the nose of the TTT. Activation energies for the different chemistry samples were obtained by linear regression analysis (Figure 3). The slope of the regression lines gives the value of Q/R. Because both the 0.018 and 0.043% samples were above the solubility limit of phosphorus in FeMnAlC alloys, they were considered together when determining the activation energy. Preliminary results show that as the amount of phosphorus increases, the activation energy for the precipitation of κ-carbide decreases. Activation energies for the 0.001 and 0.006% P samples were calculated to be 300 and 260 kJ/mol, respectively. An activation energy of 180 kJ/mol was calculated for the 0.018 and 0.043% P samples (Figure 3). Calculated kinetic data, including n and k_0 values, are listed in Table 5.

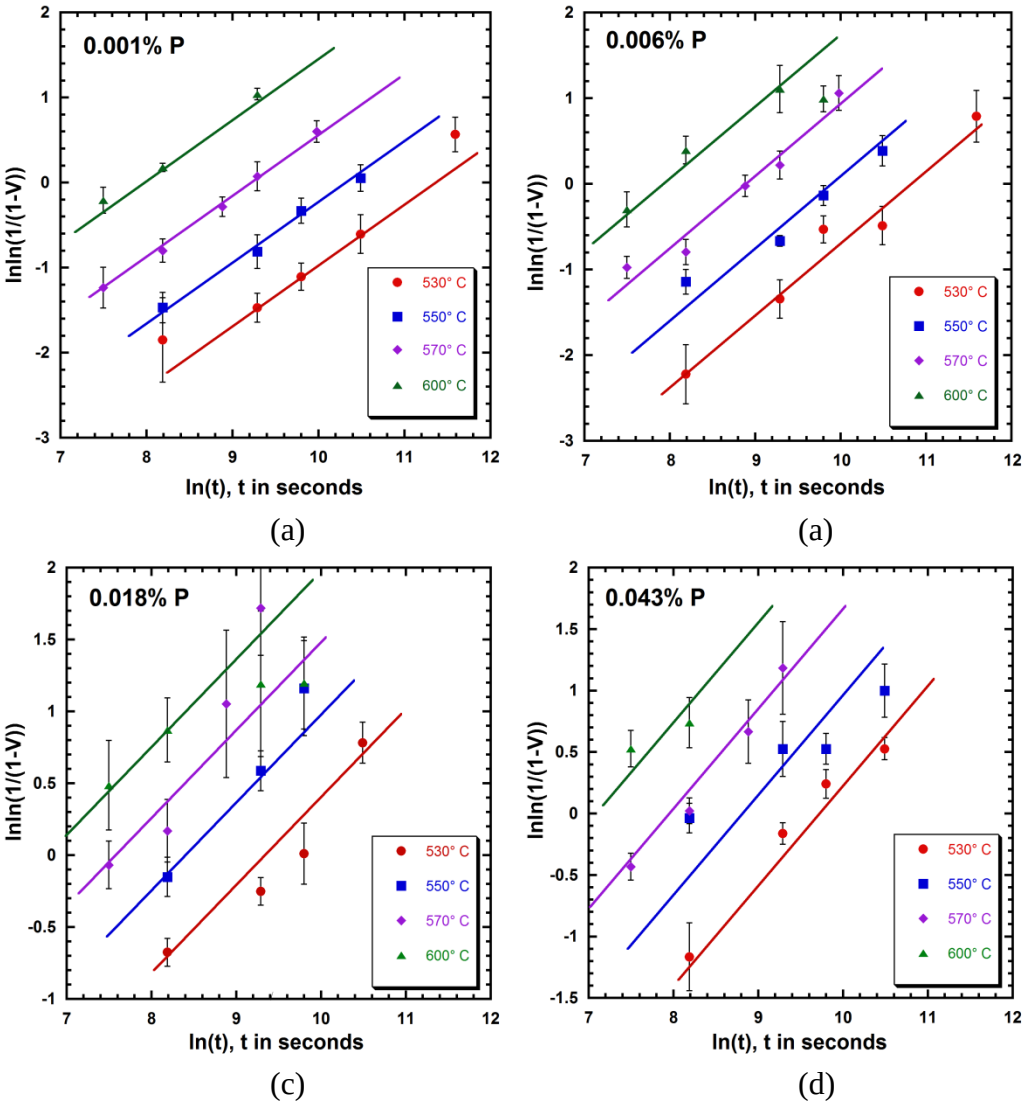

Fig. 2 Avrami analysis for the 0.001% P and 0.006% P samples produced isokinetic results (within error) for all temperatures tested. The slope of the parallel lines is equivalent to the time exponent, n, and was found to be 0.7 for the 0.001% P sample, and 0.8 for the 0.006% P, 0.018% P and 0.043% P samples.

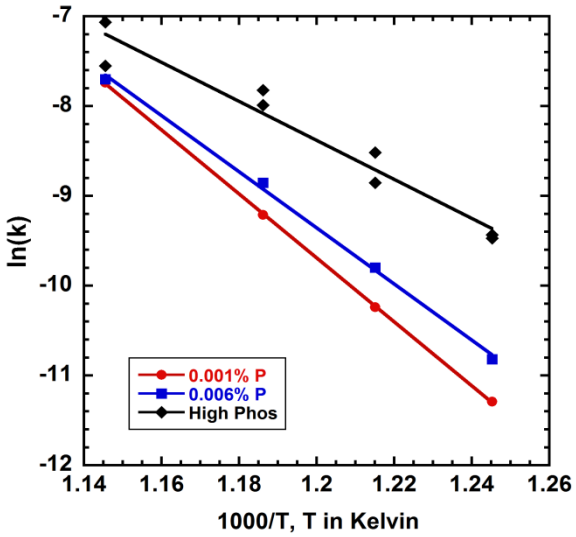

Fig. 3 In the above Arrhenius plot, the slope of each regression line is equivalent to Q/R for each of the different phosphorus levels, respectively.

Table 5. Calculated kinetic data for the different chemistry samples

% Phos	Q, kJ/mol	k_0, s^{-1}	n
0.001	300	$2.1X10^{14}$	0.7
0.006	260	$1.7X10^{12}$	0.8
0.018-0.043	180	$4.8X10^{7}$	0.8

Values of the time exponent, n, varied between 0.7 and 0.8 for all of the samples evaluated. Calculated kinetic data from the 0.001% P and 0.018% P samples was utilized to construct a TTT curve to better show the effects of phosphorus on the precipitation and growth of κ-carbide (Figure 4). Specifically, the Avrami and Arrhenius equations were manipulated to produce curves corresponding to a 1% and 50% transformation.

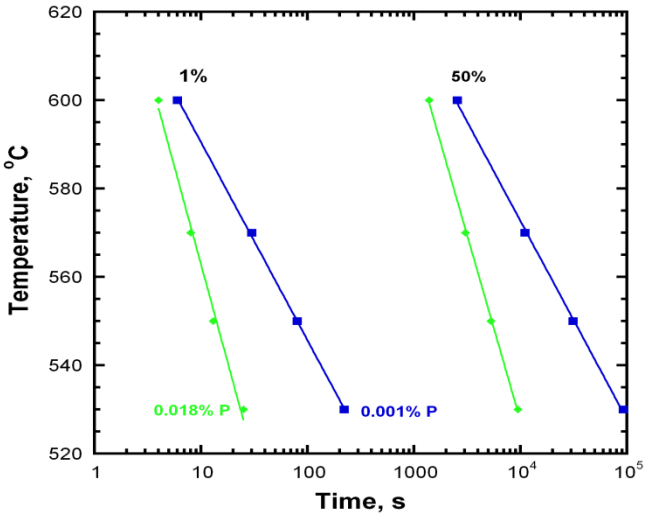

Fig. 4 Constructed TTT diagrams corresponding to a 1% and 50 % complete precipitation clearly show that transformation is delayed for the 0.001% P sample during early and later stages of aging.

Metallographic samples were prepared representing each of the differing chemistries for the solution treated condition as well as peak-aged condition for each temperature tested. Observations of the solution treated microstructures revealed the presence of undissolved ferrite in all but the 0.001% phosphorus-containing specimen. This is not a surprising result since phosphorus is well known to be a ferrite stabilizer. Overall, the greatest amount of ferrite was observed in the 0.018% phosphorus-containing specimens. The 0.018% P sample was also slightly higher in silicon, which is also a ferrite stabilizer (Table 1). The higher phosphorus specimens contained a large number of phosphide containing inclusions (see Figures 5c and 5d), which indicates that the solubility of phosphorus is less than 0.018%. The low phosphorus samples proved to have lower inclusion densities and no evidence of a phosphide phase.

The peak-aged microstructures showed that, in general, more grain boundary precipitation occurred in the higher phosphorus specimens (Figures 6a and 6b).

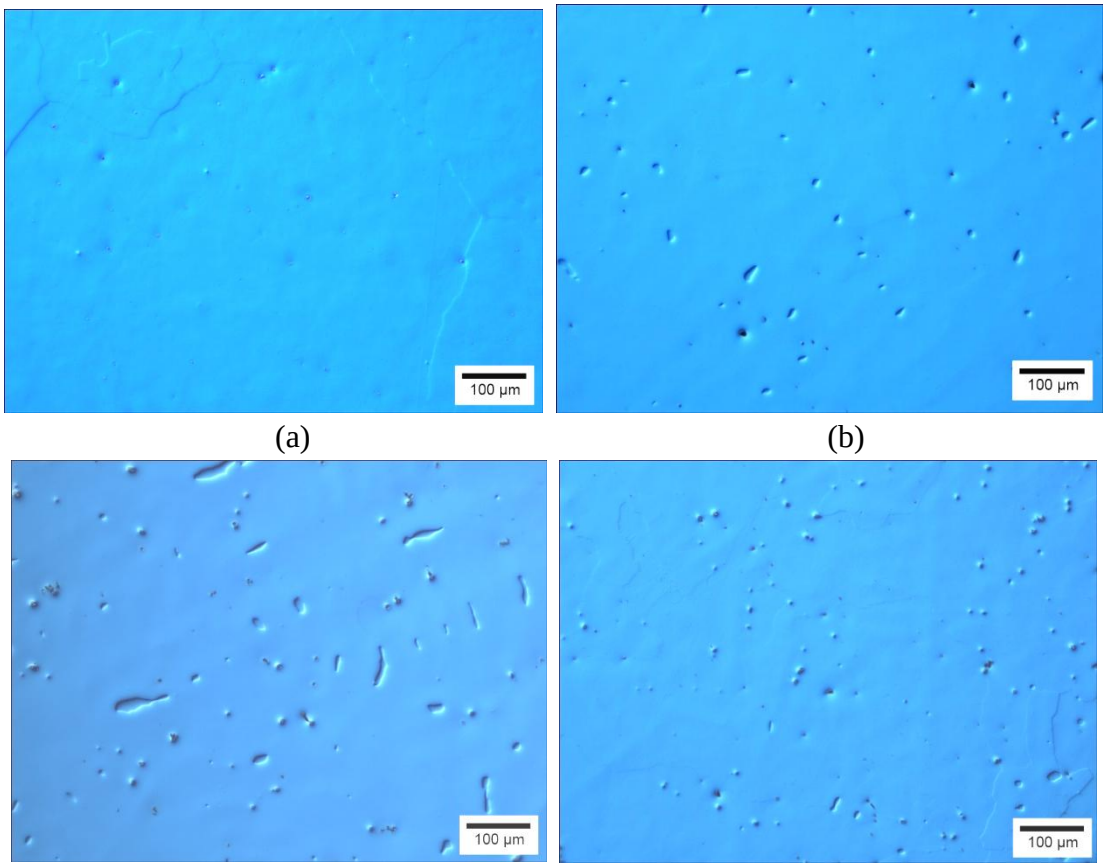

Fig. 5 The above optical micrographs correspond to the solution treated and quenched microstructure of the (a) 0.001, (b) 0.006, (c) 0.018, and the (d) 0.043% P specimens. Since phosphorus is a ferrite stabilizer, an appreciable amount of ferrite, 5%, was observed in the 0.018% P specimen in figure (c). In fact, a small volume percent of ferrite (around 1%) was observed in all of the remaining microstructures except in the 0.001% P specimen in figure (a). The microstructures in figures (c) and (d) also show a significant amount of inclusions and the presence of a hard phosphide eutectic phase that is detrimental to mechanical properties. All metallographic specimens were prepared by etching in a 2% nital solution and imaged using a differential interference contrast technique.

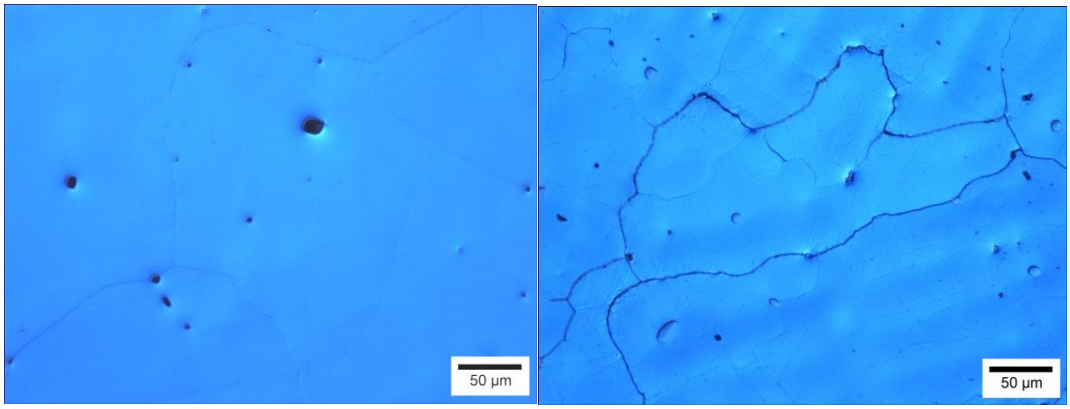

(a) (b)

Fig. 6 The above micrographs represent the peak aged condition at 600°C for the (a) 0.006 and (b) 0.018% P chemistry specimens. Both of the above micrographs show some degree of grain boundary precipitation. A considerable amount of what appears to be either extremely coarse κ-carbide or a fine intermetallic phase outlines the grain boundaries in figure (b). Note that there are only a few isolated islands of ferrite present in the microstructure of alloy (b). The reason for the decreased amount of ferrite observed in the peak aged condition is thought to be the effect of position in the casting and alloy segregation effects.

The increased amount of interdendritic ferrite and the prevalence of increased amounts of grain boundary precipitation in the samples with higher phosphorus contents is evidence that phosphorus segregates to interdendritic areas and promotes carbide precipitation on grain boundaries. SEM analysis of the peak aged condition of a 0.018% phosphorus specimen aged at 600°C shows regular arrays of what appears to be 30 to 50 nm sized κ-carbides within the austenitic matrix (see Figure 7). Carbides were too small in other samples to be detected, even when utilizing the SEM.

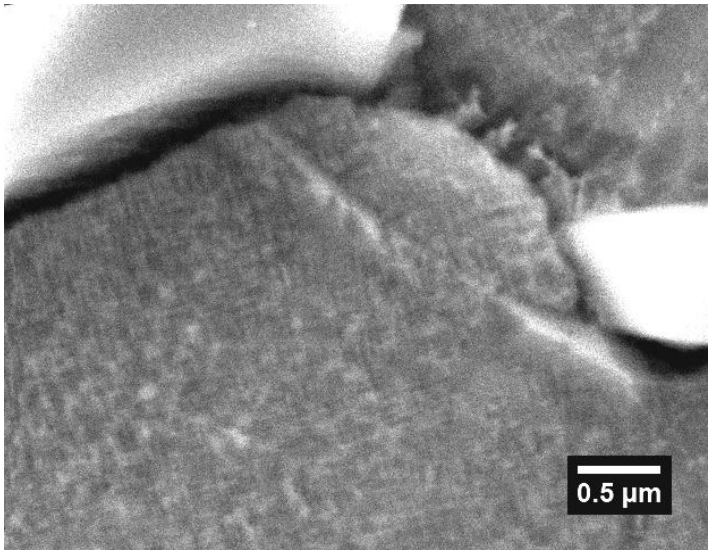

Fig. 7 Secondary electron micrograph of the 0.018% P specimen aged for 10 hrs at 600ºC. The light contrast features are the hard Mn and Fe-rich phosphide phase, which is shown outlining an austenite grain. Within the austenite matrix, what appear to be 30-50 nm κ-carbides are observed to have precipitated and aligned in a periodic and crystallographic direction.

In the solution treated condition, hardness was found to be nearly constant at around 198 ± 3.7 BHN for all of the different silicon containing alloys. The 530°C aging curves for the 0.59, 1.07, and 1.56% silicon samples are shown in Figure 8. Analysis of the age hardening data revealed that as the silicon level increased, so did the hardness at times tested up to the peak aged condition (see Figure 9). The 0.59% Si sample proved to have much lower hardness for most every aged condition than the 1.07 and 1.56% Si samples. However, the 0.59% Si sample exhibited higher hardness values after aging for 140 hrs. Peak hardnesses for the 1.07% and 1.56% Si samples were approximately the same and were recorded as 355 ± 5.3 BHN and 351 ± 7.6 BHN, respectively.

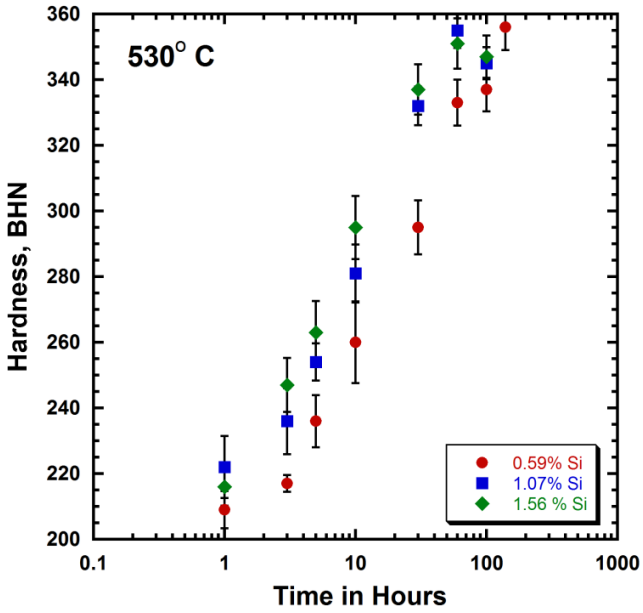

Fig. 8 The age hardening curves for the three different silicon containing alloys show that as the silicon level increased, so did the corresponding hardness levels for almost every aging time tested. Both the 1.07% and 1.56% silicon specimens achieved similar peak hardness values after 60 hours at 530°C. After 140 hrs, the 0.59% Si sample eventually exhibited the highest hardness.

In addition, the peak aging condition occurred after 60 hours at 530°C for both the 1.07% and 1.56% Si samples. Hardness for the 0.59% Si samples reached values as high as 355 ± 7.0 BHN after 140 hours. A peak aging time was not determined for the 0.59% Si alloy.

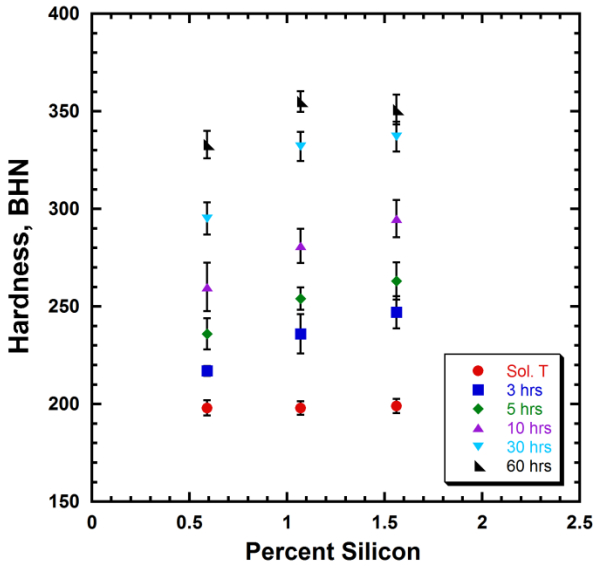

Fig. 9 Increasing the amount of silicon by 1% increased the aged hardness an average of over 30 BHN. The solution treated hardness, however, was unaffected by increasing silicon levels.

Specimens were prepared for microstructural analysis from each of the different silicon containing alloys. The microstructures corresponding to the solution treated condition and the peak aged condition are shown in Figures. 10 and 11, respectively. In the solution treated condition, less than 1.5% undissolved ferrite in the interdendritic regions was observed in the 1.56% Si containing alloy (see Figure 10c). However, it is important to note that the amount of ferrite in the 1.56% Si alloy depended on the position within the casting and the ferrite was more prominent in areas close to casting risers (see Figure 10d). Ferrite was not observed in the microstructures of the 0.59 and 1.07% Si alloys after solution treatent Also, There was little evidence of grain boundary precipitation for any of the peak aged specimens. In fact, the microstructures of the peak aged specimens were very similar and showed no major difference with increasing silicon content (see Figure 11).

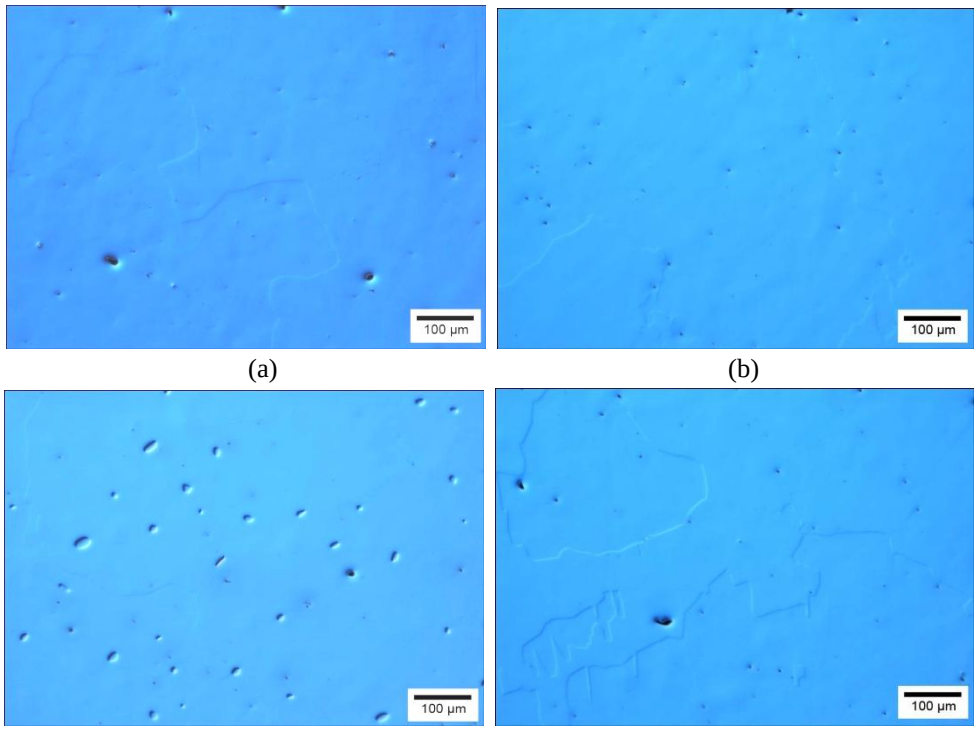

(a) (b)

(c) (d)

Fig. 10 The above optical micrographs are of the solution treated condition corresponding to the; (a) 0.59% Si, (b) 1.07% Si, (c) and (d) 1.56% Si alloys. The presence of ferrite was only observed in (c) and was thought to be a function of both higher silicon content and alloy segregation. The amount of ferrite in figure (c) was calculated to be 1.4%.

DISCUSSION

Phosphorus is widely regarded as an impurity in FeMnAlC steels, as well as most other steels, because it has been shown to segregate to grain boundaries and causes brittle fracture.[18-20] However, there have been no studies focused on considering the effects of phosphorus on precipitation hardening in the FeMnAlC system.

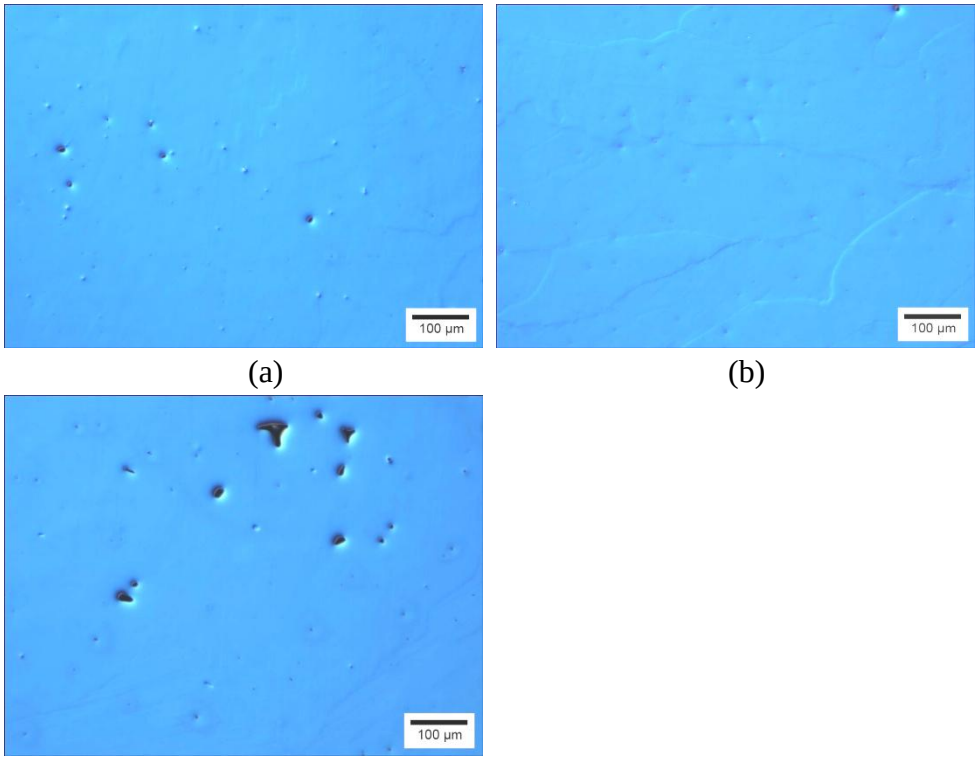

(a) (b)

(c)

Fig. 11 Micrographs of the peak aged conditon for the (a) 0.59%, (b) 1.07%, and (c) 1.56% Si specimens show very little evidence of grain boundary carbide precipitation and appear similar to the solution treated micrographs.

The results of this investigation show that amounts of phosphorus in the range of 0.006 to 0.043% increased the age-hardening response of these alloys. However, the slightly higher solution treated hardness in the higher phosphorus specimens is thought to be a combination of solid solution strengthening from the phosphorous and the formation of a hard phosphide found in interdendritic areas within the cast microstructure**.** Recently, Howell et al. studied the 530°C aging characteristics of a similar Fe-30Mn-9Al-0.9C-1.0Si alloy containing 0.06% phosphorus and found that peak hardness occurred after 30 hrs at 372 BHN, a result that is in excellent agreement with the current study.[5]

The 0.018% P samples consistently gave higher values of hardness for most every time and temperature tested even though they contained less than half the amount of phosphorus of the 0.043% P samples. One possible explanation for this unexpected result is that the aluminum content of the 0.018 % P sample is slightly different from the rest of the samples (see Table 1). However, aging curves at 550°C and 600°C for the 0.018% phosphorus samples are in close agreement with a study conducted by Hale and Baker[21] on a Fe-30Mn-8Al-0.8C-0.4Si alloy with a phosphorus content of 0.017%. In that study, peak hardness was recorded to be around 362 HV (344 BHN) for specimens aged at 600°C and a peak hardness value close to 390 HV (371 BHN) was recorded for specimens aged at 550°C. The current study supports these previous observations. In both investigations, the hardening rate was observed to increase after about an hour at temperature. Hale and Baker's results are attributed to a change in the hardening mechanism from a coherency strain, which is accompanied by the initial spinodal decomposition of the matrix, to the precipitation and growth of κ-carbide.[3,4,16,21]

In the current study, activation energies were calculated to be 300, 260, and 180 kJ/mol for the 0.001, 0.006, and 0.018-0.043% P samples, respectively. The 0.001 and 0.006% P samples gave the closest isokinetic results (Figure 2). One reason for the differences in kinetic behavior between the high and low phosphorus alloys could be that the precipitation reaction in the higher phosphorus material is more complex than originally thought.

Although, there is limited information on the kinetics of κ-carbide precipitation in literature, one study conducted by Sato et al. estimated the activation energy for spinodal decomposition, as a diffusion controlled process, to be 180 kJ/mol in a similar FeMnAlC

alloy with a phosphorus content of 0.016%.[16] The calculated activation energy of the high phosphorus samples in the current study, is almost identical to Sato's experimental value.

The activation energy for the precipitation of κ-carbide derived from the Avrami analysis is a complex combination of the activation energy of self-diffusion and the energy barrier, ΔG*, for the nucleation of a critical sized nucleus. For ordering reactions that produce homogeneous precipitation, the surface energy is small and this contributes to a near zero value of ΔG*.[22] Thus, the activation energy for the κ-carbide kinetics can be considered growth controlled and compared with the activation energy of self-diffusion of phosphorus, aluminum, and carbon. No data could be found on the direct measurement of diffusion of these elements in FeMnAlC steels, and limited data is available for diffusion of these elements in austenitic iron. Instead, activation energies obtained in this report are compared with values of 183 kJ/mol for the interdiffusion of phosphorus in austenitic iron (950 to 1250°C), 235 kJ/mol for the diffusion of aluminum in austenitic iron, and activation energies of between 120 and 150 kJ/mol for the diffusion of carbon in austenite (750 to 1300°C).[23,16] The low phosphorus alloys had an activation energy closest to that of aluminum diffusion in austenitic iron. This result suggests that aluminum is primarily responsible for the spinodal decomposition and subsequent precipitation of κ-carbide. In contrast, comparison of the calculated activation energy obtained for the higher phosphorus alloys suggests that as the phosphorus level is increased, the spinodal decomposition and precipitation is related to the diffusion of phosphorus.

Evidence that phosphorus drives the initial spinodal reaction comes from the previously mentioned study by Sato et al.[16] Sato found that in early stages of aging, spinodal decomposition was accompanied by the formation of characteristic x-ray sideband peaks around the main (200) austenite Bragg angle. It can be seen that the alloy containing the most phosphorus, 0.016% P, exhibited the most intense sidebands and the highest hardness. [16]

In the current study, additional evidence that phosphorus plays a role in spinodal decomposition can be seen in Figure 4. TTT curves corresponding to a 1% transformation show that transformation occurs more rapidly for the 0.018% P alloy as compared to the 0.001% P alloy. Thus, phosphorus is seen to affect the early stages of aging corresponding to the spinodal decomposition, as well as later stages in the precipitation process. It is interesting to speculate that the addition of phosphorus increases the enthalpy of mixing and consequently provides a greater driving force for spinodal decomposition. Additionally, specimens that were higher in phosphorus exhibited more κ-carbide precipitation on grain boundaries (see Figures 6c and 6d). Likewise, large κ-carbides that were 30 to 50 nm in size were observed to have precipitated within the austenitic matrix of a peak aged 0.018% P specimen (Figure 7). In the lower phosphorus specimens, κ-carbides were too small to be resolved using the SEM. Microstructural analysis also revealed that phosphorus segregates to interdendritic areas, promotes κ-carbide precipitation on grain boundaries, and in sufficient quantities produces a hard and brittle phosphide, which appears in a eutectic structure.[20]

For specimens aged at 530°C, additions of silicon were shown to increase the aged hardness for most every aging time. The solution treated hardness, rate of age

hardening, and the peak aged hardness were not affected by silicon content and these results are in agreement with a previous study.[5] The reason for the increase in hardness with increasing silicon content may be attributed to silicon displacing manganese from the austenite matrix to the κ-carbide.[5,16] Additions of silicon have previously been shown to restrict the formation of brittle β-Mn during extended aging and this restriction of β-Mn was believed to be a result of manganese partitioning into the κ-carbide, which leaves the surrounding austenite Mn-depleted.[10] In fact, the presence of β-Mn was not detected in any of the silicon containing specimens, even after extended aging times of 140 hrs at 530°C. It was generally observed, however, that silicon enriched regions were located in conjunction with riser positions, and, as a result, up to 1.4% ferrite was observed in the solution treated 1.56% Si material. Ferrite was not observed in any of the 0.59 or 1.07% Si samples.

CONCLUSION

Alloys in the Fe-Mn-Al-C system show great promise as lightweight substitutions for quenched and tempered alloy steels. Additions of silicon and trace amounts of phosphorus have been proven to increase the hardness of these alloys during aging treatments. During the course of this study, the effects of silicon and phosphorus on the aging of a Fe-30Mn-9Al-0.9C-XSi-0.5Mo alloy were separated. As phosphorus was increased, there was a corresponding decrease in the activation energies for the precipitation of κ-carbide in the temperature range of 530 to 600ºC. Activation energies for the high phosphorus alloys were found to be in close agreement with the activation energy for diffusion of phosphorus in austenite and with a similar alloy reported in literature.[23,16] In contrast, activation energies for the low phosphorus alloys were found

to be in closer agreement with literature values for the diffusion of aluminum in austenite.[16] Thus, in the low phosphorus alloys the initial spinodal decomposition may be driven by the enthalpy of mixing for aluminum. In the higher phosphorus alloys, the phosphorus may contribute to a more positive enthalpy of mixing and thus increase the driving force for spinodal decomposition and lower the activation energy for the aging kinetics. Microstructural evidence also shows that phosphorus segregates to interdendritic areas and increases the size and amount of grain boundary κ-carbides. Silicon, on the other hand, also contributes to hardening of Fe-Mn-Al-C alloys during aging, possibly by displacing manganese from the matrix into the κ-carbide. The results may suggest that the increase in Mn (based upon the work of Acselrad et al.[10] and Howell et al.[5]) may affect the strength of the carbide as justified by the higher hardness with increasing Si, but not a change in rate of hardening.

ACKNOWLEDGMENTS

This work was supported in part by Leonard Wood Institute under the provisions of cooperative agreement W911NF-07-2-0062 with Army Research Laboratory. The authors also gratefully acknowledge Waukesha Foundry, Inc. for providing the low phosphorous Fe-Mn-Al-C alloys and the alloys with varying Si content.

REFERENCES

1. MIL-PRF-32269, Military Performance Specification for Perforated Homogeneous Armor

2. Kayak, G. L., "Fe-Mn-Al Precipitation-Hardening Austenitic Alloys," *Met. Sc. And Heat Tr.*, Vol. 11, pp. 95-97 (1969)

3. Kalashnikov, I.S., Acselrad, O., Shalkevich, A., Chumokova, L.D., and Pereira, L.C., "Heat treatment and thermal stability of Fe-Mn-Al-C alloys,"*Journal of Materials Processing Technology*, vol 136, pp. 72-79 (2003)

4. Sato, K., Igarashi, Y., Inoue, Y., Yamazaki, T., Yamanaka, M., "Microstructure and Age Hardening in Spinodally Decomposed Austenitic Fe-Mn-Al-C Alloys," *Proceedings of the International Conference on Stainless Steels* (1991)

5. Howell, R.A., Weerasooriya, T., and Van Aken, D.C., "Tensile, High Strain Rate Compression and Microstructural Evaluation of Lightweight Age Hardenable Cast Fe-30Mn-9Al-XSi-0.9C-0.5Mo Steel" *Transactions of the American Foundry Society*, (2008)

6. Frommeyer, G. and Brux, U., "Microstructures and Mechanical Properties of High-Strength Fe-Mn-Al-C Light-Weight TRIPLEX Steels," *Steel Research Int.*, Vol. 77, pp. 627-633 (2006)

7. Acselrad, O., Dille, J., Pereira, L.C., and Delplancke, J.L., "Room-Temperature Cleavage Fracture of FeMnAlC Steels,"*Metallurgical and Materials Transactions A*, vol 35, pp. 3863-3866 (Dec. 2004)

8. Ishida, K., Ohtani, H., Naoya, S., Kainuma, R., Nishizawa, T., "Phase Equilibria in Fe-Mn-Al-C Alloys,"*ISIJ*, Vol. 30, pp. 680-686 (1990)

9. Han, K. H., Choo, W. K., Choi, D. Y., Hong, S. P., "Age Hardening in Fe-Mn-Al-C Austenitic Alloys," *TMS-AIME*, pp. 91-106 (1987)

10. Acselrad, O., Kalashnikov, I. S., Silva, E. M., Simao, R. A., Achete, C. A., Pereira, L. C., "Phase Transformation in Fe-Mn-Al-C Austenite Steels with Si Addition,"*Metallurgical and Materials Transactions A* , Vol. 33A, pp. 3569-3572 (2002)

11. Choo, W. K., Kim, J. H., "Microstructural and Mechanical Property Changes on Precipitation of Intermetallic κ' Cubic Carbide Phase in the Fe-Mn(Ni)-Al-C Solid Solution,"*Conf. on Thermo-mechanical Process. of Steels and Other Mats.*, pp. 1631-1637 (1997)

12. Kimura, Y., Handa, K., Hayashi, K., and Mishima, Y., "Microstructure control and ductility improvement of the two-phase γ-Fe/κ-(Fe, Mn)3AlC alloys in the Fe–Mn–Al–C quaternary system," *Intermetallics*, vol 12, pp. 607-617 (2004)

13. Ikarashi, Y., Sato, T., Yamazaki, T., Inoue, Y., and Yamanaka, M., "Age-hardening and formation of modulated structures in austenitic Fe-Mn-Al-C alloys," *Journal of Materials Science Letters*, vol 11, pp. 733-735 (1992)

14. Han, K.H., Yoon, J.C., and Choo, W.K., "TEM evidence of modulated structure in Fe-Mn-Al-C austenitic alloys," *Scripta Metallurgica*, vol 20, pp. 33-36 (1986)

15. Acselrad, O., Pereira, L. C., Amaral, M. R., "Processing Conditions, Microstructure, and Strength of an Austenitic Fe-Mn-Al-C Alloy," *Proceedings of Proc. and Prop. of Mats*., pp. 829-834 (1992)

16. Sato, K., Tagawa, K., and Inoue, Y., "Modulated Structure and Magnetic Properties of Age-Hardenable Fe-Mn-Al-C Alloys," *Met. Trans A*, vol. 21A, pp 5-11 (1990)

17. Howell, R. A., Lekakh, S. L., Van Aken, D. C., Richards, V. L., "The Effect of Silicon Content on the Fluidity and Microstructure of Fe-Mn-Al-C Alloys," *AFS Transactions*, Vol. 116, pp. 867-878 (2008)

18. Song, S.H., Zhuang, H., Wu, J., Weng, L.Q., Yuan, Z.X., "Dependence of ductile to brittle transition temperature on phosphorus boundary segregation for a 2.25Cr-1Mo steel," *Materials Science and Engineering A*, Vol 486, pp. 433-438 (2008)

19. Janovec, J., Jaroslav, P., and Lejcek, P. "Influence of Phosphorus Grain Boundary Segregation on Fracture Behavior of Iron-Base Alloys", *Trans. Tech. Publications, Switzerland* (2008)

20. Howell, R.A., Lekakh, S.N., Medvedeva, J.E., Medvedeva, N.I., and Van Aken, D.C., "Phosphorus and Thermal Processing Effects on Charpy V-Notch Impact Toughness of Lightweight Fe-30Mn-9Al-1Si-0.9C-0.5Mo Alloy Steel," Submitted to *Metallurgical and Materials Transactions A*. (2009)

21. Hale, G. E., Baker, A. J., "Carbide Precipitation in Austenitic Fe-Mn-Al-C Alloys," *Conf. on Alt. Alloying for Env. Res.* New Orleans, LA., (1986)

22. Christian, J.W., "The Theory of Transformations in Metals and Alloys: Part I," pp. 3-5, Pergamon Press Ltd., Oxford, (1975)

23. Gruzin, P.L. and Mural, V.V., "S -diffusion in 3%Si–Fe alloy," *Phys. Metals Meatallog*. Vol 16, No 4, pp. 50 (1963)

PAPER

2. Atom Probe Study of κ-carbide in Lightweight Steel: Part I. Effect of Silicon Addition

L.N. Bartlett, D.C. Van Aken, J. Medvedeva, D. Ishiem, N. Medvedeva, and K. Song

Missouri University of Science and Technology

Department of Materials Science and Engineering

Rolla, MO 65409

Tel.: 573-341-4717

E-mail: dcva@mst.edu

Key Words: Fe-Mn-Al-C, lightweight steel, age hardenable, atom probe tomography, silicon

To be submitted to Metallurgical and Materials Transactions A

The influence of silicon on κ-carbide precipitation in Fe-30Mn-9Al-(0.59-1.56)Si-0.9C-0.5Mo cast steels was investigated utilizing transmission electron microscopy, 3-D atom probe tomography, and X-ray diffraction. Increasing the amount of silicon from 0.59 to 1.56% Si increased the size of the κ-carbide precipitates but not the volume fraction. Silicon was shown to increase the activity of carbon in austenite and stabilize the κ-carbide at higher temperatures. Increasing the silicon from 0.59 to 1.56% increased the partitioning coefficient for carbon from 2.1 to 2.9 and the carbon content of the κ-carbide increased from 5.2 to 6.6 at.% for specimens aged for 60 hrs at 530° C. The increase in strength during aging of Fe-Mn-Al-C steels was found to be a direct function of the increase in the concentration amplitude of carbon during spinodal decomposition. The predicted increase in the yield strength was calculated to be 120 MPa/wt% Si for specimens aged at 530° C for 60 hrs and this is in agreement with experimental results. Silicon was shown to partition to the austenite during aging and to slightly reduce the austenite lattice parameter. First principles calculations show that the Si-C interaction is repulsive and this is the reason for enhanced carbon activity in austenite. The lattice parameter and stability of κ-carbide depends on the carbon stoichiometry and the silicon substitution site. Silicon was shown to favor vacancy ordering in κ-carbide due to a strong attractive Si-vacancy interaction. It was predicted that silicon occupies the iron sites in nonstoichiometric κ-carbide and the formation of Si-vacancy complexes increases the stability as well as the lattice parameter of κ-carbide. A comparison of silicon effect on the enthalpy of formation for austenite and κ-carbide shows that the

most favorable position for silicon is in austenite, in agreement with experimental results.

I. INTRODUCTION

Lightweight austenitic Fe-Mn-Al-C steels have both low melting points, less than 1350°C, and good filling characteristics which are similar to cast irons.[1] Addition of 9-10 weight percent (wt.%) aluminum reduces the density by up to 15% when compared with traditional steels and may be of interest to the transportation industry as corporate average fuel economy is increased to 54.5 mpg by 2025. These high aluminum steels can be competitive with quenched and tempered steels when age hardened. However, the high manganese (20 to 30 wt.%) required to stabilize an austenitic matrix[1,2] may relegate this class of steel to castings, since electrolytic manganese is required to limit phosphorus and may be too costly for current steelmaking practices.[3] Grades that contain from 5-11 wt.% aluminum and from 0.3-1.2 wt.% carbon are age hardenable when heat treated in the range of 450 to 700° C.[2-4] All compositions in the following text are in weight percent unless otherwise stated. Depending on the heat treatment, cast alloys can attain strengths as high as 1100 MPa in the age hardened condition or good ductility in the solution treated condition with total elongations greater than 64%.[3,5] Excellent strengths and high work hardening rates with up to a 17% reduction in density make these alloys very attractive for high energy absorbing applications.[2] However, the mechanical properties are a function of age hardening and knowledge of how alloying additions and impurities affect aging is of primary interest when qualifying these steels for high energy absorbing or low temperature applications.

Hardening is accomplished by the homogeneous and coherent precipitation of nano-sized κ-carbide, $(Fe,Mn)_3AlC_x$. κ-carbide has the $E2_1$ cubic perovskite crystal structure in which aluminum occupies corner positions, iron and manganese occupy face positions, and carbon is at the body center interstitial octahedral site. κ-carbide has a cube on cube orientation relationship with the austenitic matrix with $<100>_\kappa//<100>_\gamma$ and $\{001\}_\kappa//\{001\}_\gamma$.[6-10] Studies indicate that the first stage hardening in *Fe-Mn-Al-C* alloys is the result of compositional modulation produced by spinodal decomposition into either carbon rich[10-13] or carbon and aluminum rich[6,8,9,14] and depleted zones. Spinodal decomposition is thought to either precede[9], take place concurrently to, [6,10, 12-15] or subsequently[8,11] to short range ordering into lattice sites corresponding to the κ-carbide structure. This is followed by coarsening with the development of cuboidal shaped precipitates periodically arranged along <100>.

Silicon is one of the most common alloying additions to these high manganese and aluminum steels. Silicon increases the fluidity and decreases the melting point by 30C°/wt.%Si.[1] Most importantly, adding silicon has been reported to prevent or severely retard the precipitation of brittle β-Mn, which is deleterious to impact toughness in age hardened materials.[8] Increasing the amount of silicon in a an alloy of nominal composition Fe-30Mn-9Al-0.9C-0.5Mo from 1.0 to 1.56% increases the strength and hardness during ageing but decreases the work hardening rate and the total elongation to failure by as much as 10%.[5,16] Age hardening curves for Fe-30Mn-9Al-0.9C-0.5Mo, low phosphorus alloys (<0.003%P) with different silicon contents are given in Figure 1 (a) for specimens aged at 530°C. It is shown that increasing the amount of silicon increases the aged hardness but appears not to increase the overall hardening rate.[16]

The mechanism by which silicon increases hardness and prevents β-Mn in these steels is unknown.–Acselrad et al. reported that silicon increases the kinetics of zone formation during spinodal decomposition.[8] They additionally proposed that silicon partitions manganese from the austenite matrix into grain boundary κ-carbide during aging.[8] After sufficient aging times the austenite was depleted of enough manganese to prevent β-Mn precipitation and $D0_3$ or B_2 iron aluminide phases formed instead.[8] It is suggested that partitioning of manganese into the κ-carbide may also increase strength during aging. Manganese has a larger atomic radius, 0.179 nm, than iron, 0.172 nm, and therefore preferential substitution of manganese may increase the size of the κ-carbide and thus contribute to an increase in strength and hardness during aging.[16]

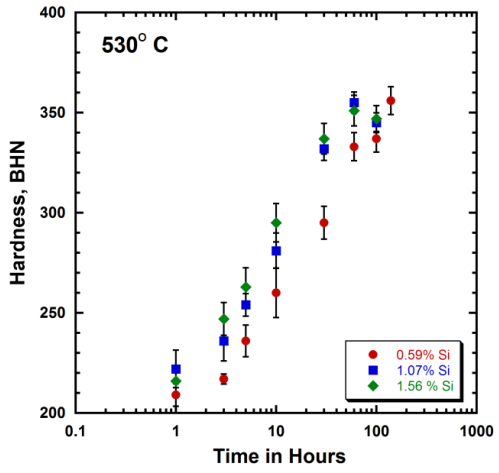

Fig. 1 Age hardening curves for low phosphorus (<0.003%P), Fe-30Mn-9Al-0.9C-0.5Mo steels aged at 530°C. Silicon increases the aged hardness but appears not to increase the hardening rate.

Evidence that silicon influences manganese partitioning comes from a study by Chao et al. who reported manganese rich grain boundary κ-carbides in a Fe-28.6Mn-9.8Al-0.8Si-1.0C steel after aging for greater than six hours at 600°C.[17] The concentration of manganese in the κ-carbide was determined by energy dispersive X-ray spectroscopy (EDS) to be 46.5 wt.%, which was almost 18% more manganese than the austenitic matrix composition.[17] However, manganese rich grain boundary κ-carbides were also observed in a Fe-8Al-31.5Mn-1.05C alloy without silicon addition and β-Mn was not observed, even after extended aging for 24 hours at 550°C.[18] β-Mn is reported to precipitate on grain boundaries in the temperature range of 550 to 750°C in alloys without silicon.[19] In a later study by Acselrad et al., it was reported that increasing silicon to 1.4% shifted the kinetics for nucleation and growth of κ-carbide to shorter times and this was suggested to be the result of silicon increasing the activity of carbon in the solid solution austenite.[14] Acselrad et al. used EDS analysis to determine the manganese content of grain boundary κ-carbides to be 47wt.%, which was well above the concentration of matrix manganese at 28wt.%.[14] Nevertheless, in all of the aforementioned studies, direct evidence of the effect of silicon on the homogeneous precipitation and composition of κ-carbide is lacking and evidence of manganese partitioning into the κ-carbide is restricted to grain boundary carbides. Additionally, in all of these studies, chemical analysis of the κ-carbide was performed utilizing EDS, and as such the amount of carbon could not be accurately determined. Thus, the explanation for increased hardening with silicon addition remains questionable.

It is clear from this review of the literature that despite fifty years of research many interesting questions remain as to the precipitation sequence of κ-carbide as well as

the role of silicon on age-hardening. Atom probe tomography allows the accurate determination of compositions as small as 50 ppm over interfaces with sub-nanometer resolution.[20] Local electrode atom probe tomography, LEAP, has been used to characterize precipitation in a variety of age-hardenable alloys including stainless steels,[21] Al-Sc alloys,[22] and Ni-based superalloys.[23] This technique has also been used to measure the extent of spinodal decomposition in Ti-Al-N thin films[24], Fe-Cr binary alloys,[25] as well as in Fe-Ni-Mn-Al alloys.[26] Most recently, Seol et al. have utilized LEAP to study the composition of a lamellar structure of κ-carbide and ferrite in a Fe-1.2C-3.2Mn-10Al (in at.%) steel.[27] κ-carbides were found to be manganese rich with an aluminum concentration that was close in composition to the adjoining ferrite. They suggest that manganese substitution for iron would make the κ-carbide harder and stronger because of stronger bonding between Mn-C couples in comparison to Fe-C pairs. The focus of the current work is to determine the role of silicon on the composition and morphology of κ-carbide that is homogeneously precipitated in a fully austenitic Fe-30Mn-9Al-0.9C-0.5Mo steel.

II. EXPERIMENTS

A series of alloys were cast with a nominal chemistry of Fe-30%Mn-9%Al-X%Si-0.9%C-0.5%Mo and with silicon ranging from 0.56 to 1.56%. Heats were prepared using electrolytic manganese, high purity aluminum, and high purity graphite. All heats were prepared in an induction furnace under argon cover. The melt was calcium treated followed by Ar-stirring before tapping and subsequently poured into horizontal plate molds that were prepared from phenolic no-bake olivine sand. The thickness of the plates measured approximately 1.5 cm. All chemical analyses were performed by ion

coupled plasma spectrometry after sample dissolution in perchloric acid and are listed in Table 1. Rectangular test coupons with nominal dimensions 1.4cm x1.4cm x2.0cm were machined from the center of the plate. Each alloy was solution treated for 2 hrs at 1050° C in protective stainless steel bags. Specimens were individually water quenched into agitated room temperature water. Aging was conducted in a salt pot containing a mixture of sodium and potassium nitrate salts. The variation in temperature during aging was +/- 5°C.

Table 1. Steel chemistries in weight percent.

Si	**C**	**Mn**	**P**	**S**	**Mo**	**Al**	**Cu**
0.59	0.95	30.35	0.002	0.006	0.54	8.74	0.01
1.07	0.90	30.42	0.001	0.006	0.53	8.83	0.006
1.56	0.89	29.97	0.002	0.007	0.53	8.81	0.006

Thin foils for transmission electron microscopy were prepared using a solution of 6% perchloric acid, 60% methanol, and 34% butoxyethanol and a twin jet electropolisher operating at -20°C utilizing and a DC current of 30-40 mA. Thin foils were analyzed using a Tecnai F20 TEM operating at 200 kV. LEAP specimens were prepared by machining 0.3x0.3x10mm rectangular blanks from the center of the solution treated and aged plates. Rectangular blanks were electropolished at room temperature in a two step polishing procedure. Initial thinning of the specimen to 0.2 mm in diameter was performed 20 V DC in a 10% perchlorc acid 90% acetic solution. Final polishing was accomplished utilizing a solution of 2% perchloric acid solution in butoxyethanol at 12 V

DC to produce a tip radius less than 100 nm. Polished tips were analyzed using a local electrode atom probe tomograph manufactured by Cameca, Madison, WI. Tips were held in a vacuum of $6.5X10^{-11}$ torr at a temperature of 60 K. A 0.5% evaporation rate was obtained at 500 kHz using 20 pJ laser pulse energy. Between 20 million and 500 million atoms were detected from each of the respective specimens. IVAS 3.6 software was utilized to construct a 3-D atom-by-atom representation of each specimen.

Specimens for X-Ray diffraction experiments were produced from bulk specimens that were polished to a 6 μm finish. Specimens were analyzed at room temperature utilizing a PANalytical X-PertPro diffractometer with Cu-kα radiation operating at 45 kV with a tube current of 40 mA. A nickel monochromator was utilized to filter out Cu-kβ radiation. Specimens were scanned over an angular range of 20 to 80° 2θ at a rate of 1/8° min^{-1}.

III. RESULTS

In the following text, the different alloys will be referred to by their silicon contents in weight percent as listed in Table 1. It should be noted that compositions given by LEAP are in atomic percent. Thin foils were prepared from selected specimens to directly show the influence of silicon on the morphology, size, and distribution of κ-carbide as a function of aging time and temperature. Solution treated samples were single phase and there was no evidence of austenite decomposition and electron diffraction patterns showed only fundamental austenite reflections. Figure 2 (a and b) are dark field images of 0.59% Si and 1.56% Si specimens that were aged for 63 hours at 490°C.

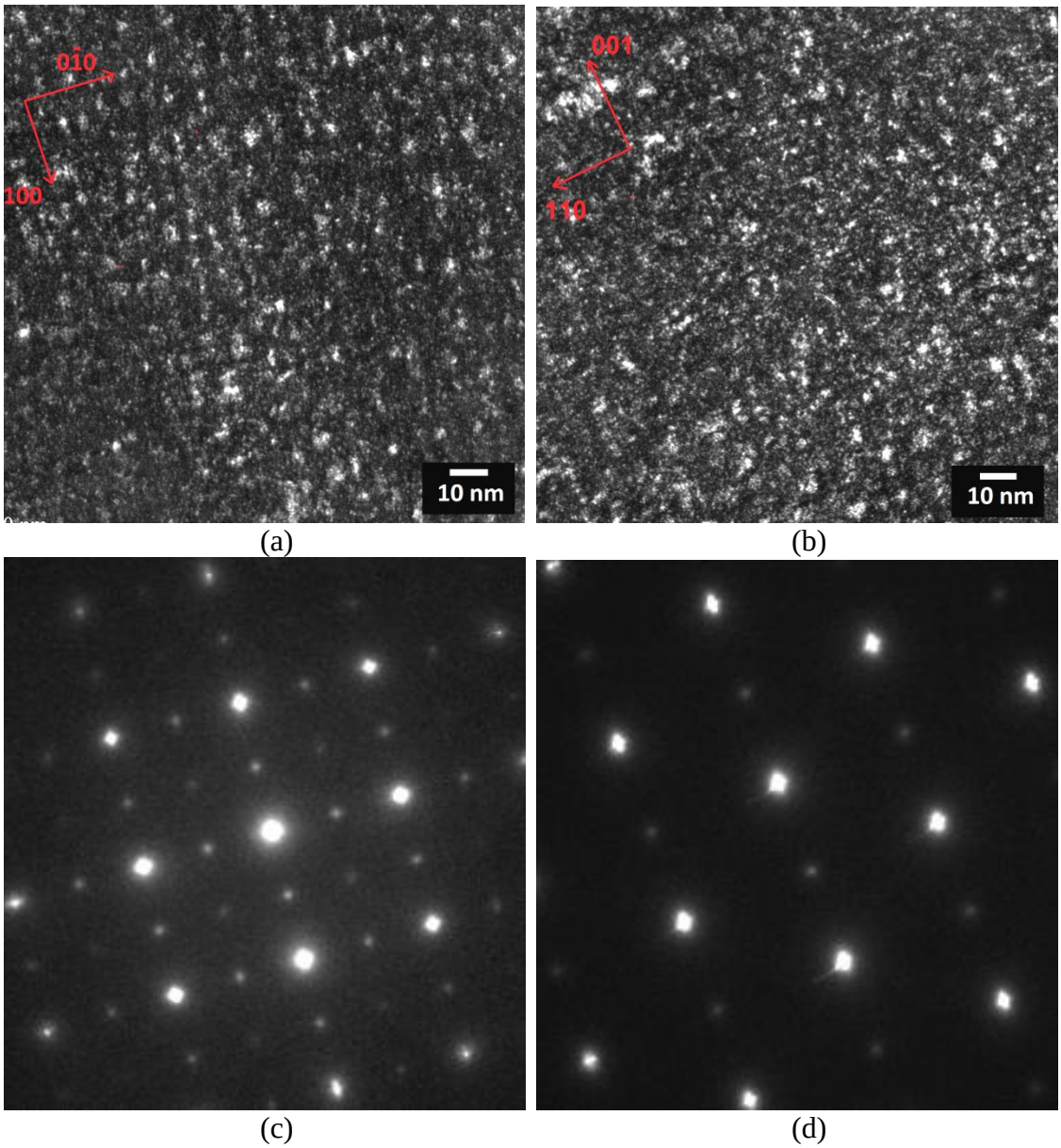

Fig. 2 (a) Dark field images of the (a) 0.59% Si and (b) 1.56% Si steels aged for 63hrs at 490°C show a high number density of κ-carbide particles that are on the order of 1 nm. The selected area diffraction patterns of the DF images in (a) and (b) corresponding to [001] and [101] zone axis, respectively are shown in (c) and (d). Particle clusters are coarsening into larger, 2-5 nm particles. (a) κ-carbide clusters of average size less than 3 nm may be in the beginning stages of alignment along a cube direction in the 0.59% Si specimen. (a and b) κ-carbide particle size is similar between both silicon containing specimens. Both diffraction patterns show satellites flanking fundamental austenite reflections in the (c) 0.59% Si and (d) 1.56% Si specimens, respectively.

Both images show a high number density of κ-carbide precipitates that are less than 1 nm and particle sizes are similar. These κ-carbides are randomly distributed throughout the austenite matrix in both alloys. High order austenite diffraction spots in the [001] SADP of the 0.59%Si specimen in Figure 2 (c) were elongated in cube directions, which is evidence of closely spaced satellite reflections and an advanced stage of spinodal decomposition. Diffraction intensity concentrated into satellite reflections was also noted in the [101] diffraction pattern aligned in the [001] direction in the 1.56% Si specimen in Figure 2 (d). Figure 3 (a and b) shows the 1.07% Si and 1.56% Si specimens that were solution treated and aged for 100 hours at 530°C. Increasing the aging temperature increases the kinetics of particle coarsening and the κ-carbides appear as cuboidal particles that are an average size of 10 nm in the 1.07%Si alloy (Figure 3 (a)) and 12 nm in the 1.56%Si (Figure 3 (b)) alloy as measured along a cube edge. The κ-carbides are periodically arranged along cube directions and the average wavelength of the spacing along <100> was 16 nm for the 1.07%Si specimen and 20 to 25 nm in the 1.56%Si specimen.

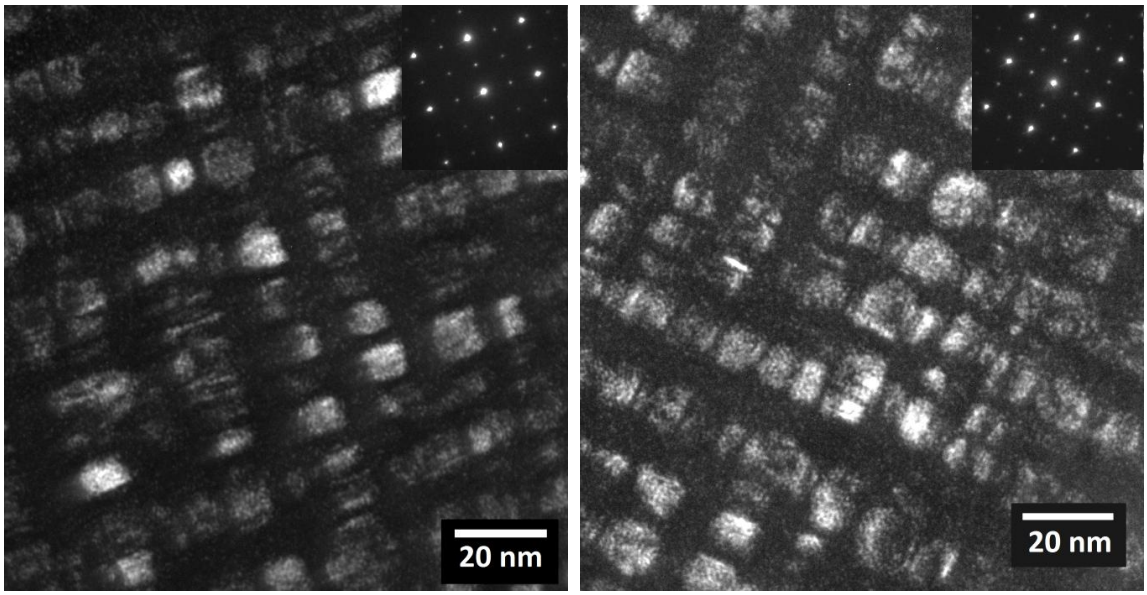

(a) (b)

Fig. 3 Dark field images of the (a) 1.07%Si and (b) 1.56%Si specimens that were aged for 100 hrs at 530° C show κ-carbide as cuboidal particles that are preferentially coarsening into plates along cube directions. (a) κ-carbides in the 1.07%Si specimen are an average size of 10 nm with an average interparticle spacing along cube directions of 16 nm. (d) κ-carbides are larger in the 1.56%Si specimen and are shown to be an average size of 12 nm with an interparticle spacing along a cube direction of 20 nm.

X-ray diffraction patterns for the 0.59% Si and 1.56% Si specimens, aged for 48 hrs at 570° C, are shown in Figures 4 (a) and 4 (b). The presence of β-Mn, B_2, or $D0_3$ phases was not detected in the x-ray diffraction patterns and the microstructure consisted of austenite and κ-carbide as shown in Figure 4 (a). A detail view of the austenite and κ-carbide (200) diffraction intensity is given in Figure 4 (b) and the amount of κ-carbide precipitation appears to be independent of silicon content. Table 2 shows calculated values of the austenite and κ-carbide lattice parameter as a function of aging and silicon addition.

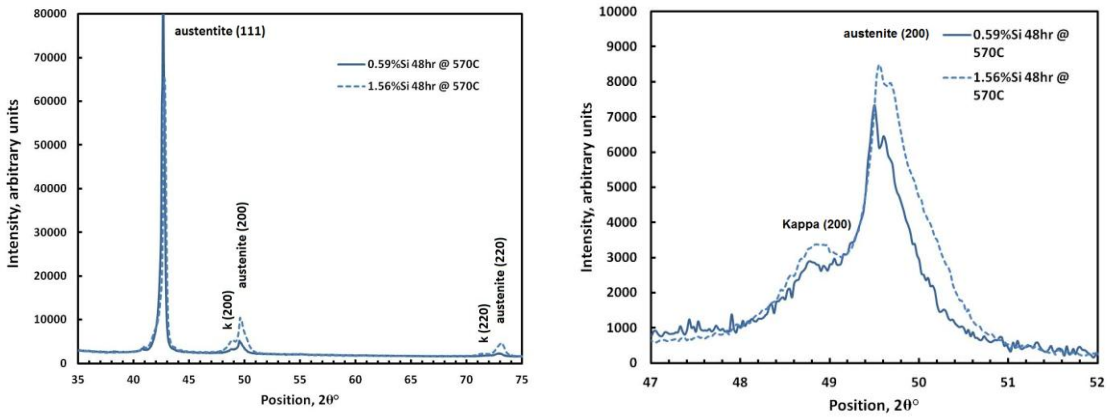

(a) (b)

Fig. 4 (a) The XRD patterns for the 0.59%Si and 1.56%Si low phosphorus containing (<0.003%P) specimens show only austenite and κ-carbide peaks after aging for 48hrs at 570°C. (b) Detail image of the austenite and κ-carbide (200) peaks from (a) show that there is little difference in the amount of κ-carbide precipitation with silicon addition.

Table 2. Calculated austenite and κ-carbide lattice parameters

Weight % Si	Heat Treatment	a^{γ}, nm	a^{κ}, nm	% Mismatch
0.59	Aged 60 hrs @ 530° C	0.3681	0.3712	0.84
1.56		0.3673		
0.59	Aged 48 hrs @ 570° C	0.3666	0.3718	1.41
1.56		0.3659	0.3731	1.97

The austenite lattice parameter slightly decreased with increasing silicon content for both specimens aged at 530 and 570° C. Increasing the amount of silicon from 0.59 to 1.56% Si, slightly increased the lattice parameter of κ-carbide from 0.372 to 0.373 nm for specimens aged for 48 hrs at 570° C. Because of extensive peak broadening in the XRD pattern of the 1.56% Si specimen that was aged for 60 hrs at 530° C, κ-carbide could not be distinguished from the fundamental austenite peaks. Table 2 shows that as the amount of silicon is increased, the lattice parameter of the austenite decreases with a

simultaneous increase in the κ-carbide lattice parameter. This induces a higher degree of lattice mismatch between the two phases as the silicon content is increased.

LEAP experiments were performed to determine the effect of silicon on the size, distribution, and chemical composition of κ-carbide. Specimens with 0.59% and 1.56% Si were prepared from steels that were aged for 60 hours at 530ºC. An aging temperature of 530° C was chosen to be consistent with mechanical property data and a condition of peak hardness at 60 hours. IVAS 3.6 software was used to create a virtual, rectangular, "slice" of the total reconstruction volume. The κ-carbides were discriminated from the matrix austenite by a 4 at.% C isoconcentration surface obtained with a voxel size of 1 nm and a delocalization of 3 nm. Figures 5 (a) and 5 (b) show the reconstruction slices of the 60 hr aged 0.59% Si and 1.56% Si specimens. The interface of the κ-carbide with the austenite matrix was arbitrarily chosen as 4 at.% C based on a carbon concentration sufficiently above the bulk carbon concentration, which ranged between 3 and 3.3 at.% C.

κ-carbide is shown as an interconnected structure rather than a cuboidal morphology, but the interconnected structure is modulated along cube directions. The volume fraction of κ-carbide was determined to be 0.19 for the 0.59% Si specimen and 0.18 for the 1.56% Si specimen and was calculated by summing the total number of atoms contained within the isoconcentration surfaces vs. the total number of matrix atoms. Molar volumes for the respective phases were calculated from the measured lattice paramters. The lattice parameter of κ-carbide in the 1.56% Si specimen was assumed to be similar to the 0.59% Si specimen and was estimated to be 0.3712 nm.

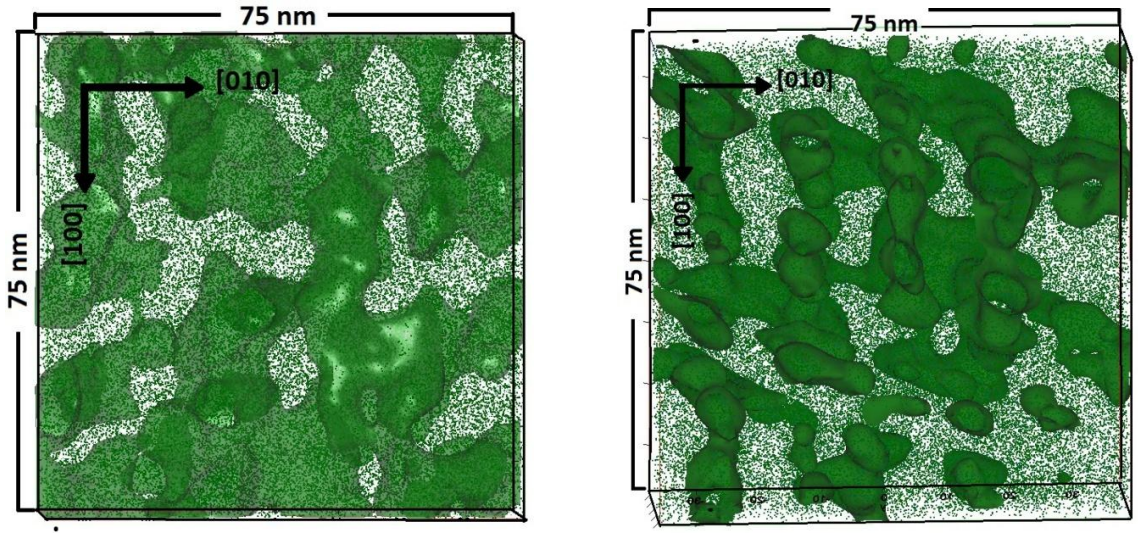

(a) (b)

Fig. 5 Virtual slices of the total reconstruction volume corresponding to the (a) 0.59%Si steel (0.002%P) and the (b) 1.56%Si steel aged for 60 hours at 530°C showing 50% of the total carbon atoms (green dots). The 4 at.%C isoconcentration surfaces delineate κ-carbide from the matrix. The volume fraction of κ-carbide is 0.19 and 0.18 for the 0.59 and 1.56%Si specimens, respectively. Slice depth in both reconstructions is 25nm.

A concentration profile of the austenite matrix vs. the κ-carbides for the 1.56%Si specimen, aged for 60 hours at 530°C, was generated by fitting a 4 nm diameter virtual cylinder across a group of precipitates as shown in Figure 6 (a). The concentration of carbon, aluminum, manganese, and iron through areas of κ-carbide and matrix austenite, which is "cut" by the continuous virtual cylinder, are shown to be consistent with a wave-like decomposition profile with an average wavelength of 14 or 15 nm as shown in Figure 6 (b). κ-carbide is shown as a modulated structure enriched with as much as 9 at.%C and 24 at.%Al and depleted in manganese and iron. A wave-like composition profile with a diffuse interface between the κ-carbide and the matrix is indicative of spinodal decomposition. The matrix areas between the κ-carbides are shown to be depleted in carbon and aluminum to levels as low as 0.8 and

12 at.%, respectively. The concentration profile can also be analyzed utilizing a 2-D concentration contour plot as shown in Figure 7 for the 60 hour aged 1.56% Si specimen. Contour plots for carbon (from 2 to 6 at.%) and aluminum (from 15 to 21 at.%) are shown in Figures 7 (a) and 7 (b), respectively, and were produced using a 2 nm virtual slice across the z-axis of the box reconstruction volume in Figure 5 (b). κ-carbide is shown to be rich in both carbon and aluminum and the diffuse interface between the matrix and the κ-carbide in Figure 7 (a) is indicative of spinodal decomposition.

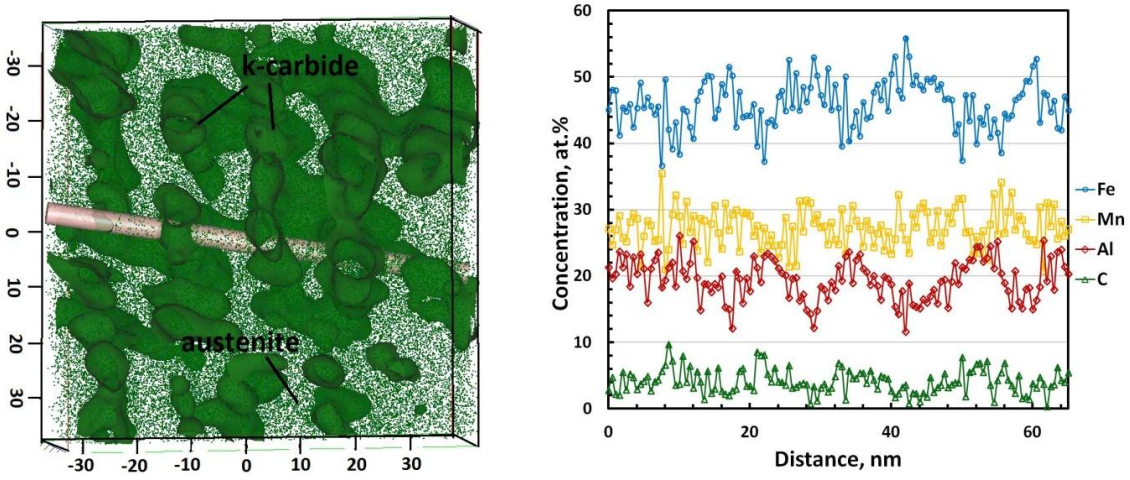

(a) (b)

Fig. 6 (a) Reconstruction of the 1.56%Si specimen which was aged for 60 hours at 530°C shows the location of the 4nm diameter virtual cylinder which was used to generate the concentration profile in (b). (b) The concentration profile appears wave-like with no sharp boundaries between the matrix and the κ-carbide. κ-carbide is enriched with carbon and aluminum and depleted in manganese and iron.

A one dimensional representation of the carbon concentration profile across the x-axis of Figure 7 (a) is shown in Figure 7 (c). The carbon profile is clearly wave-like and consists of many sinusoidal concentration waves that are superimposed upon one another. The average wavelength of the carbon concentration profile was determined to be 15 nm.

A more quantitative analysis of the alloy partioning between the matrix and the κ-carbide was achieved by utilizing a proximity histogram, or proxigram. The proxigram gives the solute concentration as a function of distance from the 4 at.% C isoconcentration surfaces which delineate the κ-carbide from the matrix austenite. Some advantages of this method are that it can accommodate the curvature of non-planar interfaces and the results can be averaged over all of the isosurfaces to reduce statistical error.[28] The proximity histogram concentration profiles of Fe, Mn, Al, C, Si, Mo, and P were determined as a function of distance from the 4 at.%C isoconcentration surfaces. Concentration profiles across the interface of the κ-carbide for the 0.59% Si and 1.56% Si alloys which were aged for 60 hrs at 530° C are shown in Figure 8. Adding silicon is shown to have little effect on the manganese distribution and the κ-carbide is shown to be slightly depleted in manganese for both silicon containing specimens as shown in Figures 8 (a) and 8 (b). However, increasing the amount of silicon from 0.59% to 1.56% Si was shown to increase the amount of carbon in the κ-carbide by almost 1.0 at.% as shown in Figure 8 (c) and (d). The aluminum concentration profile was similar between the two alloys.

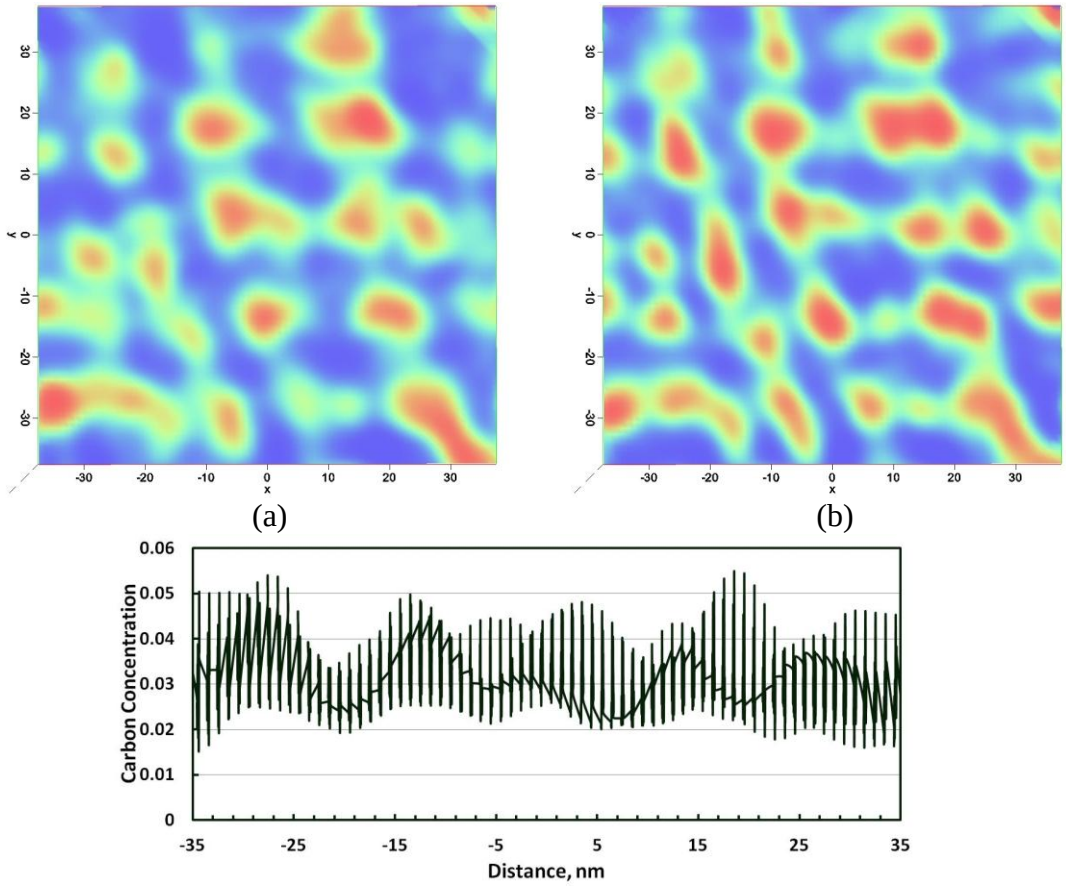

Fig. 7 2-D concentration contour plots taken from a 2 nm slice through the z-axis of the reconstruction volume corresponding to the 1.56% Si specimen that was aged for 60 hrs at 530° C show (a) carbon (2 to 6 at.% - blue to red) and (b) aluminum (15 to 21 at.% - blue to red) "hot spots" that denote the location of κ-carbides. (c) A one dimensional representation of the carbon concentration as a function of distance along the abscissa shows a sinusoidal profile with many composition waves superimposed upon one another.

The κ-carbide is depleted of silicon during aging and increasing the amount of silicon results in the matrix of the 1.56% Si steel being enriched with as much as 4 at.% Si after aging for 60 hrs at 530° C. It is interesting to note that molybdenum was shown to be slightly enriched in the κ-carbide of the 1.56% Si specimen as shown in Figure 8 (d).

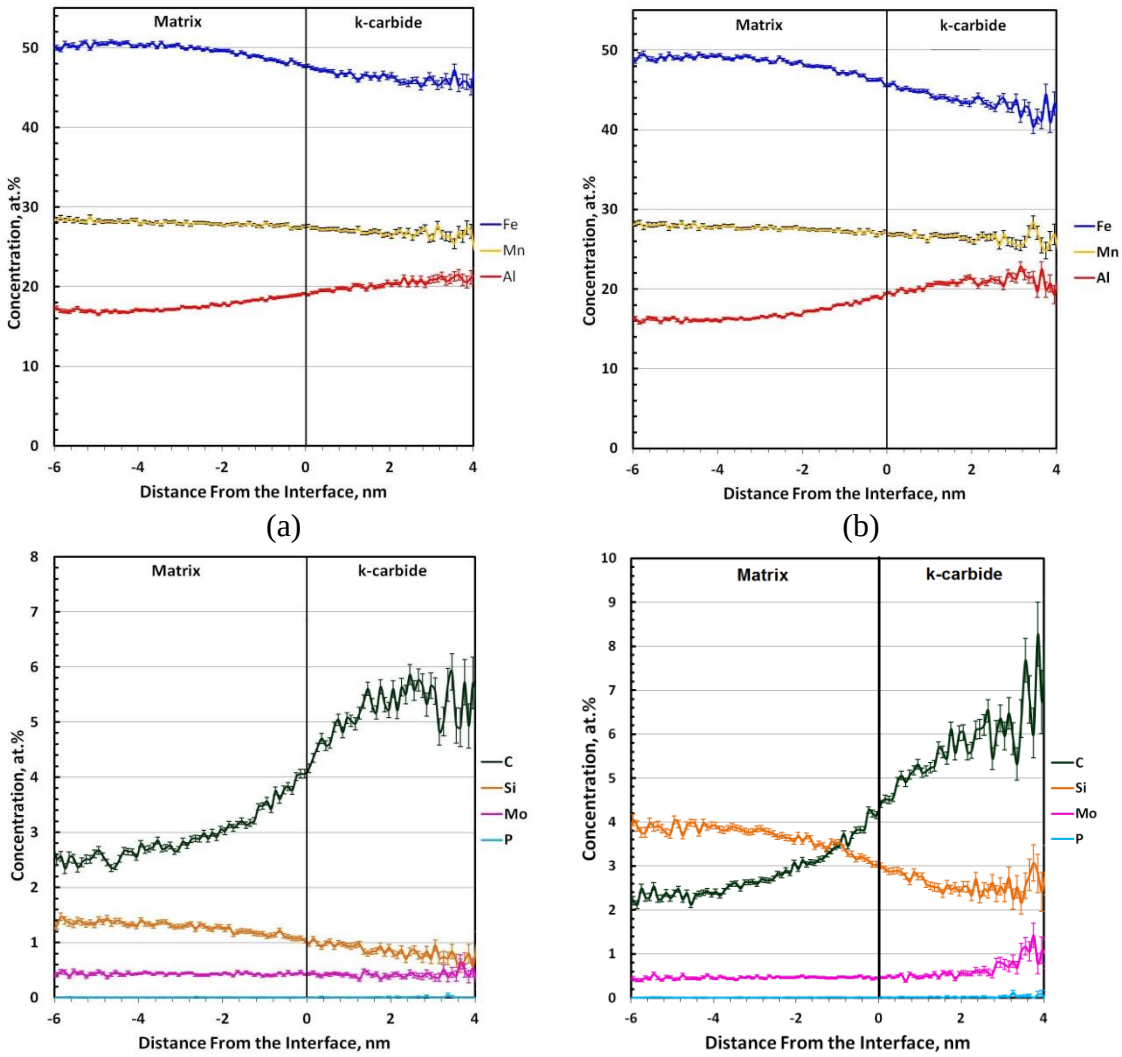

Fig. 8 Concentration profiles of Fe, Mn, and Al with respect to distance from the interface between the κ-carbide and the austenite matrix for the (a) 0.59% Si and (b) 1.56% Si steels aged 60 hrs at 530°C. Increasing the amount of silicon had no effect on the distribution of manganese and the κ-carbide was depleted in manganese regardless of the amount of silicon. The concentration profiles of C, Si, Mo, and P with respect to distance from the interface are shown for the (c) 0.59%Si and (d) 1.56%Si steel aged for 60 hours at 530°C. Increasing silicon from 0.59 to 1.56%Si increased the amount of carbon in the κ-carbide during aging by almost 1.0at.%. (d) After 60 hours of aging, the matrix is enriched with as much as 4at.% Si in the 1.56%Si steel.

Phosphorus appears to be homogeneously distributed in both phases. However, large error in measurement made accurate determination of small changes in phosphorus distribution difficult to quantify as the distance from the isoconcentration surface increased. The κ-carbide and matrix compositions are given in Table 3 and were determined from the average compositions of the plateau regions of the proxigrams as per Miller and Forbes.[28] Increasing the amount of silicon increased the amount of carbon in the κ-carbide from 5.3 to 6.6 at.%.

Table 3. Compositions of the austenite and κ-carbide in atomic percent as determined by LEAP

0.59 wt.% Si aged for 60 hours at 530°C							
Phase	Fe	Mn	Al	C	Si	Mo	P
austenite	50.0	28.4	17.0	2.51	1.36	0.43	0.005
κ-carbide	46.0	26.4	21.1	5.32	0.75	0.43	0.006
1.56 wt.% Si aged for 60 hours at 530°C							
Phase	Fe	Mn	Al	C	Si	Mo	P
austenite	49.1	28.1	16.2	2.30	3.85	0.45	0.010
κ-carbide	42.3	26.3	21.1	6.55	2.57	0.96	0.047

The results of the current study show that after 60 hrs of ageing at 530º C, κ-carbide is non-stoichiometric and may be expressed as $(Fe,Mn)_3AlC_x$ with x = 0.3. Partitioning of alloying elements between the κ-carbide and the matrix was quantified using a ratio of atomic concentration in the precipitate divided by the atomic concentration of the matrix.

A partitioning ratio greater than one indicates partitioning of the solute species to the κ-carbide phase while a value less than one indicates partitioning of solute species to the austenite matrix during aging. Partitioning ratios of solute atoms as determined from the LEAP analysis are given in Table 4. Silicon content is shown to have no effect on the partitioning of manganese and manganese partitioning ratios of 0.9 were determined for all of the alloys. However, increasing the amount of silicon from 0.59 to 1.56% Si was shown to increase the carbon partitioning ratio from 2.1 to 2.9. Silicon was shown to strongly partition to the matrix with a partitioning ratio of 0.6 to 0.7 that was nearly constant between the respective alloys. Aluminum was concentrated within the κ-carbide with a partitioning ratio of 1.2 to 1.3 and was insensitive to silicon content. Molybdenum is shown to be slightly enriched in the κ-carbide of the 1.56% Si specimen with a partitioning ratio of 2.1.

Table 4. Volume fraction of k-carbide and segregation of alloying elements as a function of silicon addition.

		Partitioning coefficients					
Alloy	V_f^{κ}	Fe	Mn	Al	C	Si	Mo
0.59%Si 60 hrs	0.19	0.9	0.9	1.2	2.1	0.6	1.0
1.56%Si 60 hrs	0.18	0.9	0.9	1.3	2.9	0.7	2.1

To elucidate the Si effect in these alloys, first-principles electronic structure calculations were performed. For this, the Vienna simulation package VASP [29,30] was utilized in the projector augmented waves (PAW) formalism and the generalized gradient approximation (GGA) for the exchange-correlation functional [31]. Calculations were performed for the ferromagnetic high spin state of austenite and the equilibrium lattice parameter was determined to be 0.364 nm with a magnetic moment of 2.52 μ_B, which is in good agreement with previous *ab-initio* calculations.[32] Silicon addition was modeled by using a 32-atom supercell for fcc iron and 40-atom supercell composed of 8 unit cells for κ-carbide. It was determined that at a silicon impurity of 3 at.% concentration (Fe31Si) slightly decreases the lattice parameter of both nonmagnetic (NM) and ferromagnetic (FM) austenite from 0.3450 nm (NM) and 0.3641 nm (FM) to 0.3431 nm (NM) and 0.3622 nm (FM). This small decrease of the lattice parameter with Si addition agrees well with the experimental findings reported inTable 5, where a^{γ} reduces by approximately 0.2% per 1wt%Si. The calculated changes in the enthalpy of formation (ΔH) are negative upon 3 at.%Si substitution (-43 meV/atom and -50 meV/atom for NM and FM states, respectively). This points out a stabilizing effect of silicon on the austenite phase. Here it should be noted that silicon is known as a strong stabilizer of ferrite, and the Fe-Si phase diagram contains B2 phase up to 30%Si. For austenitic $Fe_{0.97}Si_{0.03}C_{0.03}$ (Fe31SiC), where carbon is in an octahedral interstitial site and silicon substitutes for iron atoms in the nearest neighbor, next nearest neighbor or most remote positions from carbon, the total energy comparison reveals that silicon prefers to replace Fe atoms far from carbon with a large energy gain of -0.93 eV.

Therefore, the interaction between silicon and carbon atoms is repulsive and, hence, it prevents C from occupying the nearest neighbor positions with Si. A similar repulsive interaction is found between carbon atoms where the second carbon locates in an interstial location remote from the first carbon [33].

The ground state of Fe_3AlC was obtained to be ferromagnetic with an equilibrium lattice parameter of 0.3753 nm. These results are in good agreement with previous theoretical results.[34-38] To determine the preferable site for silicon impurity in κ-carbide, the total energy calculations were performed for $Fe_{2.875}Si_{0.125}AlC$ (Fe23SiAl8C8) and $Fe_3Al_{0.875}Si_{0.125}C$ (Fe24SiAl7C8), where Si atom replaces the Fe and Al atoms, respectively (Table 5). It was found that silicon only slightly changes the lattice parameter of stoichiometric κ-carbide (<0.2% for both Fe and Al substitution), which is in agreement with previous experimental observation[33] where the lattice constant of $E2_1$-Fe_3AlC phase does not show a decrease with the addition of Si.

Table 5. The lattice parameter *a*, and changes in the enthalpy of formation ΔH for the Si substitutions in stoichiometric Fe_3AlC

	Fe_3AlC	$Fe_{2.875}Si_{0.125}AlC$	$Fe_3Al_{0.875}Si_{0.125}C$
a, nm	0.3753	0.3748	0.3746
ΔH, meV/atom	0	+46	+11

It is predicted that silicon will substitute for aluminum (Si^{Al}) and not for iron (Si^{Fe}) in stoichiometric Fe_3AlC with the energy preference for Si^{Al} with respect to Si^{Fe} to be -35 meV/atom. In stoichiometric κ-carbide, the changes in the enthalpy of formation ΔH are positive upon addition of Si atom, and by comparing ΔH in austenite (-50

meV/atom for FM state) and in stoichiometric κ-carbide (+11 meV/atom for Si at the Al sites and +46 meV/atom for Si at the Fe sites), it can be concluded that Si should be partitioned to the austenite matrix.

Experimental results demonstrate that κ-carbide is a nonstoichiometric compound where the carbon deficiency may reach from 50 to 60%.[6,39,40] Additional calculations were performed to consider how carbon vacancies may affect the preferable sites of Si in nonstoichiometric κ-carbide. For nonstoichiometric $Fe_3AlC_{0.875}$ (Fe24Al8C7), a negligible reduction of the lattice parameter with Si addition was obtained and with nearly equal substitution energies for Si impurity in the Fe and Al sites (Table 6). Thus, it can be concluded that carbon deficiency in κ-carbide allows Si to substitute in either the Fe or Al sites.

Table 6. The lattice parameter *a* and changes in the enthalpy of formation ΔH for the Si substitutions in nonstoichiometric $Fe_3AlC_{0.875}$

	$Fe_3AlC_{0.875}$	$Fe_{2.875}Si_{0.125}AlC_{0.875}$	$Fe_3Al_{0.875}C_{0.875}Si_{0.125}$
a, nm	0.3740	0.3735	0.3734
ΔH, meV/atom	0	+11	+8

The lower carbon content in κ-carbide may lead to the vacancy ordering. Modeling of two carbon vacancies in Fe24Al8C6 supercell ($Fe_3AlC_{0.75}$) showed that the Si-vacancy (Si-vac) interaction in κ-carbide is attractive, which favors formation of the <100> vac-Si^{Fe}-vac, <110> vac-Si^{Al}-vac and <111> vac-Si^{Al}-vac complexes. The averaged lattice parameter of $Fe_3AlC_{0.75}$ is equal to 0.3727 nm, 0.3723 nm and 0.3725 nm

for the <100>, <110> and <111> vacancy ordering, respectively, and Si addition changes a^k to 0.3736 nm, 0.3719 nm and 0.3718 nm, when the <100> vac-Si^{Fe}-vac, <110> vac-Si^{Al}-vac and <111> vac-Si^{Al}-vac complexes are formed in $Fe_3AlC_{0.75}$. Thus, it is predicted that the Si^{Fe} substitution increases the lattice parameter of non-stoichiometric κ-carbide, while the Si^{Al} substitution reduces it.

When Si replaces Fe in non-stoichiometric κ-carbide ($Fe_{2.875}Si_{0.125}AlC_{0.75}$ where the vacancies are ordered as <100> vac-Si^{Fe}-vac), the value of ΔH is negative (ΔH = –8 meV/atom) as shown in Table 7, while ΔH is +6 meV/atom and +7 meV/atom for the Si^{Al} substitutions ($Fe_3Al_{0.875}C_{0.75}Si_{0.125}$ with <110> vac-Si^{Al}-vac and <111> vac-Si^{Al}-vac complexes, respectively). This means that the Fe site is more preferable than the Al site for Si impurity due to formation of the <100> vacancy-Si-vacancy configuration (i.e., due to the strong attractive interaction for the nearest-neighbor Si^{Fe}-vacancy). Indeed, the experimental compositions of κ-carbide obtained by LEAP (Table 3) demonstrate a reduction of Fe concentration with increasing silicon content that confirms the above theoretical prediction of the Fe sublattice for Si additions. The negative ΔH obtained for $Fe_{2.875}Si_{0.125}AlC_{0.75}$ shows that silicon stabilizes κ-carbide. This stabilizing effect does not exist in stoichiometric κ-carbide and arises only for carbon concentration less than 75 at% due to the strong Si-vacancy interaction. Nevertheless, the substitution energy for Si is much lower in fcc phase (ΔH = –50 meV/atom) than in κ-carbide (ΔH = –8 meV/atom) and Si is partitioned mainly in austenite matrix, which agrees with previous WDS analysis [41] and our experimental results.

Table 7. The lattice parameter *a* and changes in the enthalpy of formation ΔH for the Si substitutions in nonstoichiometric $Fe_3AlC_{0.75}$ with <100> vacancy ordering

	$Fe_3AlC_{0.75}$	$Fe_{2.875}Si_{0.125}AlC_{0.75}$
a, nm	0.3727	0.3736
ΔH, meV/atom	0	-8

FACTSage thermodynamic modeling software was utilized to determine the effect of silicon addition on the equilibrium amount of κ-carbide in a Fe-30Mn-9Al-0.9C-0.5Mo alloy. κ-carbide was modeled as a solid solution carbide, $(Fe,Mn)_3AlC_x$. The results are shown in Figure 9 for silicon additions of 0.5 and 1.5%.

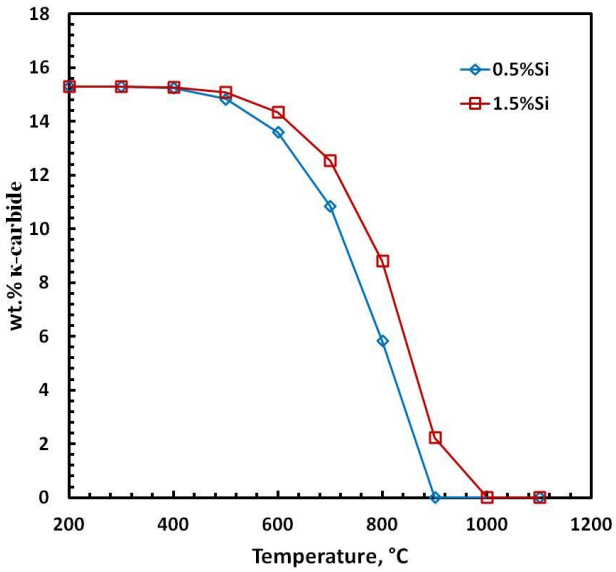

Fig. 9 Thermodynamic modeling of the effect of silicon additions of 0.5 and 1.5%Si on the equilibrium composition of a Fe-30Mn-9Al-0.9C-0.5Mo alloy shows an increase in the stability of κ-carbide with increasing silicon addition.

It is shown that additions of silicon stabilize κ-carbide to higher temperatures. However, the equilibrium amount of κ-carbide can be considered to be insensitive to silicon content at temperatures less than 500° C with a composition of 15 wt.% κ-carbide. Silicon was shown to stabilize κ-carbide by increasing the activity of carbon and thus decreasing the solubility of carbon in austenite.

IV. DISCUSSION

Silicon was shown to slightly increase the size of κ-carbide during both early and later stages of aging as shown in Figures 2 and 3, respectively. Increasing the amount of silicon led to an increase in the wavelength of κ-carbide spacing along <100> from 15 to greater than 20 nm (Figure 3) for specimens aged for 100 hrs at 530° C. The measured wavelengths of modulated κ-carbide in the current study are consistent with previous results by Sato et al. in which the wavelength was determined to be between 10 and 35 nm for Fe-(30-34)Mn-(8-11)Al-(0.9-1.0)C alloys aged for 216 hrs at 550° C.[6] The wavelength has been shown to increase with aging time [6,15,42] and this suggests that the 1.56% Si specimen that was aged for 100 hrs at 530° C is in a more advanced stage of decomposition than the 1.07% Si specimen as shown in Figures 3 (a) and (b), respectively. Han et al.[12] report that diffraction satellites form as result of lattice parameter variations caused by carbon fluctuations along <100> (spinodal decomposition) while the presence of $E2_1$ superlattice reflections are from concurrent ordering of C and Al. The presence of satellite intensity around austenite reflections and the simultaneous existence of $E2_1$ superlattice reflections, as shown in Figure 2, suggests that spinodal decomposition occurs concurrently with ordering of carbon and aluminum. These results are consistent with the work of others suggesting that spinodal

decomposition and ordering are concomitant in Fe-Mn-Al-C alloys.[6,10-13,15] Decreasing the aging temperature to 490° C drastically reduced the kinetics of coarsening and κ-carbide observed in Figure 2 appears randomly distributed after 63 hrs. This is consistent with the isothermal phase transformation diagram for a Fe-28Mn-8.5Al-1C-1.25Si alloy given by Acselrad and co-workers that shows significant delay in κ-carbide coarsening along cube directions at temperatures below 500° C.[14] No evidence of austenite decomposition or short range ordering was observed in the as-quenched state; however, both satellite and superlattice reflections were observed to occur simultaneously from the earliest stages of aging observed during the current study as shown in Figure 2. Thus, it is impossible to determine if spinodal decomposition or short range ordering occurred first.

The κ-carbide lattice parameters as determined from XRD varied from 0.371 to 0.373 nm and these results are consistent with reported lattice parameters between 0.370 to 0.375 nm for κ-carbide precipitation below 700° C in a Fe-28Mn-8.5Al-1C-1.25Si alloy.[14] Increasing both the silicon content as well as the aging temperature was shown to increase the lattice parameter of κ-carbide while simultaneously decreasing the austenite lattice parameter as silicon portioned to the austenite. Increasing the amount of silicon from 0.59 to 1.56% Si increased the unconstrained misfit from 1.41 to 1.97% for alloys aged for 48 hrs at 570° C, as shown in Table 2. Silicon partitioning to the austenite was supported by ab initio calculations presented in this study as well as experimental findings by Huang et al.[42] Silicon has also been shown to stabilize heterogeneous precipitation of $D0_3$ and B_2 intermetallic phases.[14] However, the presence of $D0_3$ or B_2 iron aluminide phases was not detected by TEM or XRD in either of the silicon

containing specimens, even after extended aging for 48 hrs at 570° C, as shown in Figure 4. This is in contrast to the findings of Liu and co-workers that report addition of 1.5% Si to a Fe-29Mn-8Al-0.9C alloy enhanced the formation of $D0_3$ in as-quenched samples.[44] 3-D atom probe tomography determined that silicon content had no affect on the volume fraction of κ-carbide. The volume fraction of κ-carbide was determined to between 0.18 to 0.19 after aging for 60 hrs at 530° C regardless of the amount of silicon. XRD profiles also show no significant variation in the amount of κ-carbide with increasing silicon content (Figure 4). The values of the volume fractions of κ-carbide from the current study can be compared with 20% by volume as determined by XRD as per the results of Kalashnikov et al.[9] for a Fe-28Mn-8.5Al-1C-1.25Si alloy that was aged 16 hrs at 550° C. Thus, the increased hardness with silicon addition cannot be attributed to an increase in the size or volume fraction of κ-carbide nor can it be attributed to the formation of intermetallic phases like $D0_3$. Alternatively, silicon may increase the strength and hardness by increasing the coherency strain between the κ-carbide and the austenite matrix.

It has been suggested that partitioning of manganese into the κ-carbide may increase the strength of κ-carbide by increasing the amount of Mn-C bonds over weaker Fe-C bonds and manganese rich κ-carbides were reported in an atom probe study of a Fe-1.2C-3.2Mn-10Al (in at.%) steel.[27] Additionally, Acelrad et al.[8] reported that the addition of silicon produces a partitioning of manganese from the austenite matrix into grain boundary κ-carbide during aging and a study by Ishida et al.[45] found evidence of homogeneous κ-carbide with a manganese composition 2 to 5% greater than the austenite matrix. However, in the current study, the manganese distribution across the interface of

the matrix austenite and the κ-carbide was nearly homogenous as shown in Figure 8 (a) and (d) and the partitioning coefficient for manganese was determined to be 0.9, meaning slight partitioning of manganese to the matrix. In their study of a mostly ferritic alloy, it was suggested by Seol et al.[27] that the neighboring phase controls the partitioning of manganese and aluminum in κ-carbide. The study by Ishida confirms this to a degree and although they show slight partitioning of manganese into the homogeneous κ-carbide of austenitic alloys, they show significant partitioning of manganese, up to 15% greater, when the neighboring phase to the κ-carbide is ferrite.[45] While it is possible that an increase in the number of Mn-C bonds may increase the strength of κ-carbide, silicon was found to have little effect on the manganese distribution and thus manganese partitioning is not responsible for the increase in hardness with increasing silicon addition.

The only notable effect of silicon on the composition of κ-carbide is that silicon was shown to partition carbon into the κ-carbide during aging. Increasing the amount of silicon increased the amount of carbon in the κ-carbide from 5.32 to 6.55 at.% , as shown in Table 3. This is consistent with a κ-carbide composition of $(Fe,Mn)_3AlC_{x=0.3}$. In comparison, the composition of the lamellar κ-carbide in a study by Seol et al.[27] of a mostly ferritic alloy was found to be $(Fe,Mn)_3(Fe,Al)C_{x=0.7}$ as measured by atom probe tomography. Utilizing X-ray diffraction and an empirical relationsip for the aplitude of spinodal decomposition, Sato et al.[6] calculated a κ-carbide composition of $(Fe,Mn)_3AlC_{x=0.4}$ for a Fe-30Mn-9Al-0.9C-0.03Si (0.016% P) alloy that was aged for 16 hrs at 550° C. It should be noted that the stoichiometric κ-carbide has never been experimentally observed and has only been theoretically addressed using first principles modeling.

As the amount of silicon was increased from 0.59% Si to 1.56% Si, the partitioning coefficient of carbon increased from 2.1 to 2.9 as shown in Table 4. These results are consistent with the work of Acselrad[14] and Bannykh[46] who showed that silicon accelerates carbide precipitation from austenite and raises the activity of C in solid solution. It was additionally reported that C and Si have similar levels of positive charge in relation to iron ions and that they mutually repel each other, which is in agreement with ab initio models in the current study.[46] During aging, increasing the amount of carbon, and to a lesser extent aluminum, in κ-carbide contributes to a continuous increase in the lattice parameter with a simultaneous decrease in the austenite lattice parameter and this produces a greater strain at the interface of the κ-carbide with the matrix.[6,15] Increasing the amount of silicon in the matrix would further decrease the austenite lattice parameter during aging and contribute to a greater misfit between the κ-carbide and the matrix. Sato et al.[6,15] showed that the increase in strength and hardness in Fe-Mn-Al-C alloys during aging is related to the increase in the amplitude of the carbon concentration which increases the strain amplitude as a function of time.

Figure 1 shows an increase in hardness for a fixed aging time as the silicon is increased and this increased hardness may be explained by the change in carbon amplitude during spinodal decomposition. A theory of spinodal hardening presented by Kato et al.[47] considered the increase in strength during aging to be the result of coherency stress associated with the growth in the composition amplitude. Thus, it is proposed that the increase in the carbon content of κ-carbide with increasing silicon content is responsible for the higher hardness at a fixed aging time.

The extent of hardening with increasing silicon in the current study may be evaluated using the concentration amplitude of carbon determined from the atom probe analysis according to the model by Kato et al. given below.[47]

$$\Delta\tau_Y = \frac{\varepsilon}{\frac{1}{6^{\frac{1}{2}}}}\,(C_{11} - C_{12}) \qquad (1)$$

$$\varepsilon = \frac{A\eta(C_{11}+2C_{12})}{3C_{11}} \qquad (2)$$

Where $\Delta\tau_y$ is the increase in the shear stress, ε is the strain amplitude, and *A* is the concentration amplitude of carbon which was measured to be 5.32 at.% and 6.55 at.% for the 0.59 and 1.56% Si specimens that were aged for 60 hrs at 530° C. C_{11} and C_{12} are elastic coefficients of the matrix and were taken to be 14.4×10^{10} and 8.7×10^{10} N/m^2 which were used by Sato et al.[6] to accurately model increases in the yield strength during aging of a Fe-29.5Mn-9.2Al-0.94C steel. It should be noted however that these values were taken from the work of Salama and Alers and were determined for a single crystal of Fe-30Ni .[48]. The parameter η is the change in the lattice parameter as a function of increasing carbon concentration and $\eta = da/dC \cdot 1/a$. The change in the lattice parameter with increasing carbon content was determined by Sato et al.[6] to be 0.18 using the data of Charles et al.[49] for a similar Fe-30Mn-9Al-0.9C-0.03Si (0.016% P) alloy. As a comparison, a η value for the change in the κ-carbide lattice parameter with increasing carbon content was predicted to be 0.2 by extrapolating the data in Table 2. This is very close to the value of 0.18 used in the Sato[6] study. Multiplying $\Delta\tau_y$ by an appropriate

Taylor factor of 3.06 gives the change in the yield strength due to spinodal hardening. The increase in yield strength after aging for 60 hrs at 530° C was predicted to be 500 and 620 MPa for the 0.59 and 1.56% Si alloys, respectively. These calculated values can be directly compared with the tensile properties in Table 8 obtained by Bartlett et al.[5] for the same 1.07 and 1.56% Si composition alloys used in the current study. Table 5 shows that after 60 hrs of aging at 530° C, the yield strength increases by almost 500 MPa in the 1.56% Si alloy which can be compared with a 620 MPa increase in the yield strength as predicted by the hardening model by Kato. [47]

Table 8. Mechanical properties of the 1.07 and 1.56% Si alloys as obtained by Bartlett et al.[5]

wt.% Si	Heat Treatment	Hdns, BHN[a]	0.2% YS, MPa	UTS, MPa	% Elong.[b]
1.07	Solution treated	197	452	737	64
1.56	Solution treated	208	450	733	64
1.07	Aged 60 hrs at 530°C	350 ± 3	873 ± 17	953 ± 25	20.1 ± 10.1
1.56	Aged 60 hrs at 530°C	360 ± 6	937 ± 8.9	1016 ± 2.5	13.2 ± 4.2

[a]Hardness Brinell (3000 kg) were converted from Rockwell B and C scale measurements
[b] % elongation was measured in a 25.4 mm (1 inch) gage length
Uncertainty reported for test sample greater than 2 and represents one standard deviation

In the solution treated condition, the mechanical properties are nearly identical regardless of silicon content. However, in the 60 hr aged condition, increasing the silicon content by 0.5 wt.% increased the yield strength by 64 MPa. The spinodal hardening model by Kato[46] predicts a 120 MPa increase in the yield strength with a 1 wt.% increase in silicon for specimens aged for 60 hrs at 530° C. Within experimental error, the spinodal hardening mechanism is in reasonable agreement with the experimental results presented here as well as those presented by Sato et al.[15]

V. SUMMARY

For specimens aged for 60 hrs at 530° C, it was determined that silicon increases the size of κ-carbide precipitated, but not the volume fraction precipitated.. Silicon was found to have little effect on the distribution of manganese and the κ-carbide was depleted of manganese regardless of silicon content; thus, the increase in hardening was not associated with changes in manganese content. Both experimental results and ab initio calculations show that there is a repulsive interaction between carbon and silicon and carbon prefers to be far away from silicon in solution. Silicon was found to partition to the austenite during aging and silicon increased the activity of carbon in austenite. Increasing the silicon content from 0.59 to 1.56 wt.% was found to increase the partitioning of carbon in the κ-carbide from 5.2 to 6.6 at.%. The results of this study suggest that the increase in strength during aging of high manganese and aluminum steels is directly related to the increase in the compositional amplitude of carbon with silicon addition. A theory of spinodal hardening was used to calculate the expected increase in strength during aging with increases in the carbon concentration amplitude. The model predicted a 120 MPa increase in strength with a 1wt.% increase in silicon for alloys aged

for 60 hrs at 530° C and this is in reasonable agreement with previously determined mechanical property data.

ACKNOWLEDGMENTS

This work was supported in part by Army Research Laboratory under contracts from Battelle Memorial Institute (contract W911NF-07-D-0001) and Benet Laboratories (contract W15QKN-07-2-0004) and a grant from Northwestern University Center for Atom Probe Tomography. Laura Bartlett was also supported by a U.S. Department of Education GAANN fellowship under contract P200A0900048. The FEI Tecnai F20 scanning/transmission electron microscope was obtained with a Major Research Instrumentation grant from NSF under contract DMR-0922851. The authors also gratefully acknowledge Waukesha Foundry, Inc. for providing the low phosphorous Fe-Mn-Al-C alloys and the alloys with varying Si content.

REFERENCES

1. R.A. Howell, S.L. Lekakh, D.C. Van Aken, V.L. Richards, AFS Trans., 2008, vol. 116, pp. 867-878.

2. G. Frommeyer and U. Brux, Steel Research Int., 2006, vol. 77, pp. 627-633.

3. R. Howell, T. Weerasooriya, and D. Van Aken, Tensile, 2008, AFS Trans., (2008).

4. G.L. Kayak, 1969, Met. Sc. And Heat Tr., vol. 11, pp. 95-97

5. L. Bartlett, R.A. Howell, A. Schulte, D. Van Aken, and K. Peaslee, 2010, MS&T Confer. Proceed. Houston TX.

6. K. Sato, K. Tagawa, and Y. Inoue, 1990, vol. 21A, pp 5-11.

7. G.E. Hale, A. J. Baker, 1986, Conf. on Alt. Alloying for Env. Res. New Orleans, LA.

8. O. Acselrad, I.S. Kalashnikov, E.M. Silva, R.A. Simao, C.A. Achete, L. Pereira, 2002, Met. Trans. A, vol. 33, pp. 3569-3572.

9. I.S. Kalashnikov, O. Acselrad, A. Shalkevich, Chumakova, and L.C. Pereira, 2003, Journal of Mat. Process. Tech. Vol. 136 pp. 72-79.

10. K. Sato, Y. Igarashi, Y. Inoue, T. Yamazaki, and M. Yamanaka, 1991, Proceed. of the Inter. Confer.on Stain. Steels, pp. 503-509.

11. W.K. Choo and J.H. Kim, 1997, Conf. on Thermo-mechanical Process.of Steels and Other Mats., pp. 1631-1637.

12. K.H. Han, J.C. Yoon, and W.K. Choo, 1986, Scripta Metall., vol 20, pp. 33-36.

13. O. Acselrad, L.C. Pereira, M.R. Amaral, 1992, Proceedings of Proc. and Prop. of Mats., pp. 829-834.

14. O. Acselrad, I.S. Kalashnikov, E.M. Silva, M.S. Khadyev, and R.A. Simao, 2006, Metal Science and Heat Treatment vol. 48, pp. 543-553.

15. K. Sato, K. Tagawa, and Inoue, 1989, Mat.Science and Engineering A 111 pp. 45-50.

16. L. Bartlett, R. Howell, D. Van Aken, and K. Peaslee, 2010, AFS Trans., vol. 118, pp. 413-423.

17. C.Y. Chao and T.F. Liu, 1991, Scripta Metall., Vol. 25 pp. 1623-1628.

18. C. Hwang, C. Chao, T. Liu, 1993, Scripta Metal. et Mat. vol. 28, pp. 263-268.

19. C. Chao, C. Hwang, and T. Liu, 1993, Scripta Metal. et Mat. vol. 28, pp. 109-114.

20. D. Isheim, R. Prakash, M. Fine, and D. Seidman, 2006, Scripta Mat. Vo. 55 pp. 35-40.

21. A. Murthy, J. Medvedeva, D. Isheim, S. Lekakh, V. Richards, and D. Van Aken, 2012, Scripta Mat.vol. 66 pp. 943-946.

22. K. Knipling, R. Karnesky, C. Lee, D. Dunand, and D. Seidman, 2010, Acta Materialia, vol. 58 pp. 5184-5195.

23. T. Kelly, and M. Miller, 2007, Review of Scientific Instruments, vol. 78 pp. 031101 1-20.

24. L. Johnson, M. Thuvander, K. Stiller, M. Oden, and Hultman, 2012, Thin Solid Films vol. 520, pp. 4362-4368.

25. W. Xiong, J. Agren, and J. Zhou, 2012, Cond. Matter and Mat.Science.

26. D. Saxey, M. Apperley, R. Zheng, T. Honma, S. and Ringer, 2006, Mat. Forum vol. 30 pp. 85-89.

27. J. Seol, D. Raabe, P. Choi, H. Park, J. Kwak, and C. Park, 2012, Submitted to Scripta Mat.

28. M. Miller, and R. Forbes, 2009, Mat. Characterization vol. 60 pp. 461-469.

29. G. Kresse, and J. Hafner, 1994, J. Phys. Condens. Matter vol. 6 pp. 8245-8257.

30. G. Kresse, and J. Furthmuller, 1996, Phys. Rev. B vol. 54 pp.11169-11186.

31. J.P. Perdew, K. Burke, and M. Ernzerhof, 1996, Phys. Rev. Lett. vol. 77 pp. 3865-3868.

32. H.C. Herper, T. Hoffmann, and P. Entel, 1999, Phys. Rev. B vol. 60 pp. 3839-3848.

33. H.M. Lee, 1974, Metal Trans, vol.5 pp. 787-789.

34. P. Willars, A. Prince, H. Okamoto, Handbook of Ternary Alloy Phase Diagrams, vol. 3

35. M. Ruda, D. Farkas, J. Abriata, 2002, Scr. Mater. Vol. 46 pp. 349-345.

36. P. Maugis, J. Lacase, R. Besson, J. Morillo, 2006, Metal Mater Trans A vol. 37 pp. 3397-3401.

37. A. Kellou, T. Grosdidier, J. Raulot, H. Aourag, 2008, Phys. Stat. Sol. B vol. 245 pp. 750-755.

38. B.V. Reddy, S.C. Deevi, 2002, Mater. Sci. Eng. A vol. 329-331 pp. 395-401.

39. M. Palm, G. Inden,1995, Intermetallics vol. 3 pp. 443-454.

40. J.Yang, P. Laa, W. Liu, and Y. Hao, 2004, Mat. Sci. and Eng. A vol. 382 pp. 8-14.

41. H. Ishii, S. Miura, and T. Mohri, 2002, MRS Proceedings vol. 753 p. BB5.29.

42. K.H. Han, W.K. Choo, D.Y. Choi, S.P. Hong, 1987, TMS-AIME, pp. 91-106.

43. H. Huang, D. Gan, and W. Kao, 1994, Scripta Metal. et Mat. vol. 30, pp. 499-504.

44. T. Liu, J. Chou, and C. Wu, 1990, Met. Trans. A vol. 21 pp. 1891-1899.

45. K. Ishida, H. Ohtani, S. Naoya, R. Kainuma, T. Nishizawa, 1990, ISIJ, vol. 30, pp. 680-686.

46. O. Bannykh, 1969, Fiz. Metal metalloved.vol. 27, pp. 837-841.

47. M. Kato, T. Mori, and L. Schwartz, 1980, Acta Metall. vol. 28. Pp. 285-290.

48. K. Salama, and G. Alers, 1968, Journal of App. Phys. vol. 39, pp. 4857-4859.

49. J. Charles, A. Berghezan, and A. Lutts, 1984, J. Phys., Colloq., vol. 45, pp. C1-619-623.

PAPER

3. Atom Probe Tomography Study of the Precipitation of κ-carbide in Fe-Mn-Al-C Alloys Part II. Influence of Phosphorus

L.N. Bartlett, D.C. Van Aken, D. Ishiem, J. Medvedeva, N. Medvedeva, and K. Song

Missouri University of Science and Technology

Department of Materials Science and Engineering

Rolla, MO 65409

Tel.: 573-341-4717

E-mail: dcva@mst.edu

Key Words: Fe-Mn-Al-C, lightweight steel, age hardenable, atom probe tomography, phosphorus

To be submitted to Metallurgical and Materials Transactions A

The influence of phosphorus on κ-carbide precipitation and alloy partitioning in Fe-30Mn-9Al-1Si-0.9C-0.5Mo cast steel was studied utilizing transmission electron microscopy, 3-D atom probe tomography, and X-ray diffraction. Increasing the amount of phosphorus from 0.006 wt.% to 0.043 wt.% increased the kinetics of the initial ordering reaction and specimens from the high phosphorus material showed some degree of short range ordering that took place during the quench and prior to any other stage of transformation. It was shown that phosphorus increases both the size and volume fraction of κ-carbide during aging. However, the distribution of phosphorus was found to be homogeneous and thus long-range diffusion of phosphorus was not responsible for the observed increase in hardening. It is suggested that phosphorus encourages short range order and accelerates spinodal decomposition.

I. INTRODUCTION

Lightweight steels in the Fe-Mn-Al-C system are being considered for high energy absorbing applications in the transportation industry[1] as well as for military cast armor.[2] Adding aluminum reduces the density and at a composition of Fe-30Mn-9Al-1Si-0.9C-0.5Mo, these steels are 15% less dense than quench hardened and tempered 4130 cast steels while still retaining equivalent mechanical properties.[3] All compositions in the following text are expressed as weight percent unless otherwise specified. Steels that contain from 5-11 wt.% aluminum and from 0.3-1.2 wt.% carbon are precipitation hardenable when heat treated in the range of 450 to 700° C.[1,2,4]

Mechanical strength properties in these alloys are increased by age hardening. Strengths as high as 2000 MPa and Charpy V notch (CVN) breaking energies as high as 221 J at room temperature have been reported for solution treated and coldworked alloys.[5,6] Solution

treated cast alloys also have high work hardening rates and can attain strengths as high as 737 MPa with total elongations greater than 64%.[7] Aging greatly increases the strength of cast Fe-Mn-Al-C alloys to greater than 1000 MPa.[7] However, increasing the degree of age hardening decreased the dynamic fracture toughness from 419 to 166 kJ/m^2 as previously reported in a Fe-30Mn-9Al-1Si-0.9C-0.5Mo (0.001% P) steel that was aged between 13 and 60 hrs at 530° C.[3]

Age hardening is the result of homogeneous and coherent precipitation of nano-sized κ-carbide, $(Fe,Mn)_3AlC_x$, which has the $E2_1$ crystal structure in which aluminum occupies corner positions, iron and manganese occupy face positions, and carbon is at the body center interstitial octahedral site. κ-carbide has a cube on cube orientation relationship with the austenitic matrix with $<100>_\kappa//<100>_\gamma$ and $\{001\}_\kappa//\{001\}_\gamma$.[8-12] The κ-carbide is a non-stoichiometric intermetallic carbide in which the carbon deficiency can range up to 50%. There is some ambiguity in literature as to the exact stages leading to the formation of κ-carbide. It is generally accepted that first stage hardening in *Fe-Mn-Al-C* alloys is the result of compositional modulation which is accomplished by spinodal decomposition into carbon rich[6,12-14] or carbon and aluminum rich[8,10,11,15] and depleted zones. Chemical modulation is followed by precipitation of κ-carbide and coarsening with morphological alignment along austenite <100>.

Short range ordering is suggested to occur concurrently with spinodal decomposition by some authors[6,8,12-14,16] and to follow spinodal decomposition by others.[10,11] Evidence of pre-clustering in the as-quenched state has been reported by some to suggest that short range ordering may precede spinodal decomposition.[15,17,18] In a study by Karakishev et al. evidence was shown of $E2_1$ superlattice reflections in an as-

quenched Fe-29Mn-9.3Al-0.95C-0.71W-0.42Nb-0.37Mo steel and using nuclear gamma resonance methods, they showed SRO of aluminum in the solid solution austenite.[19] It has been suggested that short range ordering is responsible for the absence of an incubation time during the first stage of age-hardening.[15] Additionally, Prodhan et al. report hardening in Fe-30Mn-(5-10)Al-(1.5-1.7)Si-(2.7-0.91)C cast alloys to be the result of first stage ordering into a $L1_2$ type superlattice (Fe_3Al) followed by subsequent precipitation and growth of κ-carbide to be purely an ordering reaction followed by particle coarsening.[20] In part I of the current study, which discusses the effect of silicon on age hardening of a Fe-30Mn-9Al-0.9C-0.5Mo steel, superlattice reflections were not observed in the electron diffraction patterns of as-quenched specimens; however upon aging, superlattice reflections were observed in combination with satellite reflections and this suggests that the ordering reaction occurs concurrent to spinodal decomposition.[21]

Phosphorus has been shown to promote a brittle, cleavage fracture in cast steels. In amounts greater than 0.006% P, phosphorus has been shown to decrease notch toughness by up to 80% in an aged Fe-30Mn-9Al-1Si-0.9C-0.5Mo steel.[7,22] First principles calculations have shown that substitution of phosphorus for aluminum positions in the κ-carbide is most favorable and creates open volume defects on {100} when a stress is applied normal to the plane. Phosphorus substitution for aluminum in the κ-carbide structure as previously reported by Medvedeva et al.[23] relaxes the local bonding character along the $<100>_\kappa$ as shown in Figure 1 (a). This results in a 45% reduction in the cleavage stress of the κ-carbide and is predicted to be the mechanism behind phosphorus decreasing the notch toughness in aged Fe-Mn-Al-C steels.[23]

Phosphorus greatly increases the hardening rate in these steels.[23] Age hardening curves for Fe-30Mn-9Al-1Si-0.9C steels with from 0.001% to 0.043% phosphorus are shown in Figure 1 (b) for specimens aged at 530°C.[24] Phosphorus is shown to increase both the hardness during aging as well as the hardening rate.[24] Increasing the amount of phosphorus from 0.001% to 0.018% P and greater was shown to decrease the activation energy for the hardening process from 300 to 180 kJ/mol, which is in good agreement with the activation energy for bulk diffusion of phosphorus in austenite.[24] Therefore, on the basis of experimental work and first principles modeling, it has been proposed that phosphorus increases both the initial spinodal decomposition rate as well as the precipitation and growth of κ-carbide and that this is related to diffusion of phosphorus into κ-carbide.[24] However, direct evidence of phosphorus partitioning has not been reported in the literature.

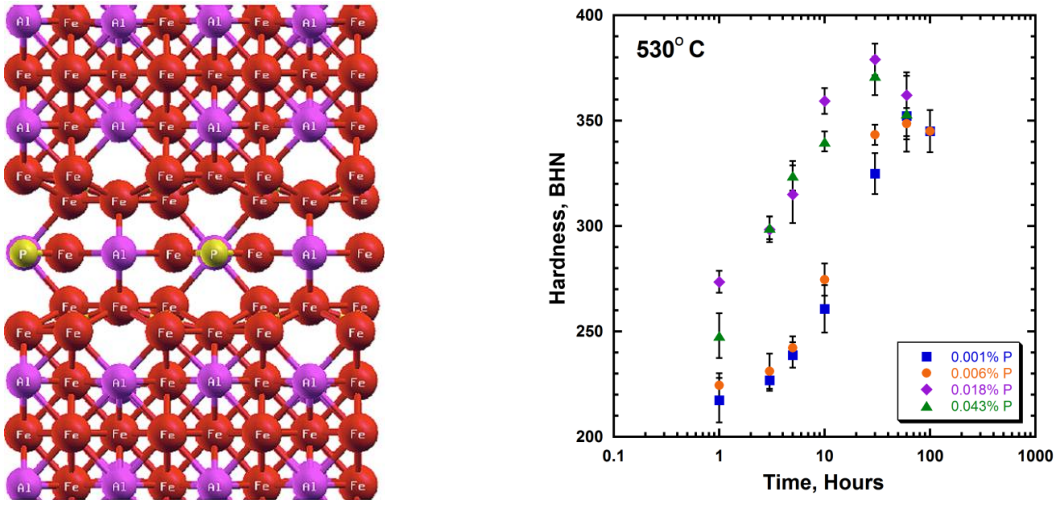

(a) (b)

Fig. 1 (a) The (101) projection of the $E2_1$ κ-carbide shows relaxation of the Fe-P bonds when phosphorus substitutes for aluminum corner positions.[23] (b) Increasing the amount of phosphorus in a Fe-30Mn-9Al-1Si-0.9C-0.5Mo steel greatly increased the hardening rate for steels aged at 530° C.[24]

In recent years, 3-D atom probe tomography has emerged as a powerful tool for determining compositions across interfaces with sub-nanometer resolution. This has mainly been the result of increases in computing power and data collection rates as well as significant increases in the field-of-view with the advent of the local electrode atom probe.[25] Local electrode atom probe (LEAP) tomography has been used to characterize many systems that undergo spinodal decomposition , e.g. Ti-Al-N thin films[26], Fe-Cr binary alloys,[27] and Fe-Ni-Mn-Al alloys .[28] LEAP has also been used to validate thermodynamic models and the spinodal compositions in the Fe-Cr system.[29] Most recently, LEAP has been used to determine the composition of lamellar κ-carbide in a mostly ferritic Fe-3.2Mn-10Al-1.2C (in at.%) alloy.[30]

In part one of the current study the authors have shown using LEAP that silicon increases the activity of carbon in solid solution austenite and partitions carbon into the κ-carbide during aging.[21] For this study, the effect of phosphorus on the size, composition, and distribution of κ-carbide during aging in an Fe-30Mn-9Al-1Si-0.9C-0.5Mo steel is investigated.

II. EXPERIMENTS

Lightweight steels were cast with a nominal chemistry of Fe-30%Mn-9%Al-1%Si-0.9%C-0.5%Mo. A high phosphorus steel with greater than 0.018% was prepared using a new furnace lining and utilizing ferromanganese without calcium addition or Ar-stirring. Ferromanganese will contribute as much as 0.018% phosphorous if fully recovered during alloy preparation. Additional phosphorus pickup can come from the furnace refractory that contain phosphate bonding agents. Steels with low phosphorus were made using electrolytic manganese, melted using a used furnace lining, and were

calcium treated followed by Ar-stirring prior to tapping. All heats were prepared in an induction furnace under argon cover. Horizontal plate molds were prepared from phenolic no-bake olivine sand. The thickness of the plates measured between 1.5 and 1.9 cm. All chemical analyses were performed by ion coupled plasma spectrometry after sample dissolution in perchloric acid and are listed in Table 1. Specimens containing low phosphorus and different silicon contents from part I of this study are also shown in Table 1.

Table 1. Steel chemistries in weight percent.

Si	C	Mn	P	S	Mo	Al	Cu
1.01	0.89	30.20	0.006	0.001	0.31	8.85	-----
0.92	0.94	29.10	0.043	0.006	0.33	8.28	0.09
0.59*	0.95	30.35	0.002	0.006	0.54	8.74	0.01
1.07*	0.90	30.42	0.001	0.006	0.53	8.83	0.006
1.56*	0.89	29.97	0.002	0.007	0.53	8.81	0.006

* Previously reported from ref. 21.

Approximately 1.5x1.5x2.0cm rectangular test coupons were machined from the center of the cast plates. Each alloy was solution treated for 2 hrs at 1050° C in protective stainless steel bags. Specimens were individually water quenched into agitated room temperature water. Aging was conducted in a salt pot containing a mixture of sodium and potassium nitrate. The variation in temperature during aging was +/- 5°C. Thin foils for transmission electron microscopy were prepared using a solution of 6% perchloric acid, 60% methanol, and 34% butoxyethanol and a twin jet electropolisher

operating at -20°C utilizing and a DC current of 30-40 mA. Thin foils were analyzed using a Tecnai F20 TEM operating at 200 kV. LEAP specimens were prepared by machining 0.3x0.3x10mm rectangular blanks from the center of the solution treated and aged plates. Rectangular blanks were electropolished at room temperature in a two step polishing procedure. Initial thinning of the specimen to 0.2 mm in diameter was performed 20 V DC in a 10% perchlorc acid 90% acetic solution. Final polishing was accomplished utilizing a solution of 2% perchloric acid solution in butoxyethanol at 12 V DC to produce a tip radius less than 100 nm. Polished tips were analyzed using a local electrode atom probe tomograph manufactured by Cameca, Madison, WI. Tips were held in a vacuum of $6.5X10^{-11}$ torr at a temperature of 60 K. A 0.5% evaporation rate was obtained at 500 kHz using 20 pJ laser pulse energy. Between 20 million and 500 million atoms were detected from each of the respective specimens. IVAS 3.6 software was utilized to construct a 3-D atom-by-atom representation of each specimen.

Specimens for X-Ray diffraction experiments were produced from bulk specimens that were polished to a 6 μm finish. Specimens were analyzed at room temperature utilizing a PANalytical X-PertPro diffractometer with Cu-kα radiation operating at 45 kV with a tube current of 40 mA. A nickel monochromator was utilized to filter out Cu-kβ radiation. Specimens were scanned over an angular range of 20 to 80° 2θ at a rate of 1/8° min^{-1}.

III. RESULTS

In the following text, the different alloys will be referred to by their phosphorus contents in weight percent as listed in Table 1. It should also be noted that compositions given by LEAP will be given in atomic percent. Thin foils were prepared from selected

specimens to directly show the influence of phosphorus on the morphology, size, and distribution of κ-carbide as a function of aging time and temperature. Figures 2 (a) and 2 (b) show the bright field images of the as solution treated and quenched specimens from the 0.006% P and 0.043% P steels. In the 0.006%P specimen, there is no evidence of austenite decomposition in the image and the corresponding [111] selected area diffraction pattern (SADP) shows no evidence of satellite or superlattice reflections.

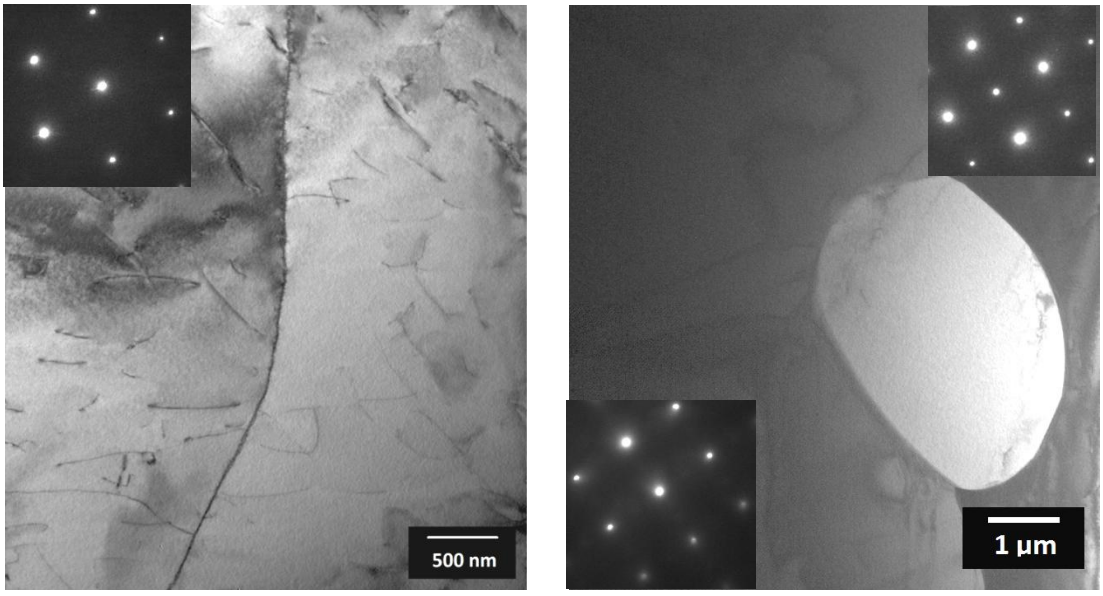

(a) (b)

Fig. 2 Bright field images of the (a) 0.006%P and (b) 0.043%P specimens in the as-solution treated condition. (a) The low phosphorus alloy shows dislocations in the microstructure but no evidence of satellite or superlattice reflections in the corresponding [111] zone diffraction pattern. (b) In contrast, the 0.043%P alloy shows diffuse superlattice reflections in the corresponding [001] zone diffraction pattern (bottom left inset) (b) The light contrast phase is DO_3, Fe_3Al, on an austenite grain boundary triple point as evidenced by the corresponding [001] zone diffraction pattern in the upper right corner of the image.

A solution treated and quenched specimen of the high phosphorus alloy is shown in Figure 2 (b). Figure 2 (b) shows a bright contrast phase on an austenite grain boundary triple point in the as-solution treated 0.043% P specimen. This phase was determined to be $D0_3$, Fe_3Al, with a lattice parameter of 0.579 nm as evidenced by the corresponding [001] SADP in the upper right corner of Figure 2 (b). The [001] SADP for the surrounding matrix austenite is shown in the lower left corner of Figure 2 (b) and shows diffuse $E2_1$ superlattice reflections that indicate SRO of Fe-Al-C. Dark-field images using the superlattice were of insufficient intensity to discern any precipitates. Absence of satellite reflections around main austenite reflections suggests that spinodal decomposition has not taken place and that short range ordering of Fe-Al-C may have occurred in the solution treated material. Figures 3 (a) and 3 (b) are bright field and dark field electron micrographs, respectively, of a 0.006%P specimen that was solution treated and aged for 10hrs at 530°C. The bright field image shows strain contrast in cube directions and the corresponding [001] zone axis diffraction pattern shows satellite reflections around main austenite reflections. A detail image of the austenite [400] shows satellite reflections in cube directions as shown in the bottom left corner of Figure 3 (a). Such satellites indicate a slight change in the austenite lattice parameter due to differences in the austenite composition along <100> and are evidence of spinodal decomposition. The dark field image in Figure 3 (b) was generated utilizing the [100] superlattice reflection in the corresponding SADP in Figure 3 (a) and shows a high number density of ordered domains that are less than 1 nm in diameter and randomly distributed throughout the austenite matrix.

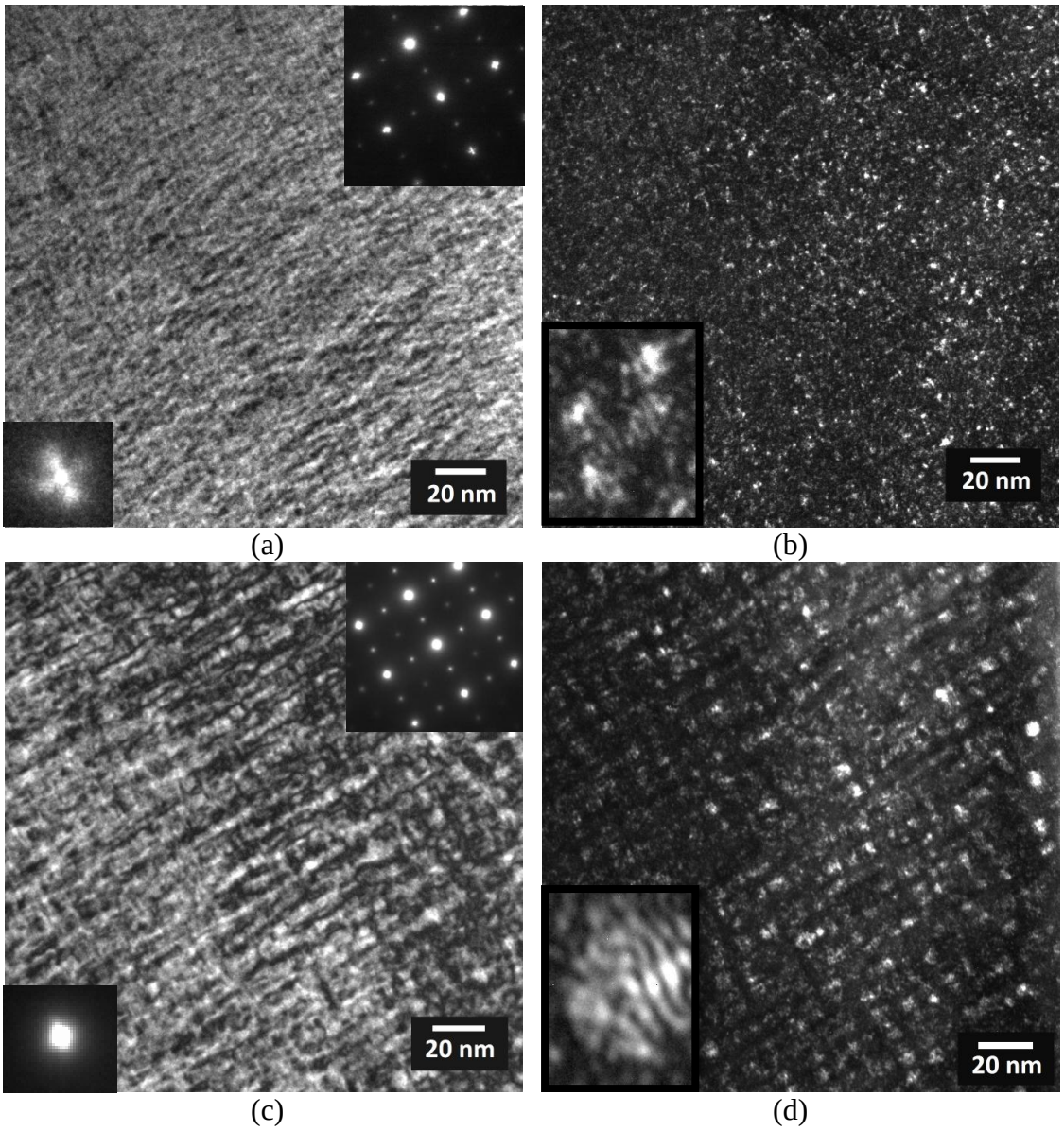

Fig. 3 (a) Bright field image and corresponding [001] zone diffraction pattern of the 0.006%P alloy that was aged for 10 hrs at 530° C shows strain contrast that is modulated in cube directions. The strain contrast is the result of spinodal decomposition of the austenite along <100> as evidenced by the satellite reflections around the austenite [400] spot in the lower left-hand corner of (a). (b) The dark field image of the same region in (a) shows a high number density of fine (<1 nm) ordered regions that are randomly distributed throughout the austenite matrix and are coarsening into clusters that are on the order of 2-3 nm (bottom left inset image). (c) The bright field image of the 10 hr aged (530° C) high phosphorus 0.043% P specimen and corresponding [001] diffraction pattern shows strain contrast that is the result of growing κ-carbide along <100>. Spinodal satellites are much closer to the austenite [400]. (d) The [001] dark field image of the same area as in (c) shows a high number density κ-carbide that is arranged along cube directions and coarsening into a cuboidal morphology.

The $E2_1$ ordered regions appear to be particles that are no larger than 2-3 nm in diameter as shown in the bottom inset image in Figure 3 (b). The bright field image of the 10hr aged 0.043%P specimen is shown in Figure 3 (c) with the corresponding [001] SADP. Strain modulation along cube directions is much stronger than in the low phosphorus specimen and is the result of preferential coarsening of κ-carbide along <100>. The inset image in Figure 3 (c) shows that after 10hrs of aging at 530° C, satellites can barely be distinguished around the fundamental austenite [400] diffraction spot in the high phosphorus specimen. As the spinodal decomposition reaction proceeds, the position of satellite diffraction intensities will move closer to the fundamental austenite reflections. Thus the diffraction patterns could be interpreted to indicate that the high phosphorus specimen is in a later stage of decomposition when compared with the 10 hr aged 0.006% P specimen in Figure 3 (a). The dark field image of the 0.043% P specimen is shown in Figure 3 (d) and shows high number density of κ-carbides that are much larger with an average particle size of 5 nm. κ-carbides are clearly periodic and arranged along cube directions. The extent of coarsening of the κ-carbide can also be described in terms of a growing wavelength, λ, of the modulated structure measured from the center of the κ-carbide to the center of the next κ-carbide along <100>. The wavelength of the modulations in the 0.043% P specimen was an average of 10 nm with a particle size (measured along the cube edge) of 5 nm as shown in Figure 3 (d). At this stage of coarsening, κ-carbides are adapting a cuboidal morphology and the bottom inset image of Figure 3 (d) shows that the cuboids are composed of <1 nm thick chains or disks of ordered zones that are periodic along a cube direction which is characteristic of systems with a high degree of elastic anisotropy.

The structure of the high and low phosphorus Fe-Mn-Al-C steels in both the solution treated and aged condition was evaluated using x-ray diffraction. Evidence of spinodal decomposition will manifest itself in the form of sidebands around fundamental austenite reflections that grow in intensity and move closer to the main Bragg angle as decomposition progresses.[8] It should be noted that sidebands in XRD profiles are analogous to satellite reflections in electron diffraction patterns, however they tend to form only after extended aging for periods greater than 180 min at 550° C after spinodal satellites in electron diffraction patterns have moved so close to fundamental reflections that their spacing cannot be determined[18] In the solution treated condition, both the 0.006% P and 0.043% P steels showed no evidence of decomposition and only fundamental austenite peaks are observed as shown for an as-solution treated and quenched 0.043% P specimen in Figure 4 and Figure 5 (a) After aging for 10 hrs at 530° C, only the 0.043 phosphorus specimen showed evidence of spinodal decomposition in the form of sidebands around the austenite (200) peak as shown in Figures 5 (b) and (c). Thus, it can be concluded that after 10 hrs of aging at 530° C, the 0.043% P steel is in a later stage of spinodal decomposition than the low phosphorus, 0.006% P steel.

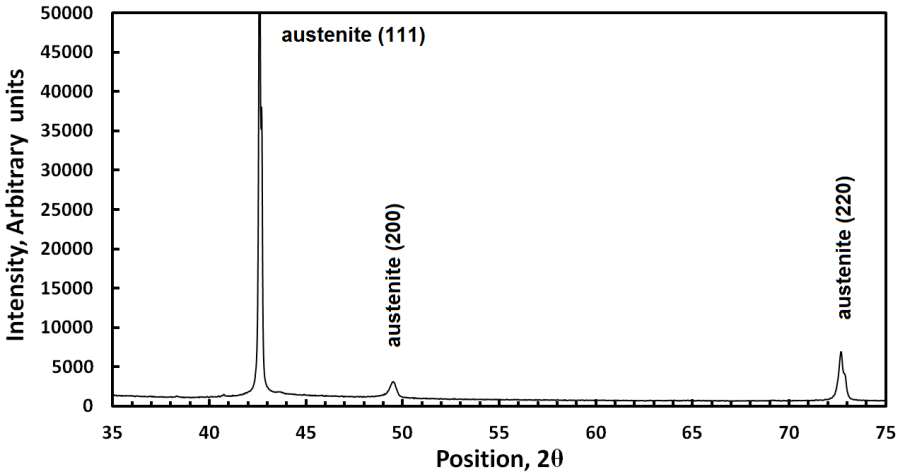

Fig. 4 The X-Ray diffraction pattern of the as-solution treated and quenched 0.043% P specimen shows no evidence of decomposition and only fundamental austenite diffraction peaks are observed.

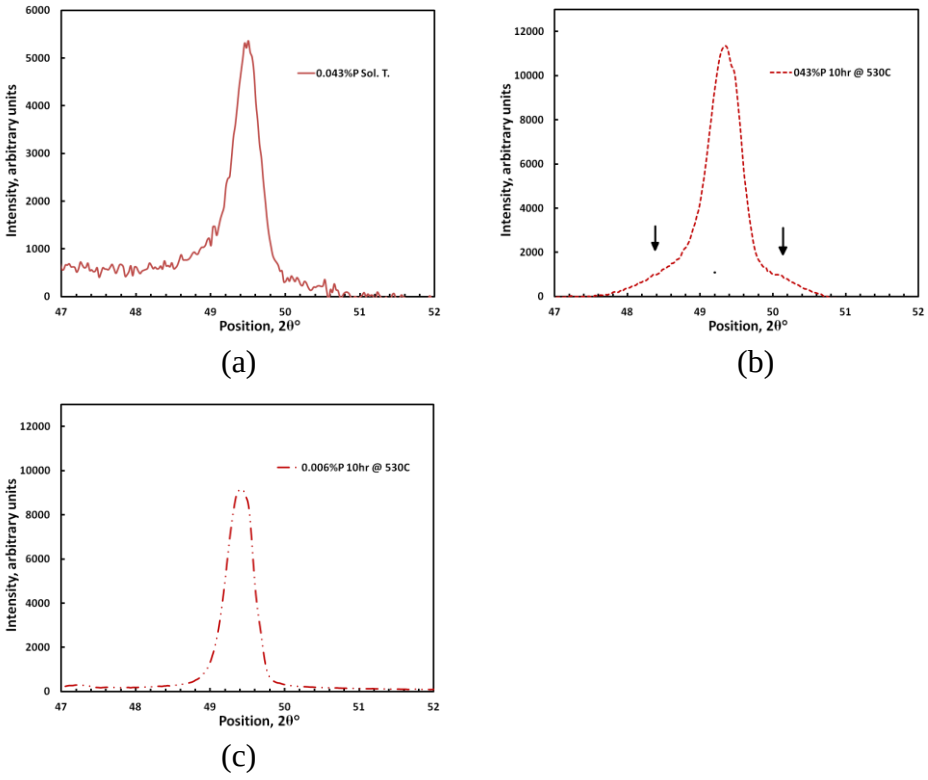

Fig. 5 The detail image of the (200) austenite Bragg peaks are shown for the (a) as solution treated 0.043%P specimen and (b and c) the 0.006%P and 0.043% P specimens that were aged for 10 hrs at 530°C. (a) Sidebands were not observed in the solution treated condition. (b) After 10hrs at 530°C, sidebands are beginning to form only in the 0.043% P specimen as denoted by the arrows.

LEAP experiments were performed to determine the effect of phosphorus on the size, distribution, and chemical composition of κ-carbide. Specimens from the 0.006% P and 0.043% P steels plate were aged for 10 hours at 530°C. IVAS 3.6 software was used to create an atom-by-atom reconstruction of each specimen. A virtual, rectangular, "slice" of the total reconstruction volume was used for analysis. The κ-carbides were discriminated from the matrix austenite by a 4 at.% C isoconcentration surface obtained with a voxel size of 1 nm and a delocalization of 3 nm to be consistant with previous analysis of low phosphorus material (< 0.003% P) of the same nominal chemistry but with different silicon contents.[21] Figures 6 (a) and 6 (b) show the reconstruction slices of the 0.006% P and 0.043% P specimens, respectively, that were aged for 10 hours at 530°C. Carbon modulation in the 10 hour aged 0.006% P specimen was not apparent in the reconstruction and the carbon concentration appears homogenous as shown in Figure 6 (a). Thus, κ-carbide could not be distinguished from the austenite matrix in the low phosphorus specimen as shown in Figure 6 (a). The reconstructed slice of the 10 hour aged 0.043%P specimen is shown in Figure 6 (b). κ-carbide is distinguished from the matrix by the 4 at.%C isoconcentration surface which is shown oriented in a nearly cube direction (see Figure 6 (b)). After 10 hours of aging at 530°C, the κ-carbide in the 0.043% P reconstruction appears not as discrete particles but as interconnected regions aligned in cube directions. The volume fraction of κ-carbide in Figure 6 (b) was determined to be 0.32 by summing the total number of atoms contained within the isoconcentration surfaces vs. the total number of matrix austenite atoms in the reconstruction and then determining the volume of each phase. Lattice parameters of 0.373 nm for κ-carbide and 0.367 nm for austenite were measured from x-ray diffraction

patterns and used to calculate molar volumes. The interconnectivity of the κ-carbide in the 0.043% P reconstruction made it difficult to determine the size of individual κ-carbides, however, the interparticle spacing, λ, along a cube direction was determined to be around 15 nm. It should be noted that APT artifacts can arise as a consequence of local magnification or demagnification effects and can lead to errors when measuring distances between interfaces.[31]

Evidence of clustering or short range ordering in the early stages of austenite decomposition can be determined from LEAP reconstructions utilizing a radial distribution function, RDF, that determines the number of nearest neighbor atoms as a function of distance from center atom positions. The RDF is a representative of the average radial concentration profile as a function of distance away from each detected atom of a chosen element. In the current study carbon will be used as the center atom. The RDF indicates the probability of finding an element *i* a distance *r* from each detected carbon atom. Radial distribution functions were calculated using a step size of 0.1 nm and the measured concentration at each position was normalized with respect to the bulk concentration. The RDF is expressed as follows:

$$RDF(r) = \frac{C_i(r)}{C_0} = [N_i(r)/N(r)]/C_0 \qquad (1)$$

Where $C_i(r)$ is the atomic concentration of element *i* at a distance *r* from center carbon atoms. C_0 is the average concentration of element *i* in the entire analyzed volume. RDF can also be expressed in terms of the total number of atoms of element *i* at a distance *r*, $N_i(r)$, and the total number of atoms of all types, N(r). RDFs of iron, aluminum, carbon,

and silicon content with respect to distance from center carbon atoms are shown in Figure 7 (a) and (b) for the 0.006% P and 0.043% P specimens, respectively, that were aged for 10 hours at 530°C. A value of the normalized composition greater than one indicates SRO or clustering and a value less than one means that the atoms repel each other in solution. Figure 7 (a) shows a tendency towards short range ordering or clustering of carbon on a scale of less than 2 nm in the 0.006% P specimen with a peak normalized carbon concentration of 1.02. In comparison, the 0.043% P specimen shows much greater carbon clustering with a peak normalized carbon concentration of 1.10 and higher than average carbon concentration on a scale up to 8 nm as shown in Figure 7 (b).

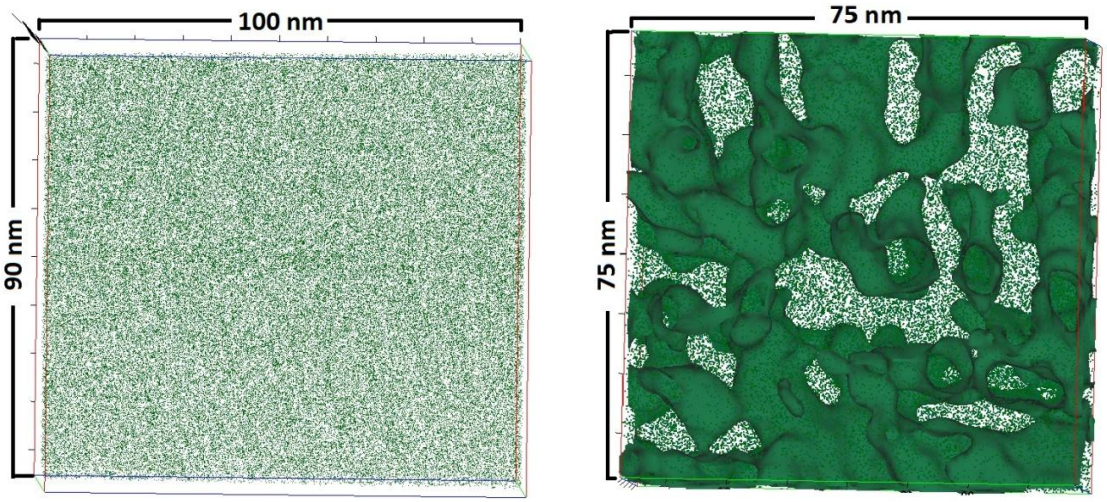

(a) (b)

Fig. 6 Rectangular virtual slices of the total reconstruction volume corresponding to the (a) 0.006%P steel and the (b) 0.043% P steel that were aged for 10 hours at 530°C showing 50% of the total carbon atoms (green dots). (a) Compositional modulation of carbon is not apparent in the 0.006% P specimen. (b) The 4at.% C isoconcentration surfaces in the 0.043% P specimen show the high connectivity of the modulated structure of the κ-carbide. Slice depth in both reconstructions is 25 nm.

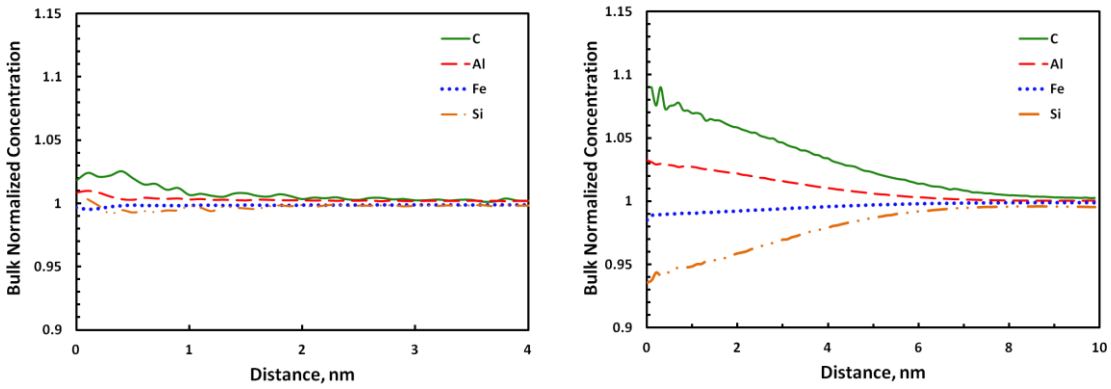

Fig. 7 Radial distribution functions showing the bulk normalized concentration of C, Al, Fe, and Si as a function of distance from center carbon atoms for the (a) 0.006% P and (b) 0.043% P specimens that were aged for 10 hrs at 530° C. (a) There is a tendency towards clustering of carbon atoms on a scale less than 2 nm in the low phoshphorus specimen. (b) The high phosphorus specimen shows a higher amplitude carbon and aluminum clustering at a much greater distance of up to 8 nm. Silicon is shown to partition far away from carbon.

Aluminum is also shown to cluster with carbon in the 0.043% P specimen, however, at a much smaller normalized concentration amplitude of 1.03, indicating only diffusion of aluminum in the short range is required for precipitation of κ-carbide. Silicon is shown to be anti-correlated with carbon and prefers to be far away from carbon atoms (Figure 7 (b)). Iron, manganese, molybdenum, and phosphorus atoms were randomly distributed with respect to carbon in both specimens.

The evolution of the microstructure during aging can also be represented using a 2-D concentration contour plot representing a "thin slice" of the reconstruction. 2-D concentration maps of the 0.006% P and 0.043% P 10 hr aged specimens were generated using the IVAS 3.6 software utilizing a voxel (cube) size of 1 nm^3. Concentration contour plots corresponding to carbon and aluminum are shown in Figure 8 for the (a and b) 0.006% P and (c and d) 0.043% P specimens. In the 0.006% P specimen, the carbon

concentration varied between 2.4 and 4.4 at.% with a mean value of 3.3 at.% as shown in Figure 8 (a). The aluminum concentration in the 0.006% P specimen varied from 16 to 19 at.% with an average value of 17 at.% as shown in Figure 8 (b). Aluminum is not always modulated with carbon as shown in Figure 8 (a and b). At an equivalent aging time of 10 hrs at 530° C, the peak concentration of carbon is much greater in the 0.043% P specimen and carbon ranges from a concentration of 2.1 at.% to 6.0 at.% with a mean value of 3.8 at.% C as shown in Figure 8 (c). The aluminum concentration in the 0.043% P specimen ranged from a minumium of 15 at.% to a maximum of 21 at.% Al with an average composition of 17 to 18 at.% Al as shown in Figure 8 (d). Regions of intense carbon and aluminum concentration are not only smaller in amplitude in the 0.006% P specimen, but they are also smaller in extent when compared to the regions of heavy carbon and aluminum in the 0.043% P specimen. Both specimens show a very diffuse interface between areas of high and low carbon concentration and this is an indication of a spinodal decomposition. The lower concentration amplitude and smaller wavelength of modulation in the low phosphorus alloy is evidence that the kinetics of spinodal decomposition is slower when compared with the high phosphorus specimen.

Solute distribution across an interface can be determined using a proximity histogram as a function of distance from an isoconcentration surface. The proximity histogram or proxigram was developed by Hellman et al.[32] and has the advantage in that it can accommodate the curvature of interfaces. An isoconcentration surface is constructed to define the second phase region and then the shortest distance from each atom to the nearest surface is determined. The composition of each atom is identified and

binned according to positive and negative distance from the interface. The concentration can then be plotted as a function of distance from the interface.

Proxigrams of the solute distribution as a function of distance from the 4 at.% isoconcentration surface in the 10 hr aged 0.043% P specimen are shown in Figure 9. Figure 9 (a) shows that the κ-carbide is slightly depleted in iron and manganese and enriched with as much as 21 at.% aluminum. The carbon amplitude reaches an average concentration of 6 at.% in the κ-carbide as shown in Figure 9 (b). Silicon is shown to partition to the matrix during aging. One of the most important results from the atom probe analysis is that phosphorus was found to be randomly distributed between the matrix and the κ-carbide as shown in Figure 9 (c). Thus the increase in the rate of hardening with increasing phosphorus content is not related to long range diffusion of phosphorus.

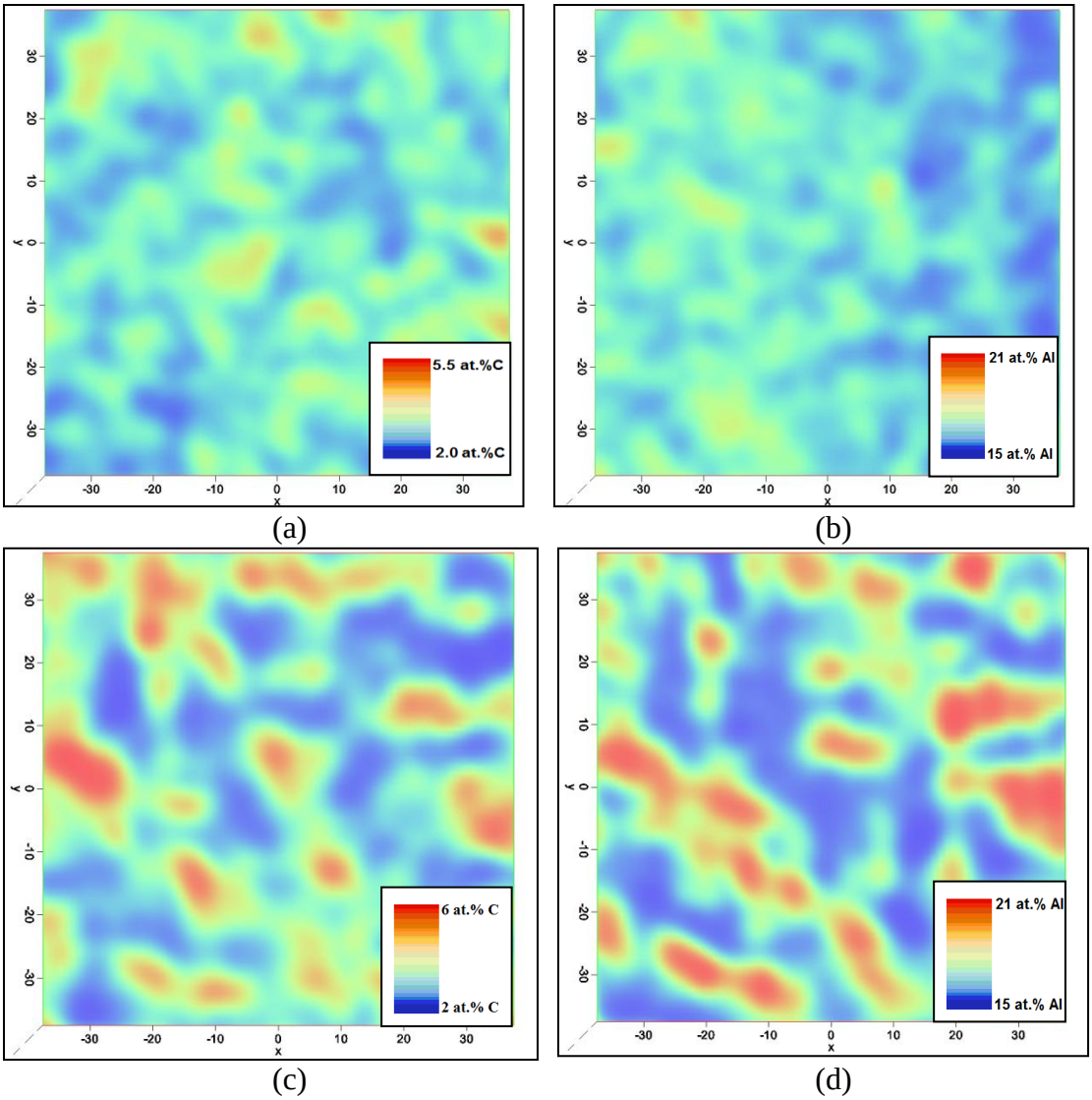

Fig. 8 2-D concentration surfaces for carbon (a and c) and aluminum (b and d) as shown for the 0.006% P (a and b) and 0.043% P (c and d) specimens that were aged for 10 hrs at 530° C. Diffuse interfaces and a growing carbon amplitude are indications of spinodal decomposition. The carbon and aluminum peak concentrations are greater in the 0.043% P specimen as well as the spacing between aluminum and carbon segregated zones.

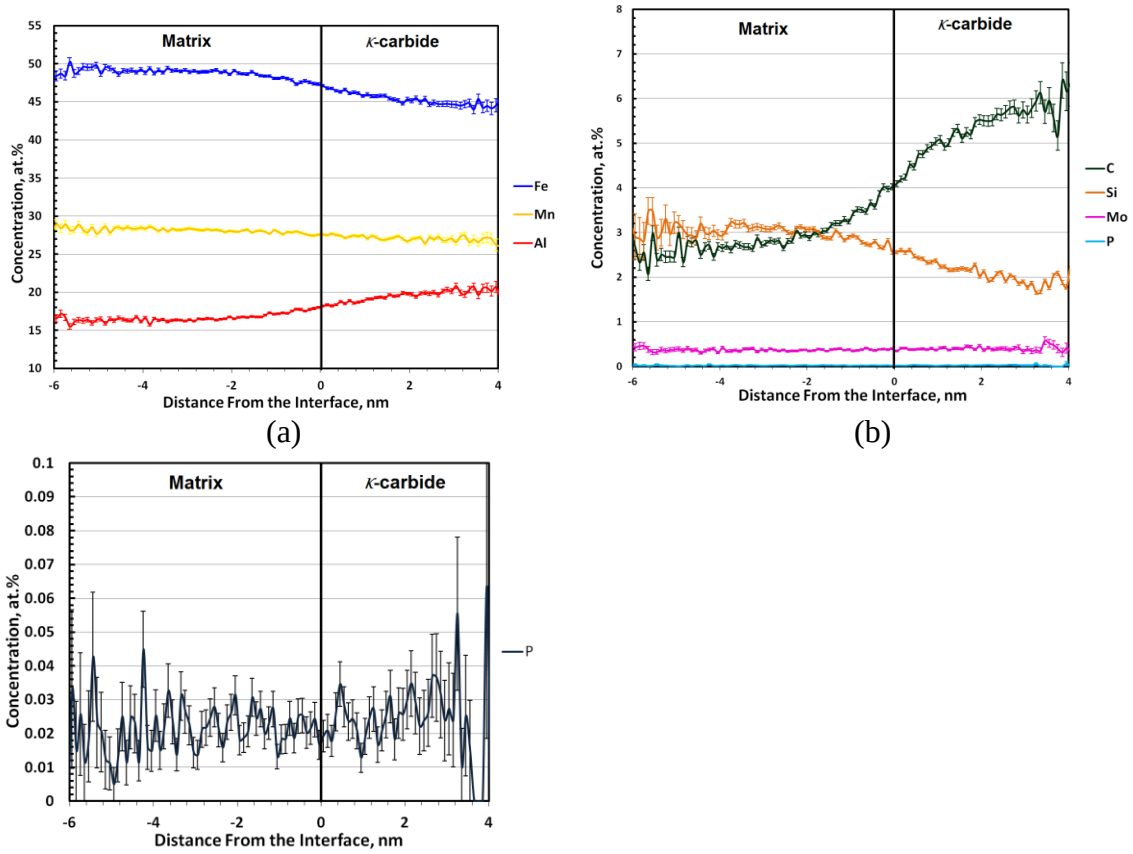

Fig. 9 Concentration profiles across the interface of the κ-carbide and austenite matrix for Fe, Mn, Al, C, Si, Mo, and P for the aged for 10 hrs at 530° C. (a) The κ-carbide is slightly depleted in Fe and Mn but enriched wth as much as 21 at.% Al. (b) The amplitude of the carbon concentration in the κ-carbide to be around 6 at.%. Silicon strongly partitions to the matrix during aging. (c) Phosphorus is randomly distributed across interface with an average concentration of 0.02 at.%.

IV. DISCUSSION

In many metallic systems the mechanism for precipitation of ordered phases from solid solution is not well understood because of the competing processes of phase separation (clustering) and ordering. As a result, there are a number of routes by which a supersaturated solid solution Fe-Mn-Al-C alloys may decompose into a two phase mixture of ordered κ-carbide and disordered solid solution austenite. Most researchers

consider that the first stage of decomposition in Fe-Mn-Al-C alloys is accomplished via spinodal decomposition of the initially disordered matrix into carbon rich[6,12-14]or carbon and aluminum rich[8,10,11,15] and poor zones followed by ordering of those zones into the κ-carbide structure. It is also possible κ-carbide may form as a result of nucleation and growth of ordered domains followed by various stages of coarsening.[20] A third method involves spinodal decomposition occurring subsequent to or concurrent with first stage continuous ordering as presented by Soffa and Laughlin.[33] Both spinodal decomposition and ordering mechanisms proceed at a high rate and it is difficult to determine the decomposition sequence when both occur. Ordering is evidenced by the presence of superlattice reflections in electron diffraction patterns while spinodal decomposition produces satellite reflections around matrix diffraction spots.[34-37] In the current study, the high phosphorus (0.043% P) specimen exhibited evidence of short range ordering corresponding to the κ-carbide structure in the as-quenched state as shown by $E2_1$ superlattice reflections in Figure 2 (b). Satellite reflections were not observed around the fundamental austenite electron diffraction intensities in the as-quenched 0.043% P steel. It should be noted that at a concentration of 0.043 wt.% P that the alloy is supersaturated with respect to phosphorus and phosphides are present in the microstructure.[22] It has been estimated that the maximum solubility of phosphorus at the solution treatment temperature is 0.018 wt.%. Thus short range ordering of Fe-Al-C into the $E2_1$ κ-carbide structure occurs prior to any other decomposition sequence when phosphorus is as a great as 0.018% . First principles calculations show that SRO of Fe-Al-C into the $E2_1$ crystal structure in as-solution treated Fe-Mn-Al-C is energetically favorable over a homogeneous solid solution.[38]

Short range ordering prior to spinodal decomposition has been reported previously by Acselrad et al.[15] for an as-quenched Fe-28Mn-8.5Al-1C-1.25Si steel. They report 2-3 nm ordered "zones" that were responsible for the absence of an incubation time during spinodal decomposition.[15] Acselrad and co-workers did not report the phosphorus content of their steels.[15] In comparison, the as-quenched low phosphorus (0.006% P) specimen in Figure 2 (a) revealed no evidence of superlattice reflections or satellite intensity near the fundamental reflections in electron diffraction patterns, indicating only disordered solid solution austenite. This is evidence that phosphorus greatly increases the prevalence of the ordering reaction and this is why high phosphorus alloys are observed to have a much higher first stage age-hardening rate as shown in Figure 1 (b).

First principles calculations show that phosphorus substitutions for aluminum corner positions in κ-carbide are most energetically favorable and this may be responsible for the enhancement of the ordering reaction in the high phosphorus alloys.[23]

A random walk estimate of the short range ordering kinetics of phosphorus atoms and aluminum atoms into κ-carbide corner positions during quenching was calculated. Although the actual quench rate was not determined in the current study, a quench rate of 340°C/s was determined for 10x10x55mm rectangular bars from the work of Howell[22] for the same nominal composition alloy that was quenched from 1050° C to room temperature in agitated water. Acelrad et al. estimated the upper limit of homogeneous precipitation of κ-carbide to be 650°C.[15] Therefore a quench rate of 340°C/s yields a time of 0.29s per 100°C of quench interval for a total time of 1.2s above 650°C. The diffusivity of phosphorus and aluminum in austenite at 650°C was determined to be $7.15 \times 10^{-13} cm^2/s$ and $2.51 \times 10^{-14} cm^2/s$, respectively, using reference values from reported

diffusion data.[39,40] For cubic metals the diffusivity is related to the jump frequency, Γ, and the jump distance, α, by the following relationship.

$$D = \frac{1}{6}\Gamma\alpha^2 \qquad (2)$$

Considering jumps between adjacent planes, this results in a total of $7.5x10^3$ atomic jumps of phosphorus and $4.2x10^2$ atomic jumps of aluminum, an order of magnitude less, during the quench. Thus, short range ordering of phosphorus into $E2_1$ corner positions of the κ-carbide structure may be an order of magnitude faster than that of aluminum. It should be noted that thermodynamic preference of phosphorus substitution for aluminum corner positions was not taken into account in the above calculation.

The brightfield image in Figure 3 (a) and [001] zone diffraction pattern shows strain modulation along cube directions. The presence of <100> aligned satellites flanking high order austenite diffraction spots in Figure 3 (a) is evidence that the strain modulation along cube directions and the corresponding brightfield image is consistent with spinodal decomposition as reported previously for Fe-Mn-Al-C alloys[15,16,18] as well as many other systems.[35,37,41] The 0.043% P specimen in Figures 3 (c) and 3 (d) shows that the κ-carbide is adapting a cuboidal morphology and coarsening along cube directions with satellite reflections that are much closer to fundamental reflections than in the low phosphorus specimen in Figure 3 (a). These satellite reflections will move closer to the fundamental matrix reflection as decomposition progresses and the wavelength of the modulation grows.[35,37,41] A comparison of the positions of the satellite reflections in Figure 3 (a) and Figure 3 (c) provide evidence that the high phosphorus specimen is in a much later stage of spinodal decomposition.

Sidebands around fundamental x-ray diffraction peaks are equivalent to the satellite reflections observed in electron diffraction patterns. Daniel and Lipson demonstrated that sidebands around Bragg peaks of an aged Cu-Ni-Fe alloy were the result of periodic composition modulation along <100> directions.[42] Sidebands around fundamental diffraction peaks have been used as evidence for spinodal decomposition in a variety of different systems including Ag-Cu-Au alloys,[43,44] Cu-Ni-Sn alloys,[45] Cu-Ti alloys,[46] and by Sato et al.[8] in their study of a Fe-30Mn-9Al-0.9C-0.016P steel aged at 550°C. Sidebands can be detected in Fe-Mn-Al-C alloys only after there is a sufficient difference in the lattice parameter between the C and Al rich and poor zones.[8,12] Diffraction patterns of the 10 hr aged specimens showed sidebands around austenite peaks only in the 10 hr aged condition and only for the 0.043% P steel as shown in Figures 4 and 5. Thus, from analysis of electron micrographs and XRD profiles, it is most likely that spinodal decomposition follows short range ordering of Fe-Al-C into clusters which have the same coordination as in the $E2_1$ κ-carbide structure. The faster diffusivity of phosphorus appears to accelerate the ordering and subsequent spinodal decomposition.

The precipitate interface during spinodal decomposition will generally be diffuse compared with interfaces formed by nucleation and growth mechanisms.[47,48] In most cubic alloys, Young's modulus will be a minimum in <100> directions and this gives rise to a periodic and modulated structure along <100> that is frequently observed.[35,41,49-51] However, a <100> periodic arrangement of precipitates is not always the result of spinodal decomposition. Ardell and Nicholson[52] determined that the <100> arrangement of cube-shaped precipitates in a Ni-13.5at.%Al alloy was the result of classical nucleation

and growth with selective coarsening along cube directions resulting from elastic modulus differences between the matrix and precipitate phase. Likewise, it has been suggested by some that hardening in Fe-Mn-Al-C alloys is simply the result of first stage ordering followed by particle coarsening with alignment along <100> resulting from elastic interactions between the κ-carbide and the matrix.[20]

Direct evidence of precipitation via nucleation and growth or spinodal decomposition can be obtained utilizing atom probe microscopy. Hill and Ralph[53] utilized atom probe field-ion microscopy (APFIM) to determine that ordered γ' in a Ni-14at.%Al alloy formed as a result of growing composition modulations rich in aluminum that developed the stoichiometric Ni_3Al composition only after extended aging times. In contrast, the appearance of discrete stoichiometric Ni_3Al particles after a slower quench was determined to be via nucleation and growth.[53] In a APFIM study by Hono et al.[54] the stoichiometric δ' was observed in the as-quenched state of a Al-7.8 at.% Li alloy and thus concluded that decomposition had already taken place. More recently, LEAP has been used to evidence concurrent phase separation and clustering in duplex stainless steels.[55] In the current study, κ-carbide was shown to exist as an interconnected structure rich in carbon and aluminum as shown in Figures 6 (b) and 9 for the 0.043% P alloy that was aged for 10 hrs at 530° C. An interconnected structure is typical for the spinodally decomposing alloys and characterization of interconnected structures by LEAP has been utilized as evidence for spinodal decomposition in Fe-Co-Mo alloys.[56] The boundary between the κ-carbide and the matrix austenite is also shown to be very diffuse, spanning a distance of around 8 nm as shown in Figure 9. Although artifacts can arise because of field evaporation differences that lead to error in accurately measuring distances,

interfaces that form via nucleation and growth in γ/γ' alloys are much sharper and span only a distance of up to 2.5 nm.[57] As mentioned above, a growing concentration amplitude with aging time can only be accomplished by spinodal decomposition. 2-D concentration contour plots obtained from 3-D LEAP reconstructions have been utilized to prove the existence of spinodal decomposition in a variety of systems.[26,29,56] In Figure 10 the 2-D carbon concentration surface of the low phosphorus 0.006% P specimen that was aged for 10 hrs at 530° C is compared to the carbon concentration surface of a low phosphorus, 0.002% P, alloy with a similar nominal composition of Fe-30Mn-9Al-1.56Si-0.9C-0.5Mo that was aged for 60 hrs at 530° C.[21]

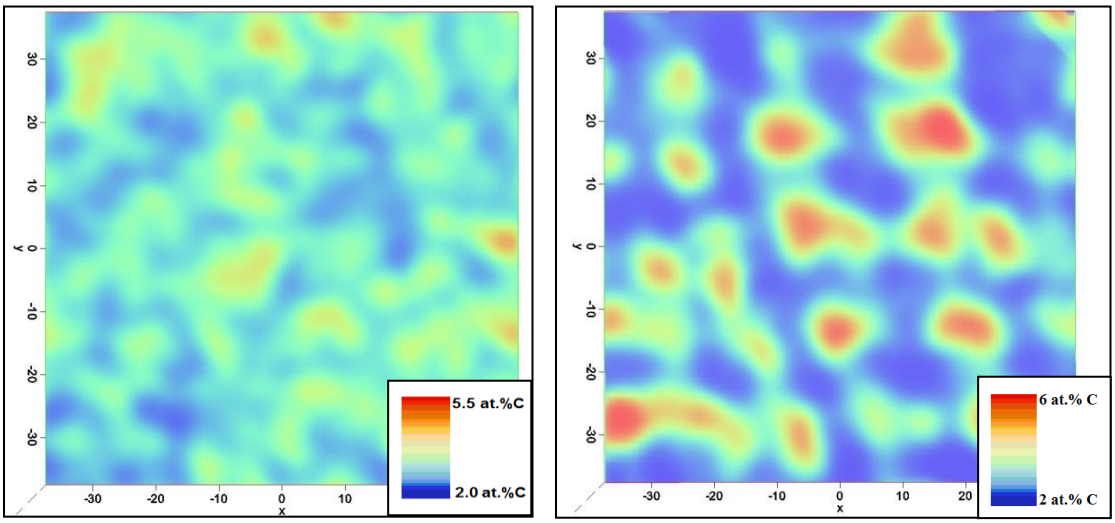

(a) (b)

Fig. 10 Carbon concentration contour plots corresponding to (a) the 10 hr aged 0.006% P (1% Si) alloy in the current study and (b) a previously reported[21] 0.002% P alloy of similar composition Fe-30Mn-9Al-1.56Si-0.9C-0.5Mo that was aged for 60 hrs at 530° C show a growing carbon amplitude with aging time.

For low phosphorus alloys, the carbon concentration amplitude is shown to increase from an average of 4 at.% to 6 at.% as the aging time is increased from 10 to 60 hrs, thus indicating spinodal decomposition. Increasing the amount of phosphorus greatly increased the spinodal decomposition rate as evidenced in Figure 8 by the much higher carbon amplitude in the 10 hr aged 0.043% P specimen. However, phosphorus was shown to be randomly distributed between the κ-carbide and the austenite matrix as shown in Figure 9 (c). Thus, long range diffusion of phosphorus is not involved. It is suggested that phosphorus increases the prevalence of the initial short range ordering reaction and this accelerates subsequent spinodal decomposition. Table 2 lists the matrix and κ-carbide compositions for the high and low phosphorus alloys that were aged for 10 hrs at 530° C in comparison to previously reported compositions for low phosphorus alloys (0.002% P) of the same nominal composition but with different silicon contents.[21] The matrix and κ-carbide compositions of the previously reported alloys with different silicon contents and the 0.043% P alloy were determined from the plateau region of proxigrams as shown in Figure 9. The κ-carbide could not be distinguished from the matrix of the 10 hr aged low phosphorus specimen utilizing the 4 at.% C isoconcentration surface as shown in Figure 6 (a). Instead, the average concentration of the peak and valley regions of 2-D concentration surfaces was used to determine the concentration amplitude and matrix compositions in the 10 hr aged 0.006% P specimen.

Table 2. Compositions of the austenite and κ-carbide in atomic percent as determined by LEAP for alloys with nominal bulk composition Fe-30Mn-9Al-XSi-0.9C-0.5Mo (wt.%).

0.006 wt.% P, 1.01 wt.% Si aged for 10 hours at 530° C					
Phase	**Fe**	**Mn**	**Al**	**C**	**Si**
austenite	48.8	30.0	16.4	2.7	3.0
k-carbide	46.2	27.5	18.3	4.0	2.4
0.043 wt.% P, 0.92 wt.% Si aged for 10 hours at 530° C					
Phase	**Fe**	**Mn**	**Al**	**C**	**Si**
austenite	49.1	28.4	16.4	2.5	3.1
k-carbide	44.6	26.8	20.2	5.9	1.9
0.002 wt.% P, 0.59 wt.% Si aged for 60 hours at 530° C[21]					
Phase	**Fe**	**Mn**	**Al**	**C**	**Si**
austenite	50.0	28.4	17.0	2.5	1.4
k-carbide	46.0	26.4	21.1	5.3	0.75
0.002 wt.% P, 1.56 wt.% Si aged for 60 hours at 530° C[21]					
Phase	**Fe**	**Mn**	**Al**	**C**	**Si**
austenite	49.1	28.1	16.2	2.3	3.9
k-carbide	42.3	26.3	21.1	6.6	2.6

It is shown that the carbon amplitude increases from 4 to between 5.3 and 6.6 at.% C (depending on the silicon content) when low phosphorus alloys are aged from 10 to 60 hrs at 530° C.[21] However, after only 10 hrs of aging, the high phosphorus, 0.043% P, specimen has a greater carbon amplitude than a previously reported low phosphorus (0.002% P) alloy containing Fe-30Mn-9Al-0.59Si-0.9C-0.5Mo alloy.[21]

Recent studies of silicon in low phosphorus, 0.002% P, Fe-30Mn-9Al-0.9C-0.5Mo alloys found that hardening was the result of an increase in the concentration amplitude of carbon during aging as proposed by Kato et al.[21,58] Figure 1 (b) shows the 530° C age hardening curves for the 0.006% P and 0.043% P steels. It is shown that after 10 hrs of aging, the 0.043% P alloy has attained similar a similar hardness as the peak aged 0.006% P specimen that was aged for 60 hrs. Thus, previously reported age hardening curves are in agreement with the current study.[24]

A theory of spinodal hardening presented by Kato et al.[58] considered the increase in strength during aging to be the result of coherency stress associated with the growth in the composition amplitude. The extent of hardening with evaluated using the concentration amplitude of carbon determined from the atom probe analysis according to the model by Kato et al. given below.[58]

$$\Delta\tau_Y = \frac{\varepsilon}{\frac{1}{6^{\frac{1}{2}}}} (C_{11} - C_{12}) \quad (1)$$

$$\varepsilon = \frac{A\eta(C_{11}+2C_{12})}{3C_{11}} \quad (2)$$

Where $\Delta\tau_y$ is the increase in the shear stress, ε is the strain amplitude, and *A* is the concentration amplitude of carbon which was measured to be 5.9 and 4.0 at.% for the 0.043% P and 0.006% P specimens that were aged for 10 hrs at 530° C. C_{11} and C_{12} are elastic coefficients of the matrix and were taken to be 14.4×10^{10} and 8.7×10^{10} N/m^2 which were used by Sato et al.[8] to accurately model increases in the yield strength during aging of a Fe-29.5Mn-9.2Al-0.94C steel. It should be noted however that these values were taken from the work of Salama and Alers and were determined for a single crystal of Fe-30Ni .[59] The parameter η is the change in the austenite lattice parameter as a function of increasing carbon concentration and $\eta = da/dC \cdot 1/a$. The change in the austenite lattice parameter with increasing carbon content was estimated by Sato et al.[8] to be 0.18 for a similar composition Fe-30Mn-9Al-0.9C-0.03Si (0.016% P) alloy using the data of Charles et al.[60]

Multiplying $\Delta\tau_y$ by an appropriate Taylor factor of 3.06 gives the change in the yield stress due to spinodal hardening. The increase in yield strength after aging for 10 hrs at 530° C was predicted to be 370 and 550 MPa for the 0.006 and 0.043% P alloys, respectively. Howell et al. studied the tensile properties of a Fe-28.8Mn-8.3Al-0.9C-1Si-0.5Mo alloy with high phosphorus, 0.06% P. After age hardening for 10 hrs at 530° C, they reported a 433 MPa increase in the yield strength, from 458 MPa in the solution treated condition to 891 MPa after aging.[2] It should be noted that for Fe-30Mn-9Al-0.9C alloys, compositions of about 0.02 wt.% P and above exceed the solubility limit of phosphorus in these steels and as such, hardening resulting from solid solution phosphorus would be expected to be comparable between phosphorus levels of 0.043 and 0.06% P. Thus, the theoretical increase in strength of 550 MPa for the 0.043% P alloy in the current study can be compared with a 433 MPa increase in strength as observed by Howell et al. for a 0.06% P steel for the same aged condition.[2] Although the hardening model overestimates the increase in yield strength by about 120 MPa, theoretical results fit experimental results reasonably well.

V. SUMMARY

Atom probe tomography, transmission electron microscopy, and X-Ray diffraction were used to determine the effect of phosphorus on the precipitation and composition of κ-carbide during aging. In the alloy containing 0.043 wt.% P the precipitation of κ-carbide was determined to form first by ordering of Fe-Al-C into the $E2_1$ structure and this was followed by spinodal decomposition involving mainly the diffusion of carbon along austenite <100>. Phosphorus was shown to increase the prevalence of the ordering reaction and high phosphorus, 0.043% P, specimens showed

short range ordering that took place during the quench. In contrast, neither short range ordering nor spinodal decomposition took place during the quench in the low phosphorus specimens, 0.006% P. High phosphorus specimens showed a higher increase in the concentration amplitude of carbon during aging when compared with low phosphorus specimens of equivalent composition and this was determined to be the mechanism behind the increase in the increased hardening rate with increasing phosphorus. However, long range diffusion of phosphorus was not involved in the observed increase in the hardening rate and the phosphorus distribution was random. It is therefore suggested that phosphorus increases the initial ordering reaction and that this greatly accelerates the later stage of spinodal decomposition.

ACKNOWLEDGMENTS

This work was supported in part by Army Research Laboratory under contracts from Battelle Memorial Institute (contract W911NF-07-D-0001) and Benet Laboratories (contract W15QKN-07-2-0004) and a grant from Northwestern University Center for Atom Probe Tomography. Laura Bartlett was also supported by a U.S. Department of Education GAANN fellowship under contract P200A0900048. The FEI Tecnai F20 scanning/transmission electron microscope was obtained with a Major Research Instrumentation grant from NSF under contract DMR-0922851. The authors also gratefully acknowledge Waukesha Foundry, Inc. for providing the low phosphorous Fe-Mn-Al-C alloys and the alloys with varying Si content.

REFERENCES

1. G. Frommeyer and U. Brux, 2006, Steel Research Int., Vol. 77, pp. 627-633.
2. R. Howell, T. Weerasooriya, and D. Van Aken, Tensile, 2008, AFS Trans.
3. L. Bartlett, A. Dash, D. Van Aken, V. Richards, and K. Peaslee, 2012, AFS Trans, 120, pp. 469-486.
4. G. Kayak, 1969, Met. Sc. And Heat Tr., Vol. 11, pp. 95-97.
5. G.S. Brady, H.R. Clauser, 1977, Materials Handbook, 11th Ed., p. 497.
6. O. Acelrad, L.C. Pereira, M.R. Amaral, 1992, Proceedings of Proc. And Prop. Of Mats., pp. 829-834.
7. L. Bartlett, A. Schulte, D. Van Aken, K. Peaslee, and R. Howell, 2010, MS&T Conf. Proceed., Houston, Texas Oct. 17-21(2010).
8. K. Sato, K. Tagawa, and Y. Inoue, 1990, Met. Trans A, vol. 21A, pp 5-11.
9. G.E. Hale and A.J. Baker, 1986, Conf. on Alt. Alloying for Env. Res. New Orleans, LA.
10. O. Acselrad, I.S. Kalashnikov, E.M. Silva, R.A. Simao, C.A. Achete, L.C. Pereira, 2002, Met. Trans. A , Vol. 33A, pp. 3569-3572.
11. I.S. Kalashnikov, O. Acselrad A. Shalkevich, Chumakova, and L.C. Pereira, 2003, vol. 136 pp. 72-79.
12. K. Sato, Y. Igarashi, Y. Inoue, T. Yamazaki, and M. Yamanaka, 1991, Proceed. of the Inter. Conf. on Stain. Steels, pp. 503-509.
13. W. Choo, J.H. Kim, 1997, Conf. on Thermo-mechanical Process. of Steels and Other Mats., pp. 1631-1637.
14. K.H. Han, J.C. Yoon, and W.K. Choo, Scripta Metallurgica, vol 20, pp. 33-36.
15. O. Acselrad, I.S. Kalashnikov, E.M. Silva, M.S. Khadyev, and R.A. Simao, 2006, Metal Science and Heat Treatment Vol. 48, pp. 543-553.
16. K. Sato, K. Tagawa, and Inoue, 1989, Mat. Sci. and Eng. A vol.111 pp. 45-50.
17. K.H. Han, W.K. Choo, D.Y. Choi, S.P. Hong, 1987, TMS-AIME, pp. 91-106.
18. W. Choo, J. Kim, and J. Yoon, 1997, Acta Mater. Vol. 45, pp. 4877-4885.
19. S. Karakishev and I. Kalashnikov, 1986, Phys. Met. Metall. Vol. 62, pp. 187-190.

20. A. Prodhan, and K. Chakrabarti, 1990, Journal of Mat. Sci. vol.25 pp. 1856-1862.

21. L.N. Bartlett, D.C. Van Aken, D. Ishiem, K. Song, and J. Medvedeva, 2013, to be submitted to Met. Trans. A.

22. R.A. Howell, 2009, "Microstructural Influence on Dynamic Behavior of Age Hardenable FeMnAl Steel Alloys" PhD Dissertation.

23. N.I. Medvedeva, R.A. Howell, D.C. Van Aken, and J.E. Medvedeva, 2010, Phys. Rev. B. vol. 81, p. 012105.

24. L. Bartlett, R. Howell, D. Van Aken, and K. Peaslee, 2010, AFS Trans. vol. 118, pp. 413- 423.

25. M.K. Miller, 2009, Mat.Char. vol. 60 pp. 461-469.

26. L. Johnson, M. Thuvander, K. Stiller, M. Oden, and L. Hultman, 2012, Thin Solid Films vol. 520, pp. 4362-4368.

27. W. Xiong J. Agren, and J. Zhou, 2012, Cond. Matter and Mat. Science.

28. D. Saxey, M. Apperley, R. Zheng, T. Honma, and S. Ringer, 2006, Materials Forum vol. 30 pp. 85-89.

29. W. Xiong, P. Hedstrom, M. Selleby, J. Odqvist, M. Thuvander, and Q. Chen, 2011, CALPHAD: Comp. Coup.of Phase Dia. and Thermochem.vol. 35, pp. 355-366.

30. J. Seol, D. Raabe, P. Choi, H. Park, J. Kwak, and C. Park, 2012, Submitted to Scripta Mater., (2012).

31. M. Mulholland, and D. Seidman, 2011, Microsc. Microanal. vol.17 p. 950.

32. O.C. Hellman, J.A. Vanderbroucke, J. Rusing, D. Isheim, and D.N. Seidman, 2000, Microsc. Microanal. vol. 6, pp. 437-444.

33. W. Soffa and Laughlin, 1989, Acta Metall. Vol. 37 pp. 3019-3028.

34. G. Viswanathan, R. Banerjee, A. Singh, S. Nag, J. Tiley, and H. Fraser, 2011, Scripta Materialia Vol. 65, pp. 485-488.

35. J. Zhao, and M. Notis, 1998, Acta Mater. Vol. 4, No.12, pp. 4203-4218.

36. C. Corey, B. Rosenblum, and G. Greene, 1973, Acta Metallurgica Vol. 21, pp. 837-844 .

37. I. Bartra, G. Dey, U. Kulkarni, and S. Banerjee, 2003, Mat.s Sci.and Eng. A vol. 360 pp. 220-227.

38. N.I. Medvedeva, M.S. Park, D.C. Van Aken, and J.E. Medvedeva, 2012, Cond. Mat. Mat. Sci. arXiv:1208.0310v1.

39. C.J. Smithells, 1962, Metal. Reference Book, Butterworth's, London, p. 593.

40. C.J. Smithells, 2004, Metal. Reference Book, Butterworth's, London, p. 13-21.

41. D. Laughlin, R. Sinclair, and L. Tanner, 1980, Scripta Metall. vol. 14, pp. 373-376.

42. V. Daniel and H. Lipson, Proc. R. Soc. vol. 18A pp. 368.

43. J. Udoh, H. Fujiyama, K. Hisatsune, M. Hasaka, and K. Yasuda, 1992, Journal of Mat. Sci.,vol. 27 pp. 504-510.

44. K. Hisatsune and K. Udoh, 1991, Journal of Alloys and Compounds, vol. 176 pp. 269-283.

45. V. Lopez, A. Arias-Perez, L. Saucedo-Munoz, Journal of Mat. Sci. Lett. vol. 18 pp. 1697-1699.

46. F. Hernandez-Santiago, N. Cayetano-Castro, M. Lopez-Hirata, Dorantes-Rosales and J. Cruz-Rivera, 2004, Mat. Trans.vol. 45 pp. 2312-2315.

47. Porter and Easterling, 1992, "Phase transformations in metals and alloys," 2nd addition CRC Press, pp.308-311.

48. J.W. Cahn, 1968, Met. Trans. A. vol. 242 pp.177.

49. D.E. Laughlin and J.W. Cahn, 1975, Acta Metall., vol. 23 pp. 329-339.

50. FuXing Y., Ohsawa Y., Sato A., and Kawahara K., "Phase Decomposition of the gamma phase in a Mn-30at.% Cu alloy during aging," Acta Mater. Vol. 48 pp. 1273-1282 (2000).

51. J. Singh, C. Wayman, J. Mazumder, S. Lele, and S. Ranganathan, Met. Trans. A, vol. 19 pp 1703-1709.

52. A. Ardell and Nicholson, 1966, Acta Met. vol 14, p.1295.

53. S. Hill and B. Ralph, 1992, Acta Metall. vol. 30 pp. 2219-2225.

54. K. Hono, S. Babu, K. Hiraga, R. Okano, and T. Sakurai, 1992, Acta Metall. Mater. vol. 40, pp. 3027-3034.

55. J. Zhou, J. Odqvist, M. Thuvander, S. Hertzman, and P. Hedstrom, 2012, Acta Mater. vol. 60, PP. 5818-5827.

56. E. Eidenberger, M. Schober, P. Staron, D. Caliskanoglu, H. Leitner, and H. Clemens, 2010, Intermetallics, vol. 18 pp. 2128-2135.

57. J. Hwang, S. Nag, A. Singh, R. Srinivasan, J. Tiley, H. Fraser, and R. Banerjee, 2009, Scripta Mater. vol. 61. pp. 92-95.

58. M. Kato, T. Mori, and L. Schwartz, 1980, Acta Metall.vol. 28. Pp. 285-290.

59. K. Salama, and G. Alers, 1968, Journal of App. Phys., vol. 39, pp. 4857-4859.

60. J. Charles, A. Berghezan, and A. Lutts, 1984, J. Phys., Colloq., vol. 45, pp. C1-619-623.

PAPER

4. Effect of Aluminum and Carbon on the Dynamic Fracture Toughness of Fe-Mn-Al-C Steels

L.N. Bartlett and D.C. Van Aken

Missouri University of Science and Technology

Department of Materials Science and Engineering

Army Research Lab

Rolla, MO 65409

Tel.: 573-341-4717

E-mail: dcva@mst.edu

Key Words: Fe-Mn-Al-C, lightweight steel, Aluminum, Carbon, Dynamic Fracture Toughness

Submitted to Transactions of the American Foundry Society (2013).

ABSTRACT

Dynamic fracture toughness was evaluated as a function of aluminum and carbon content in laboratory cast Fe-28%Mn-(2.9-9)%Al-0.9%Si-(0.9-1.8)%C-0.6%Mo steels. Both the solution treated and aged castings showed an increase in toughness with decreasing aluminum content. In the solution treated condition, decreasing the aluminum content from 6.5% to 2.9% resulted in an 85 kJ/m^2 increase in toughness at a constant carbon content of 0.9%. Increasing carbon from 0.9% to 1.2% in solution treated 2.9%Al steels resulted in a 125 kJ/m^2 increase in toughness from 605 to 730 kJ/m^2. As the amount of aluminum was reduced from 9 to 6.5% Al, toughness increased from 160 to 370 kJ/m^2 in castings aged to approximately 300 BHN. Carbon additions greater than 1.2% reduced the toughness of aged castings and produced brittle fracture, which was associated with increased κ-carbide precipitation. Laboratory heats contained up to four times the amount of AlN than an commercially cast steel of similar composition and the high AlN content decreased the dynamic fracture toughness by 200 kJ/m^2. It is anticipated that with a clean melt practice and limiting the aluminum content in aged castings to 6.5%, while simultaneously keeping C below 1.2%, will produce up to a 200 kJ/m^2 increase in toughness when compared with a Fe-30%Mn-9%Al-1%Si-0.9%C-0.5%Mo steel.

INTRODUCTION

Recent research has focused around lightweight austenitic Fe-Mn-Al-C steels for use in structural and high energy absorbing applications. Additions of 4-12wt.% aluminum reduce the density by up to 18% when compared with quench and tempered (Q&T) steels without a sacrifice in strength and toughness.[1,2] Fully austenitic

compositions typically contain from 20-30 wt.%Mn and greater than 0.7 wt%C.[2,3] All compositions in the following text are expressed as weight percent unless otherwise specified as a stoichiometric formula and then the composition is in an atomic proportion. The combination of low density with high strength and high work hardening behavior at elevated strain rates makes steels in the Fe-Mn-Al-C system very attractive for high energy absorbing applications.[1,2] Ultimate tensile strengths as high as 2000 MPa and Charpy V notch (CVN) breaking energies as high as 221 J at room temperature have been reported for solution treated wrought alloys.[4,5] Fe-Mn-Al-C steels that contain greater than 5% Al and greater than 0.3% C are age-hardenable when isothermally held in the temperature range of 400 to 700°C and strengthening is the result of homogeneous and coherent precipitation of nano-sized κ-carbide.[3,6-13] Depending on the composition and heat treatment, age-hardenable cast alloys have excellent toughness and high strengths. Most studies have centered around slight variations of the fully austenitic composition of Fe-30Mn-9Al-1Si-0.9C-0.5Mo because at this composition these steels are almost 15% less dense and have properties that are equivalent to or exceed that of Q&T 4130 castings.[14] High strengths of up to 1000 MPa with total elongations of 35% and room temperature CVN breaking energies greater than 135 J have been reported for aged low phosphorus (<0.007%P) cast steels of nominal composition Fe-30Mn-9Al-1Si-0.9C.[14,15]

Notch toughness of high strength steel has traditionally been characterized by the CVN breaking energy, which is a geometry specific parameter and is therefore only a qualitative measure of toughness under impact loading. To qualify lightweight Fe-Mn-Al-C steels for high energy absorbing applications, knowledge of the high strain rate fracture toughness, or dynamic fracture toughness, in the presence of a sharp crack is

desired. The fracture toughness of high strength steels can be characterized by either a linear elastic fracture mechanics (LEFM) approach or an elastic plastic fracture mechanics (EPFM) approach. Dynamic fracture behavior of brittle materials that have limited plasticity around the crack front is characterized by LEFM as the critical stress intensity factor, K_{Id}.[16] For ductile materials, such as the austenitic Fe-Mn-Al-C steels, failure is governed by the flow properties around the crack tip and the LEFM approach is no longer valid.[16] Thus, for materials exhibiting crack tip blunting an EPFM approach is necessary and the flow characteristics can be described by the path independent J integral, which is equivalent to the energy release rate in elastic-plastic materials.[16] The dynamic fracture toughness of ductile materials, J_{Id}, is therefore defined as the critical value of the J integral near the onset of stable crack growth.[17] However, dynamic fracture toughness (DFT) is often difficult to measure because of high crack extension rates during impact loading. Instrumented Charpy impact tests on fatigue pre-cracked specimens provide a reproducible way of measuring the time dependency of force and crack displacement at elevated loading rates; and thus, provide a means of measuring DFT. Schindler[18] has devised a single specimen technique for determining the dynamic fracture toughness, J_{Id}, from instrumented Charpy tests. The only experimental inputs necessary for this technique are the peak load (P_{max}), the energy consumed up to the peak load (E_{max}), and the total facture energy (E_{tot}), all of which can be determined in a straightforward fashion from the instrumented load vs. crack displacement data. A complete description of the test procedure and analysis of the data may be obtained from a reading of Schindler[18], ASTM E 1820[19], and ASTM E 813[17]. A standard procedure for determining DFT has not been agreed upon; however, the Schindler[18] method has been

shown to be in excellent agreement with other single specimen and multispecimen experimental methods[20] and has been widely used to characterize the dynamic toughness of both wrought and cast high strength steels.[21-23]

For a given composition, high strain rate fracture in Fe-Mn-Al-C steels is mainly dependent on heat treatment and cleanliness. Age hardening sharply reduces toughness and promotes both transgranular and intergranular cleavage fracture which is associated with κ-carbide precipitation as well as precipitation of grain boundary intermetallic phases.[24] The Schindler[18] method was recently used to compare the DFT of Q&T, Ni alloyed Cr and Mo cast steels with that of a cast Fe-30Mn-9Al-1Si-0.9C-0.5Mo (0.001%P) steel aged to an equivalent hardness of 36-38 HRC.[23] It was found that the lightweight Fe-Mn-Al-C steel achieved an equivalent dynamic fracture toughness in the hardness range of 37-38 HRC as quench and tempered HY130 (5.5% Ni) with a DFT of 153 kJ/m^2.[23] However, with less age-hardening and at a lower hardness of 32 HRC, the Fe-Mn-Al-C alloy obtained more than twice the toughness (376 kJ/m^2) of the cast Cr and Mo high strength steel.[23] Phosphorus and cleanliness also have a dramatic effect on the toughness of lightweight steels. Phosphorus in amounts greater than 0.006% P has been shown to increase the aged hardness but promote brittle cleavage fracture.[14,15,25] Howell[15] reported a 100 J decrease in CVN breaking energy in a 10 hr aged (530°C) Fe-30Mn-9Al-1Si-0.9C-0.5Mo steel as phosphorus increased from 0.001 to 0.043% P. The deleterious effects of phosphorus on the toughness of Fe-Mn-Al-C steels can be minimized by adding rare earth metals (REM) in the form of misch metal during melting to tie up phosphorus as complex (Ce,La) phosphides.[26] Melt practice can additionally affect the cleanliness of high strength cast steel because it affects the inclusion type,

morphology, and distribution; and thus, can affect the fracture behavior. Bartlett et al. have shown that excess additions of misch metal above what is needed to remove phosphorus results in the formation of brittle (Ce,La)Si_2 with a commensurate loss in CVN impact energy.[26] In addition, Schulte et al.[27] determined that there was an inverse relationship between AlN content and CVN breaking energy in Ce-treated Fe-30Mn-9Al-1Si-0.9C-0.3Mo steel castings. Castings with less than 5 particles/mm^2 of AlN had nearly twice the -40°C breaking energy than castings with 50 particles/mm^2 of AlN.[27] When casting Fe-Mn-Al-C steels, a clean melt practice utilizing Ar-cover to limit N pickup and judicious amounts of misch metal for control of phosphorus is desired for maximizing notch toughness.

From the above literature survey, it is clear that the fracture properties of lightweight Fe-30Mn-9Al-1Si-0.9C-0.5Mo steels are a complex function of age-hardening, phosphorus content, and cleanliness. However, fracture properties may also be a function of aluminum and carbon additions. The deformation mechanisms which are responsible for the high strain hardening rates and excellent ductility in high manganese steels are controlled by the intrinsic stacking fault energy.[28,29] When the stacking fault energy (SFE) is below 18 mJ/m^2, strain induced ε-martensite can occur, while twinning is reported to occur at values of SFE between 12 and 35 mJ/m^2.[30] Deformation twinning is delayed at higher values of SFE and deformation is accomplished by planar slip.[31] Additions of aluminum and carbon greatly increase the stacking fault energy and suppresses deformation twinning to a higher critical stress.[32] However, aluminum alloyed manganese steels continue to have high work hardening rates which is associated with planar glide and the formation of dislocation sheets before twinning regardless of

stacking fault energy.[33] It has been suggested that the mechanism of superior strength and plasticity in austenitic high manganese steel is the result of dynamic strain aging associated with short range order (SRO) and the formation of Mn-C dipoles in solid solution austenite.[34] Aluminum has been shown to decrease the work hardening rate in both wrought and cast steels as evidenced by tensile tests.[35,36] Correspondingly, increasing the amount of carbon in solid solution from 0.2 to 1.1% in wrought solution treated Fe-29Mn-9Al alloys has been shown to simultaneously increase both the strength and ductility.[37] However, studies of cast alloys have mostly considered the effect of silicon on the mechanical properties of the nominal Fe-30Mn-9Al-0.9C composition.[2,14,25,26] And there have been limited studies on the effect of aluminum and carbon on the high strain rate fracture of these alloys. The current study will evaluate the effects of age hardening, casting cleanliness, and aluminum and carbon additions on the dynamic fracture toughness of a cast Fe-Mn-Al-C steel.

EXPERIMENTAL PROCEDURE

Three heats with a nominal chemistry of Fe-30%Mn-X%Al-1.3%Si-0.5%Mo were prepared under argon cover in a 200 lb induction furnace. Charge materials consisted of high purity induction iron, electrolytic manganese, and 356 aluminum. All heats were melted under argon cover, calcium treated to remove sulfur, rare earth treated to remove phosphorus, and argon stirred. Dross brought to the surface by argon stirring and was removed prior to casting. Each 200 lb heat contained different levels of aluminum and each heat was divided into three separate pours with different carbon levels using increasing additions of high purity graphite, which was added in the furnace by plunging beneath the melt. Heats were tapped into a 100 lb teapot style ladle and the

weight of each heat was measured utilizing a digital Toledo scale. The resulting melt was poured into preheated investment shell molds for wear specimens and bonded olivine sand Y-block molds for DFT specimens. Heat chemistries were determined using a Verichek Foundry-Master UV arc spectrometer and a Leco CS6000 carbon-sulfur analyzer (see Table 1).

Table 1. Chemical composition of alloys in weight percent

Alloy	Fe	C	Si	Mn	P	Cr	Mo	Ni	Al	Cu
Heat 1-A	59.7	0.89	0.95	28.6	<0.0014	0.064	0.64	0.020	9.08	0.0064
Heat 1-B	59.4	1.04	0.94	28.5	<0.0014	0.073	0.59	0.020	9.49	0.0053
Heat 1-C	59.0	1.22	0.99	29.3	<0.0014	0.079	0.62	0.036	8.76	0.0065
Heat 2-A	62.7	0.88	0.87	28.4	<0.0014	0.058	0.62	0.019	6.51	0.0053
Heat 2-B	62.6	1.22	0.89	27.9	<0.0014	0.071	0.59	0.034	6.61	0.0057
Heat 2-C	61.5	1.83	0.90	29.1	<0.0014	0.075	0.56	0.048	6.14	0.006
Heat 3-A	67.5	0.90	0.86	27.2	<0.0014	0.056	0.60	0.021	2.88	0.0042
Heat 3-B	66.6	1.20	0.93	27.6	<0.0014	0.142	0.57	0.073	2.93	0.0063
Heat 3-C	66.9	1.61	0.92	27.0	<0.0014	0.214	0.55	0.105	2.89	0.0076

Y-block castings were milled into 14 mm thick rectangular plates and rough machined into 14×14×55 mm bars using a wet abrasive cut off saw. Bars were solution treated at 1050° C for 2 hrs in protective stainless steel heat treating bags and then rapidly quenched into room temperature water. Specimens were finish milled to 10×10×55 mm rectangular bars. Aging was conducted in a salt pot for up to 24 hrs at 530 ± 5°C. After heat treatment, a 2.5 mm deep notch was cut midsection using a diamond wafering blade to facilitate uniform fatigue crack initiation. The specimens were lightly ground with 800 grit abrasive to produce sufficiently smooth surfaces to measure the fatigue cracks. Care was taken not to destroy dimensional tolerances during grinding.

Specimens were fatigue pre-cracked in three point bending according to ASTM E1820 specifications. Loading on the specimens was incremenally reduce during pre-cracking to avoid large plastic strain fields that might affect measurement of the fracture toughness. The specimens were broken on a Tinius Olsen model 84 Charpy pendulum impact machine outfitted with an instrumented tup and a high-speed data acquisition system. Measurements of the crack length were conducted after fracture using optical microscopy and Image J software. The total crack length, saw notch plus fatigue pre-crack, varied between 4.0 and 6.0 mm and was determined by using the nine point averaging method described in the ASTM E813 standard. Hardness was measured using the Rockwell C scale and converted to an appropriate Brinell hardness number (BHN). Uncertainties in the reported measurements were determined as a sample standard deviation for sample sizes greater than three. Metallographic specimens for optical microscopy and inclusion analysis were prepared from broken test bars and the plane of polish was just beneth the fracture surface. Inclusion analysis was performed utilizing an

ASPEX Pica 1020 scanning electron microscope (SEM) with automated feature analysis. Fracture surfaces were retained and analysis of the fractured surface was conducted using a Hitachi S570 SEM.

RESULTS

Results from the chemical analysis showed that the aluminum content in the castings varied from 2.9 to 9.5% Al and the carbon content varied from 0.9 to 1.8% C, as shown in Table 1. Chromium and nickel were slightly elevated with levels up to 0.2% Cr and 0.1% Ni in Heat 3-C. The higher than anticipated Cr and Ni levels are a result of the method used to charge carbon. Graphite was folded into stainless steel bags and plunged beneath the melt leading to an increase in residual Cr and Ni with increasing carbon content as shown in Table 1. In the following text these alloys will be described by their heat numbers and sub-heat letters consistent with the nomenclature given in Table 1.

Pouring of Heat 2-C resulted in an incomplete fill and thus the resulting casting was full of oxide folds and macroshrinkage and was therefore of insufficient quality for evaluation of mechanical properties. Castings from the other heats were of sufficient quality for testing. In the solution treated condition, all of the castings were nearly 100% austenitic with less than 1% ferrite. A representative image of the solution treated microstructure of Heat 3-B is given in Figure 1 and shows a fully austenitic microstructure with a secondary dendrite arm spacing of 40-50 μm. The solution treated microstructures and SDAS of the other Al and C containing alloys were similar. Heats containing less than about 6% Al and less than 0.9% C showed limited age hardening

capacity and thus, Heats 3 (A, B, and C) and Heat 2-A were tested in the solution treated condition only. All other heats were evaluated in the age hardened condition.

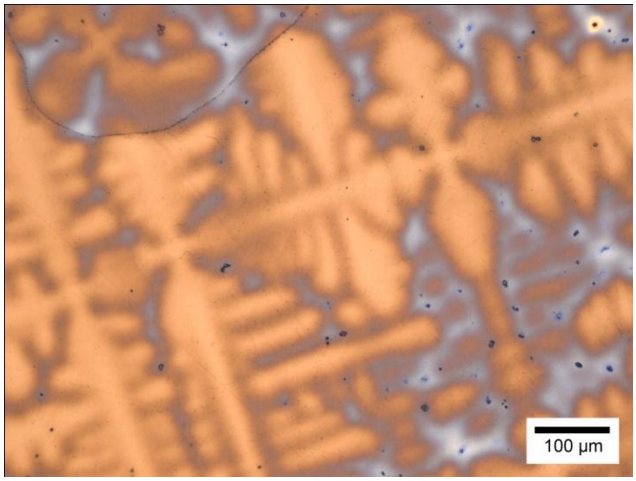

Fig. 1 The optical micrograph of an un-deformed specimen from Heat 3-B shows a fully a fully austenitic matrix and has been etched with Klemm's reagent to show segregation and porosity in the last areas to solidify.

The effect of aluminum content on the dynamic load vs. displacement curves of solution treated alloys with a constant carbon content of 0.9% is shown in Figure 2 (a and b) for specimens from Heats 2-A and 3-A. A method of moving averages was used to smooth the load vs. displacement data, as outlined by Kalthoff and Gregor,[38] to eliminate specimen "ringing" and for determination of experimental inputs used in determining DFT. Both curves in Figure 2 (a and b) show Type IV fracture, that is characterized by stable crack growth by ductile tearing, which is the desirable behavior for high energy absorbing applications.

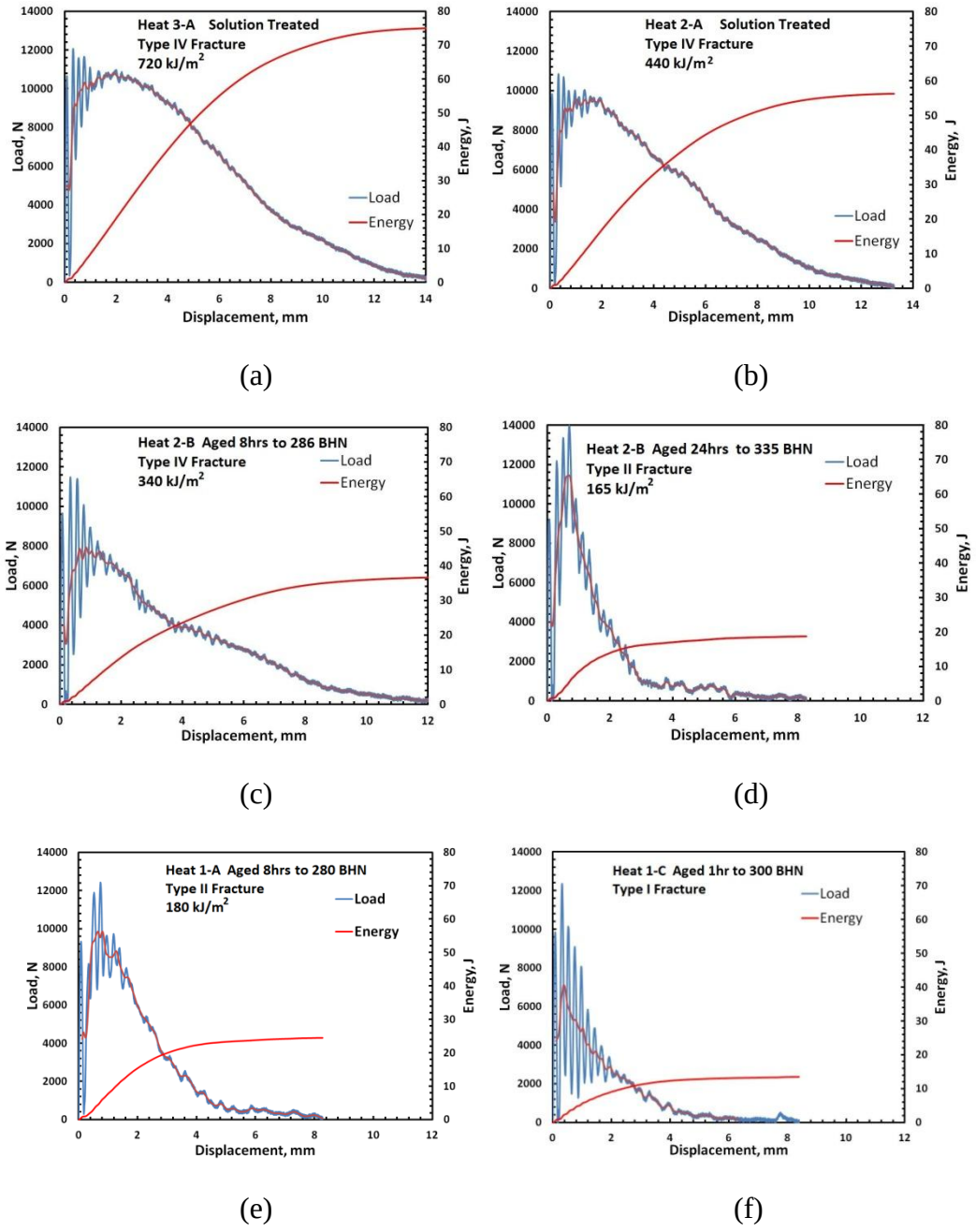

Fig. 2 Dynamic load vs. displacement curves show (a and b) type IV fracture behavior in the solution treated condition with a decrease in the fracture energy and DFT as the aluminum content increased from 2.9 to 6.5% Al at a constant carbon content of 0.9% C. Continued aging greatly reduced the toughness of specimens from Heat 2-A with (c) type IV fracture the specimen aged to 286 BHN and (d) type II fracture observed in the specimen aged to 335 BHN. For a constant aluminum content of 9%, Increasing the carbon content from (e) 0.9% C to (f) 1.2% C in specimens aged in the range of 300 BHN lead to a sharp decrease in the fracture energy and tended toward brittle type I fracture behavior with excessive ringing in the instrumented data.

Increasing the aluminum content from 2.9 to 6.5% Al decreased the dynamic load carrying capacity and lead to a decrease in the crack propagation load for the solution treated specimens shown in Figures 2 (a and b). Figures 2 (c and d) show the effect of age hardening on the crack growth resistance curves of specimens from Heat 2-B with 6.6% Al and 1.2% C. Increasing the aging time from 8hrs to 24hrs was shown to transition the fracture behavior from Type IV fracture (Figure 2c) to Type II fracture (Figure 2d) and indicates only a small amount of stable crack extension before fracture at the peak load. Increasing the amount of carbon from 0.9% C to 1.2% C in Heat 1, aged to a hardness of approximately 300 BHN, transitioned the fracture from Type II to Type I with crack initiation at the maximum load and followed by unstable crack propagation to failure, as shown in Figures 2 (e and f).

The dynamic response of Fe-Mn-Al-C alloys was shown to vary with chemistry and aging treatment as shown in Figure 2. For fractures characterized as Type II, III, and IV failure, an EPFM approach was used to determine DFT via the Schindler[18] model as J_{Id}. However, for Type I failure where unstable crack propagation was initiated at the peak load and without general yielding as shown in Figure 2 (f), a LEFM approach was utilized to determine K_{Id} according to the ASTM E 399 standard using the following equations.[21,39]

$$K_{Id} = \frac{P_{max}S}{BW^{\frac{3}{2}}} * f\left(\frac{a}{W}\right) \quad (1)$$

$$f\left(\frac{a}{W}\right) = 3\sqrt{\frac{a}{W}} * \frac{1.99-\left(\frac{a}{W}\right)\left(1-\frac{a}{W}\right)\left[2.15-3.93\frac{a}{W}+2.7\left(\frac{a}{W}\right)^2\right]}{2\left(1+2\frac{a}{W}\right)\left(1-\frac{a}{W}\right)^{\frac{3}{2}}} \quad (2)$$

In the above P_{max} is the maximum load obtained from the force vs. displacement curves, *a* is the total pre-crack length, *W* is the specimen width, *B* is the specimen thickness, and *S* is the span. K_{Id} values obtained from the LEFM method were subsequently converted to an approximate J_{Id} values using the following conversion given in Anderson.[16]

$$J_{Id} = \frac{(K_{Id})^2}{E'} \quad (3)$$

For plane strain, the effective modulus, *E'*, has the following relationship with Young's modulus, *E*, and Poisson's ratio, *v*.

$$E' = \frac{E}{(1-v^2)} \quad (4)$$

The value of Poisson's ratio was taken to be $v = 0.3$ after the work of Gebhardt et al.[40] and Young's modulus was taken to be 188 GPa after the work of Howell et al.[2]

The dynamic fracture toughness values obtained from the instrumented Charpy tests are presented in Table 2. DFT was determined utilizing EPFM and the Schindler[18] method unless otherwise indicated. Heat 1 alloys with 9% Al showed a decrease in toughness with increasing carbon content and DFT decreased from 160 kJ/m^2 to less than 77 kJ/m^2 for specimens aged in the range of 300 BHN (see Table 2). Aged specimens from Heat 1-C showed immediate fracture upon loading and thus the peak load could not reliably be determined from load vs. displacement curves and an accurate determination of DFT was not possible using the Schindler[18] method or by utilizing the LEFM model.

Table 2. Dynamic fracture toughness as a function of aluminum and carbon content.

Heat	%Al	%C	Al/C	Heat Treatment	Hardness, BHN	DFT, kJ/mm^2	Average Fracture Energy, J/cm^2
1-A	9.08	0.89	10.2	Aged 8hrs	275 ± 10	160	49
1-B	9.49	1.04	9.1	Aged 8hrs	295 ± 21	77	17
				Aged 20hrs	340 ± 15	60*	12
1-C	8.76	1.22	7.2	Aged 1hr	300 ± 13	-	10 ± 2
2-A	6.51	0.88	7.4	Solution Treated	224 ± 31	520 ± 68	115 ± 13
2-B	6.61	1.22	5.4	Aged 8hrs	286 ± 10	368	94
				Aged 24hrs	335 ± 10	110* ± 60	25 ± 9
3-A	2.88	0.90	3.2	Solution Treated	228 ± 21	605 ± 110	121 ± 18
3-B	2.93	1.20	2.4	Solution Treated	240 ± 23	731 ± 111	138 ± 17
3-C	2.89	1.61	1.8	Solution Treated	298 ± 10	240 ± 60	64 ± 19

*Determined using LEFM

Error reported as sample standard deviation for a sample size greater than three

For specimens from Heat 1-C, toughness was estimated as an average fracture energy utilizing the total breaking energy given by the dial gage and compared to the fracture energy of the other heats. The total average fracture energy decreased from 49 J/cm^2 to 10 J/cm^2 as the amount of carbon was increased from 0.9 to 1.2% C in aged

specimens with nominally 9% Al. At a constant carbon content of 1.22% C, the average fracture energy of aged alloys increased from 10 to 94 J/cm^2 with a decrease in the aluminum content from 8.8% Al to 6.6% Al as shown in Table 2 for Heats 1-C and 2-B, respectively.

Specimens from Heat 2-B that were aged for 8 hrs to a hardness of 286 BHN obtained the highest DFT out of all of the aged specimens at 368 kJ/m^2. Increasing the aging time to 24 hrs lead to a corresponding decrease in toughness to 110 kJ/m^2 for Heat 2-B specimens (see Table 2). In the solution treated condition and for a constant carbon content of 0.9% C, decreasing the amount of aluminum from 6.5% Al to 2.9% Al increased DFT by 80 kJ/m^2 for specimens from Heat 2-A and Heat 3-A, respectively. Increasing the carbon content in solution treated alloys from Heat 3, with 2.9% Al, increased the hardness from 228 to 298 BHN (see Table 2). The effect of carbon content on the solution treated DFT values is more complex. Increasing carbon from 0.9 to 1.2% C in solution treated alloys from Heat 3 resulted in a 125 kJ/m^2 increase in DFT from 605 to 731 kJ/m^2. However, further increasing the carbon content to 1.6% C resulted in a sharp drop in the toughness to less than 245 kJ/m^2, as shown in Table 2.

Fractured test specimens were retained for analysis of the fracture mode utilizing scanning electron microscopy (SEM). In all of the following images, the notched edge is oriented toward the top of the figure and the direction of crack propagation is from the top to the bottom of the figures. The effect of increasing carbon content in solution treated 2.9% Al specimens, from Heats 3 (A and C), is shown in Figure 3. Figures 3 (a and b) show the interface between the fatigue pre-cracked in the top of the figure and the onset of crack initiation and propagation at the bottom of the figure for specimens with

0.9 and 1.6% C, respectively. The presence of an extensive stretch zone at the interface indicates appreciable crack-tip blunting before crack extension. Increasing the amount of carbon to 1.6 % increased the plasticity as evident by the larger and deeper microvoids at the interface of the 1.6% C specimen in Figure 3 (b). However, the image of the final fracture area of the 0.9% C specimen shows ductile failure with microvoid nucleation and coalescence around rather large groups of inclusions (Figure 3 (c)) while the 1.6% C specimen in Figure 3 (d) shows low energy ductile fracture through interdendritic regions. A higher magnification image in Figure 3 (f) of the same area as in Figure 3- (d) shows a high density of brittle second phase particles that are observed to be fractured in interdendritic regions of the 1.6% C specimen. It should be noted that all of the specimens from Heat 3 had a large amount of coarse and closely spaced AlN particles that in some cases were larger than 10 μm as shown for the specimen from Heat 3-A in Figure 3 (e). The fracture surfaces of aged specimens from Heat 1 with 9% Al and different levels of carbon are shown in Figure 4. The specimens in Figure 4 were all aged in the hardness range of 300 BHN. Increasing the carbon content from 0.9 to 1.2% C tended toward brittle fracture. Figure 4 (a) shows that the fracture mode in the 0.9% C specimen is a combination of mainly transgranular ductile fracture with large dimples nucleated at inclusions and intergranular ductile fracture with shallow dimples nucleated at grain boundaries.

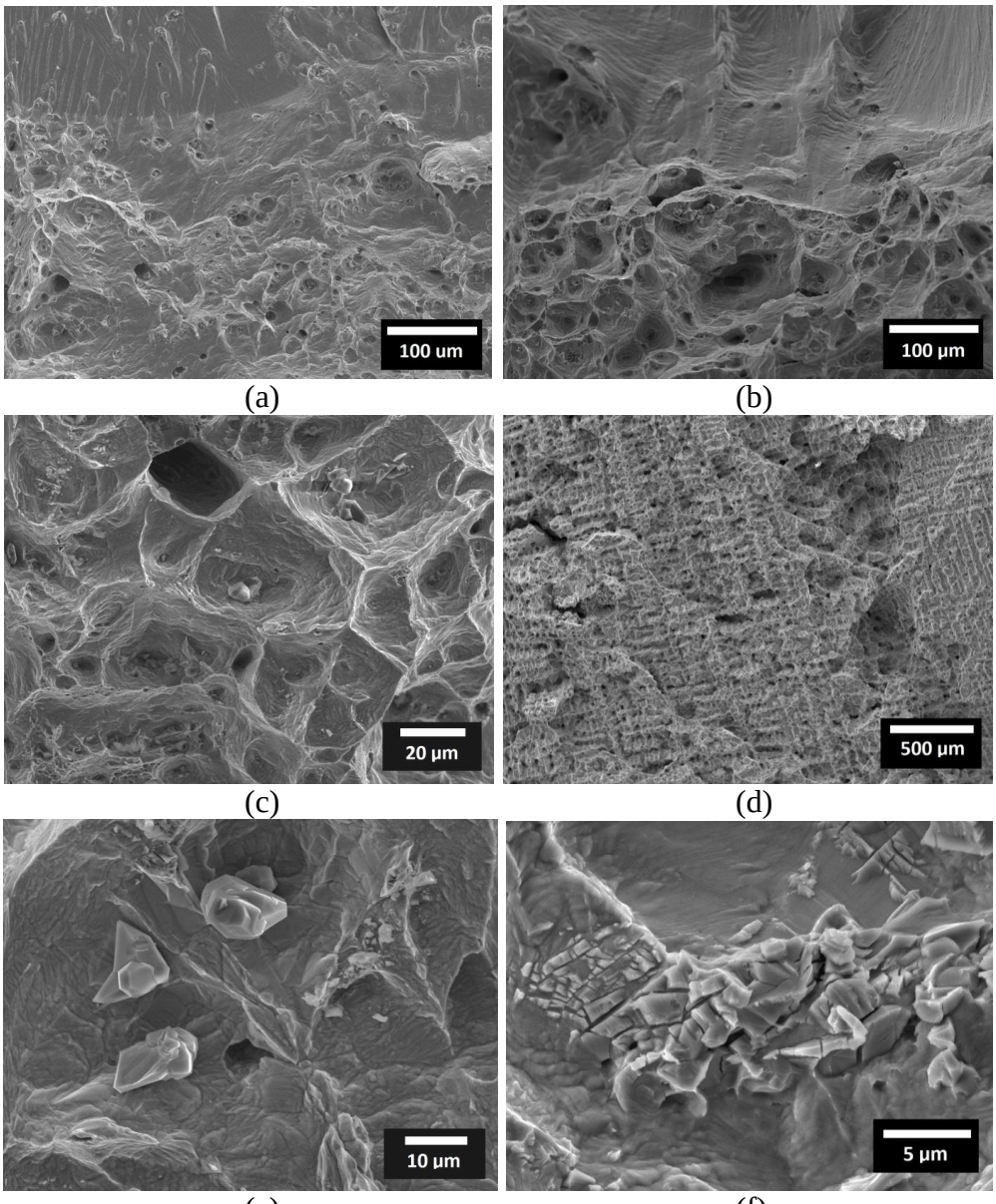

Fig. 3 Fracture surfaces of solution treated specimens from (a, c, and e) Heat 3-A and (b, d, and f) Heat 3-C show the effect of increasing the amount of carbon from 0.9 to 1.6% C in the 2.9% Al alloys. (a and b) The interface between the fatigue pre-cracked area (top) and the onset of crack initiation shows ductile rupture and an extensive stretch zone in both specimens, however, dimples are much larger and deeper in (b) indicating an increase in ductility with increasing carbon content. (b and d) Images of the final fracture region in (c) Heat 3-A and (d) 3-C show high energy ductile rupture in Heat 3-A and low energy interdendritic fracture in Heat 3-C. (e and f) Higher magnification images of the same areas as in (c and d) show closely spaced AlN inclusions in (e) that are in some cases larger than 10 µm on the fracture surface of the specimen from Heat 3-A and (f) large areas of a hard and brittle second phase believed to be either a complex carbide or intermetallic phase that is shown fractured in the interdendritic regions of the specimen from Heat 3-C.

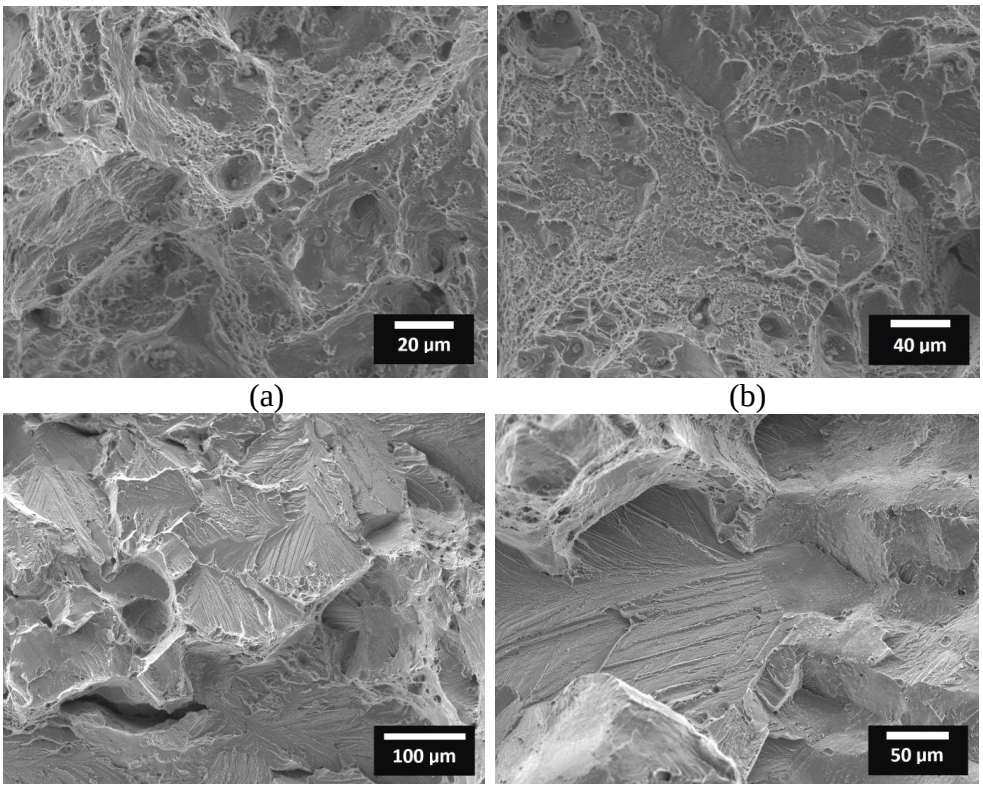

Fig. 4 The fracture surfaces of specimens from (a) Heat 1-A aged for 8hrs, (b) Heat 1-B aged for 8hrs, and (c and d) Heat 1-C aged for 1hr in the hardness range of 300 BHN show the tendency toward brittle fracture as the carbon content is increased from 0.9 to 1.2% C. (a) The specimen from Heat 1-A shows ductile fracture with shallow microvoid nucleation and coalescence around inclusions and at grain boundaries. (b) Increasing the carbon content to 1.0% C in specimens from Heat 1-B resulted in a mixed mode fracture with areas of cleavage-like fracture. (c) A further increase in carbon to 1.2% C resulted in brittle cleavage fracture. (d) A higher magnification image of the same area as in (c) shows that cleavage fracture in the 1-C alloy that is both intergranular and transgranular in nature.

Increasing the amount of carbon to 1.0% C in an aged specimen from Heat 1-B produced a mixed mode fracture with shallow voids and areas of mainly transgranular cleavage-type fracture as shown in Figure 4 (b). Further increases in carbon up to 1.2% produced mostly transgranular and intergranular cleavage fracture in an aged specimen from Heat 1-C, as shown in Figure 4 (c and d).

Figure 5(a) shows ductile failure with large dimples that have nucleated and grown around inclusion clusters in a specimen from Heat 2-B (6.6% Al and 1.2% C) that was aged for 8hrs to a hardness of 290 BHN. The effect of aluminum content on the fracture mode of alloys with 1.2% C aged to approximately 300 BHN can be observed by comparing Figure 4 (c) and Figure 5 (a). The specimen with 8.8% Al in Figure 4 (c) shows mostly brittle cleavage fracture. In contrast, when the aluminum level is reduced to 6.6% Al the fracture mode is completely ductile in nature as shown in Figure 5 (a). Some specimens showed fracture through large areas of porosity as shown in Figure 5 (b) and those specimens with widespread porosity on the fracture surface were excluded from calculation of DFT. Increasing the degree of age hardening from a nominal hardness of 300 BHN to 340 BHN produced brittle fracture in all alloys. Increasing the aging time to 24hrs in a specimen from Heat 2-B (6.6% Al and 1.2% C) produced a mixed mode fracture with limited areas of ductile fracture as well as both intergranular and transgranular type cleavage fracture as observed in Figures 5 (c and d). A high magnification image of a transgranular cleavage facet on the surface of the 24hr aged specimen in Figure 5 (d) shows either cracking in shear bands or de-cohesion of specific atomic planes that are shown in two crystallographic directions. The orientation of the cleavage plane could not be determined.

Standard metallographic specimens were prepared from sections just beneath the fracture surface. Figure 6 shows the deformed microstructures of solution treated specimens from Heat 3 and Heat 2-A.

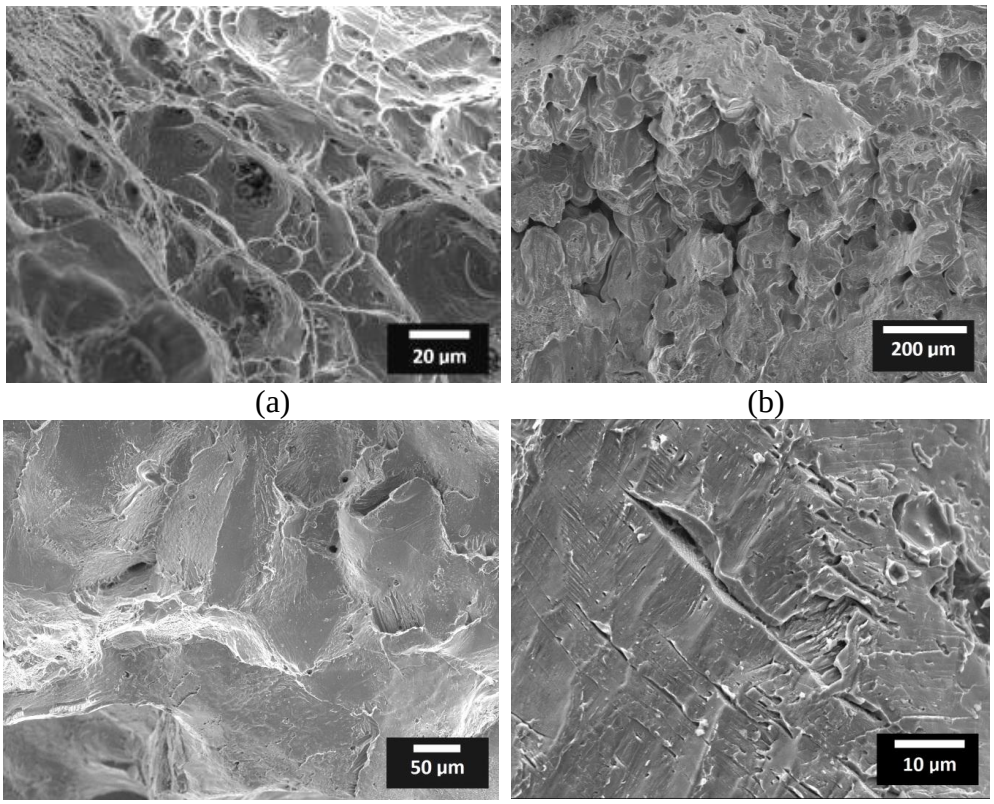

Fig. 5 (a) The fracture surface of a specimen from Heat 2-B that was aged for 8hrs to a hardness of 290 BHN shows ductile fracture around clusters of inclusions. (b) Fracture through a large area of porosity in a specimen from Heat 2-B. (c) After aging for 24hrs to a hardness of 335 BHN, a specimen from Heat 2-B shows intergranular fracture and some areas of transgranular fracture. (d) Areas on some grains in specimens from Heat 2-B that were aged for 24hrs showed either cracking in shear bands or de-cohesion of atomic planes.

At a distance greater than approximately 3 mm from the last area to fail, deformation twins were observed only in favorably oriented grains and only in solution treated specimens with 2.9% Al and less than 1.2% C as shown in Figures 6 (a and c). Figures 6 (b and d) show the deformation structure corresponding to the last area of the bar to fracture (ductile hinge) in specimens from (b) Heat 3-A and (d) Heat 3-B. High densities of mechanical twins were observed in two crystallographic directions intersecting shear bands. The frequency of twins was higher in the 3-B specimen, however this may only be

an effect of sectioning or grain orientation. The micrograph of the solution treated specimen from Heat 3-C shows heavy segregation in interdendritic areas and no evidence of deformation in the microstructure either by deformation twinning or by planar slip as shown in Figure 6- (e). Figure 6 (e) shows a large amount of brittle plate like precipitants in the interdendritic areas of the Heat 3-C specimen. The presence of this phase was also noted on the fracture surface of this bar as shown in Figure 3 (d) and has contributed to the observed intergranular fracture and produced a more than 400 kJ/m^2 loss in toughness. Energy dispersive X-Ray spectroscopy (EDS) established that this brittle phase was rich in Cr, Mn, and Mo and is thus either a complex carbide intermetallic phase. Increasing the aluminum content from 2.9 to 6.5% decreased the frequency of twinning in solution treated specimens and deformation twins were observed only in a few heavily deformed grains from the plastic hinge areas of specimens from Heat 2-A as observed in Figure 6 (f). Figures 7 (a) and (b) show the area just beneath the fracture surfaces of specimens from Heat 1-A (9% Al and 0.9% C) and Heat 1-C (8.8% Al and 1.2% C) that were aged to approximately 300 BHN. Etching revealed that the deformation mechanism was predominately planar dislocation slip in both alloys with no evidence of deformation twins. Decreasing the amount of aluminum to 6.6% Al in aged castings did not change the deformation mechanism and planar slip was observed in specimens from Heat 2-B that were also aged to approximately 300 BHN as shown in Figure 7 (c). Increasing the aged hardness to 340 BHN resulted in areas of continuous precipitation of κ-carbide and/or an intermetallic phase on grain boundaries as shown in Figure 7 (d).

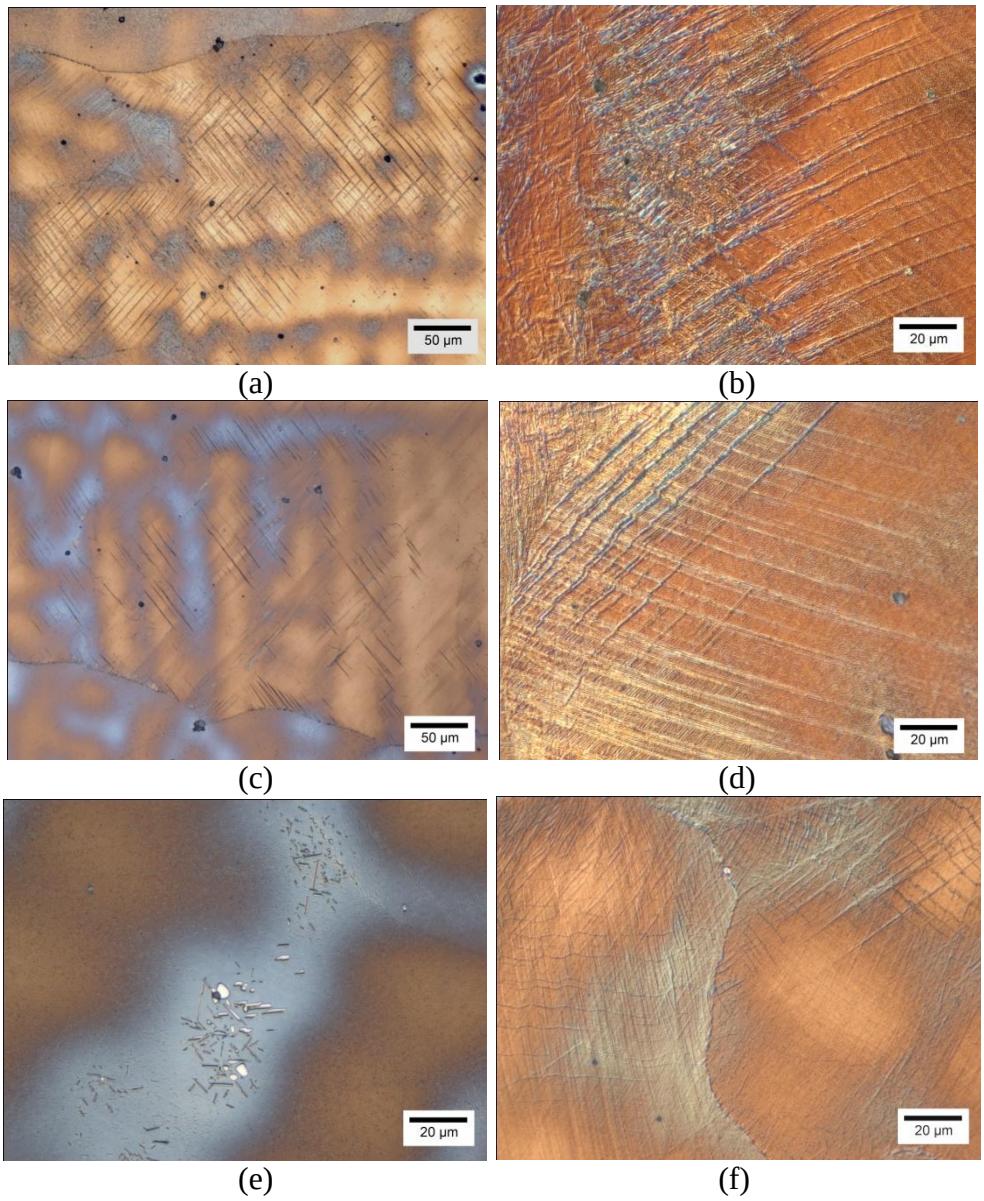

Fig. 6 The microstructures of solution treated specimens from (a and b) Heat 3-A (2.9% Al and 0.9% C), (c and d) Heat 3-B (2.9% Al and 1.2% C), (e) Heat 3-C (2.9% Al and 1.6% C), and (f) Heat 2-A (6.5% Al and 0.9% C) show the deformed area just beneath the fracture surface. (a and c) The microstructures of an area a distance 3-4 mm away from the last portion of the (a) Heat 3-A and (c) Heat 3-B specimens to fail shows deformation twins only in favorably oriented grains. (b and d) The differential contrast (DIC) images of the last area to fail in specimens from (b) Heat 3-A and (d) Heat 3-B show a high density of mainly fine deformation twins with intersecting shear bands. (e) Neither deformation twins nor slip traces were observed in the specimen from Heat 3-C indicating that plastic deformation was not widespread. Regions in interdendritic areas of the Heat 3-C specimen are heavily segregated and show the precipitation of a hard plate-like phase. (f) The DIC image of the last area to fail in a solution treated specimen from Heat 2-A shows less of a frequency of deformation twins with increasing aluminum to 6.5% Al. Specimens etched with 4% Nital and Klemm's.

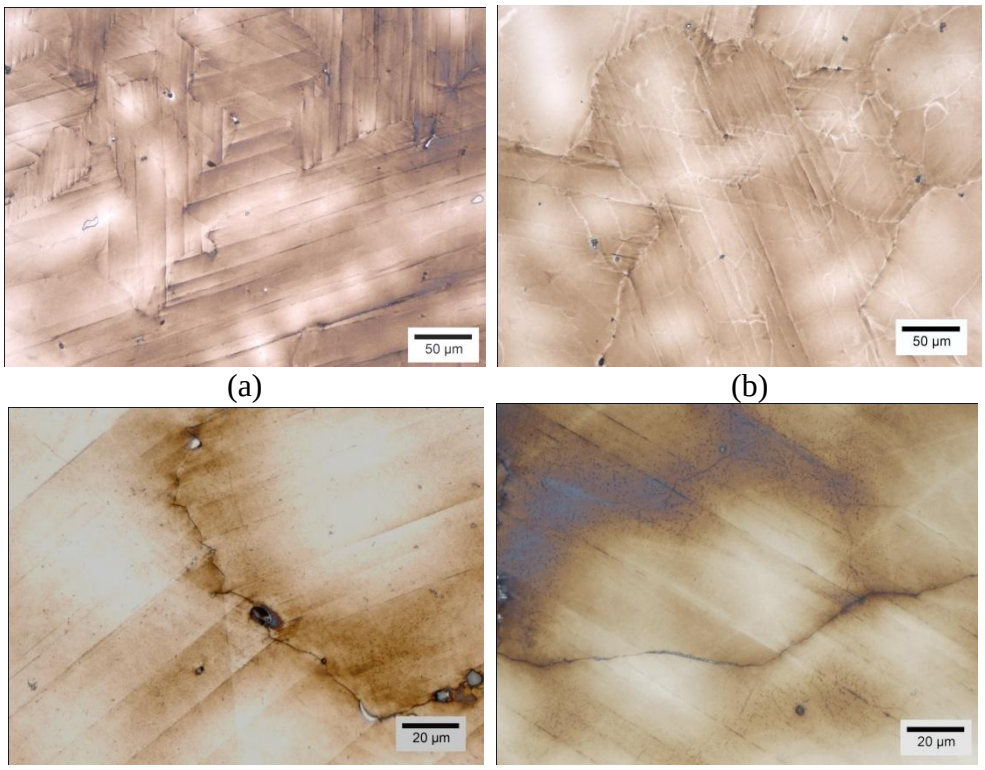

Fig. 7 The microstructures of specimens age hardened in the range of 300 BHN are shown in (a) for Heat 1-A (9% Al and 0.9% C), (b) for Heat 1-C (8.8% Al and 1.2% C) and (c) for Heat 2-B (6.6% Al and 1.2% C)and show planar slip bands and serrated grain boundaries. (d) Areas of continuous precipitation of κ-carbide and/or an intermetallic phase was noted on the grain boundaries of a specimen from Heat 2-B that was aged for 24hrs to 340 BHN.

The normalized inclusion density and average inclusion diameter as a function of inclusion type are shown for the different carbon and aluminum laboratory cast Fe-Mn-Al-C alloys in Figure 8 and are compared with the inclusions in a previously reported[23] commercially cast Fe-30Mn-9Al-1Si-0.9C-0.5Mo-0.001%P steel without rare earth additions. All of the inclusion analyses for the different steels were determined for a particle or pore major diameter of 1 to 80 µm. Inclusions in the laboratory heats consisted mainly of AlN, globular MnO and MnS, and complex rare earth (RE) oxides and phosphides of Ce and La as shown in Figure 8. Inclusions in the laboratory heats

were found mostly clustered together in the last areas to solidify and most are of the mixed inclusion type. Laboratory heats contained up to four times the amount of AlN as the commercially cast steel and these inclusions were on average much larger, with an average diameter of 5 μm, as shown in Figures 8 (a and b). Large and clustered inclusions are often the result of holding the melt too long before pouring and exposure to the atmosphere. AlN density and size was not a function of total aluminum content and steels from Heats 2-B and 3-C with 6.5% and 2.9% Al, respectively, contained the highest AlN density with 45 inclusions/mm^2. This can be compared with an AlN density of 12 inclusions/mm^2 in the commercially cast steel (see Figure 8 (a)). Most of the AlN observed in the commercially cast steel was an average diameter of 2 μm and existed as a complex type of inclusion consisting of an AlN core surrounded by a MnS or MnO shell (see Figure 8 (a)). However, the AlN in the laboratory heats was generally found to be without an encapsulating MnS shell and this is because rare earth metals like cerium are much more chemically active in the melt than Mn. Rare earth inclusions were complex in nature consisting of a phosphide core surrounded by an oxide shell and were found in combination with AlN in interdendritic regions. Additionally, a hard and complex carbide or intermetallic phase that is rich in Ti and Mo was found in varying degree in all of the laboratory heats as shown in Figure 8 and designated as complex carbide.

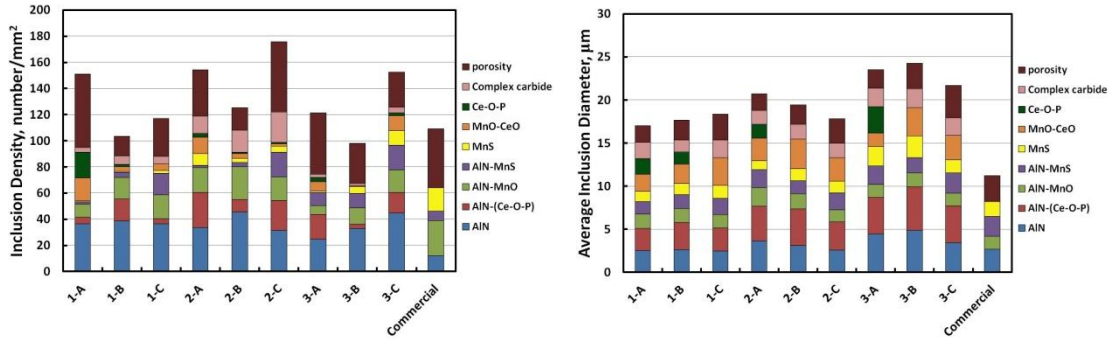

(a) (b)

Fig. 8 (a) Laboratory heats contained more than twice the AlN density as compared to a commercially cast Fe-30Mn-9Al-1Si-0.9C-0.5Mo (0.001% P) without cerium addition. (b) Inclusions were generally much larger in the laboratory heats.

The amount of this carbide or intermetallic phase was significant only in the castings from Heat 2 where the total amount was greater than 15% of the total inclusion density (see Figure 8 (a)). The source of the titanium is unknown but may have been introduced into the melt by polling rods used to plunge the charge carbon and RE additions underneath the surface of the melt during melting. Porosity was high in all castings except for 1-B and 2-B and highest in Heats 1-A and 2-C with more than 50 pores/mm^2, as shown in Figure 8 (a). Figure 9 (a) shows the total inclusion densities from the current study in comparison to the inclusion densities of the previously reported[23] commercially cast *Fe-30Mn-9Al-1Si-0.9C-0.5Mo* steel. Total average inclusion density (inclusions and porosity) for the laboratory heats was much greater, 130 to 200 inclusions/mm^2, than that of the commercially cast alloy, 77 inclusions/mm^2. The highest inclusion density was found in the casting from Heat 2-C which was the last metal poured from the ladle and the casting did not completely fill. The average inclusion diameter was larger, 3 µm, for castings from Heat 3 than for all other heats as shown in Figure 9 (b).

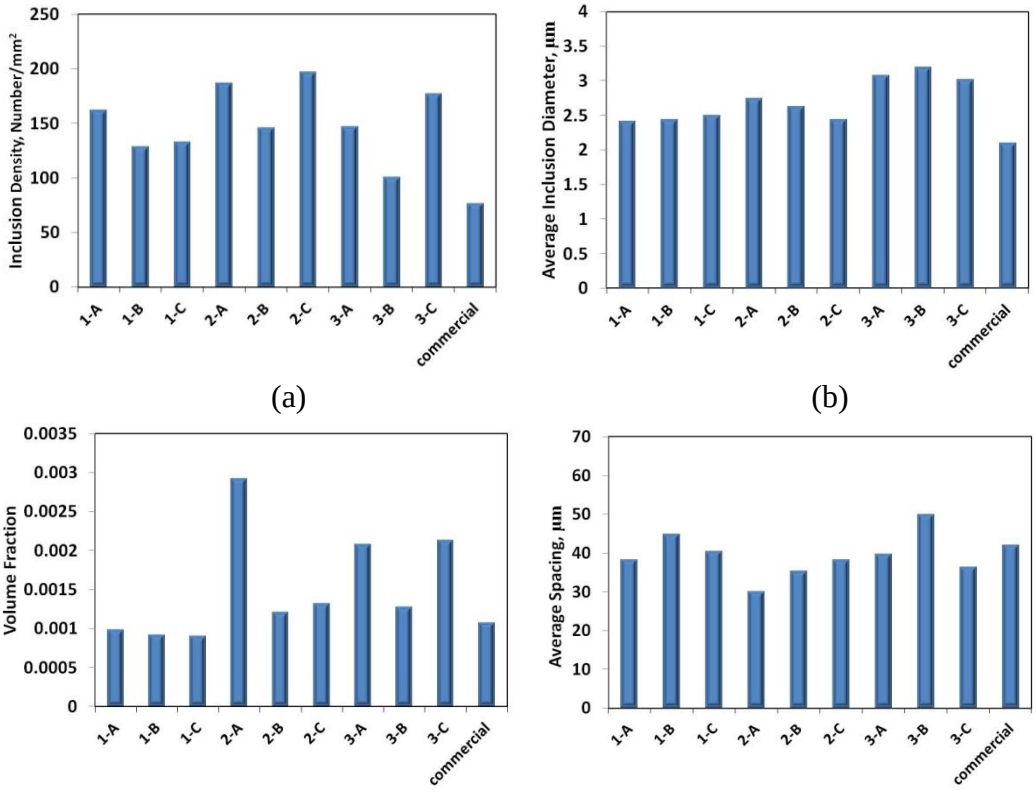

Fig. 9 (a) The total average inclusion densities of the laboratory heats with different C and Al contents are in most cases more than twice that of the commercially cast Fe-30Mn-9Al-1Si-0.9C-0.5Mo steel. (b) The average inclusion size was slightly larger in laboratory cast steels from Heat 3, which were poured last. (c) Total average volume fraction of inclusions was largest for the Heats 2-A, 3-A, and 3-C. (d) The average spacing between inclusions was lowest in Heat 2-A and greatest in Heat 3-B.

The average inclusion diameters of the laboratory cast heats were all larger than the average inclusion diameter of the commercially cast heat which was 2 μm. Volume fraction of inclusions for the different heats is given in Figure 9 (c) and shows the most inclusion coverage in test bars from 2-A and Heat 3. Heat 1 castings had the lowest volume fraction of inclusions at 0.001 and was comparable to the volume fraction of inclusions in the commercially cast steel. Average inclusion spacing for the different steels is given in Figure 9 (d).

Specimens from Heat 2-A were shown to have smallest inclusion spacing at an average of 30 μm. Heat 3-B had the largest average inclusion spacing at 50 μm.

DISCUSSION

Dynamic fracture toughness of the Fe-Mn-Al-C steels in the current study was a complex function of chemistry, heat treatment, and cleanliness. Table 3 shows the composite mechanical properties of the respective laboratory heats in comparison with the mechanical properties of two commercially produced steels of nominal composition Fe-30Mn-9Al-1Si-0.9C-0.5Mo with[26] and without[23] cerium additions in the form of misch metal. Tensile properties of the laboratory heats were obtained from the work of Buckholz.[41]

In the solution treated condition and for a constant aluminum content of 2.9% Al, increasing the amount of carbon in solution increased both the yield and ultimate strengths with a commensurate increase in ductility and DFT as shown for alloys from Heat 3 in Table 3. DFT was highest in the Heat 3-A steel with 1.2% C and 2.9% Al at 730 kJ/m^2. However, increasing carbon to 1.6% C produced an almost 500 kJ/m^2 decrease in toughness without a significant decrease in ductility and the total elongation remained close to 40%. This significant decrease in toughness is directly related to the presence of a hard and brittle Cr, Mn, and Mo complex carbide or intermetallic phase that was found fractured on the surface of broken test specimens from Heat 3-C as shown in Figure 3 (f). In contrast, fracture in the other solution treated materials was by void nucleation around rather coarse and closely spaced AlN inclusions which failed by decohesion from the matrix.

Table 3. Mechanical properties of laboratory heats in comparison to previously reported and commercially cast Fe-30Mn-9Al-1Si-0.9C-0.5Mo steels with[26] and without[23] cerium treatment.

Heat	%Al	%C	Heat Treat.	Hdns., BHN	YS MPa[41]	UTS MPa[41]	% Total Elong.[41]	DFT, kJ/mm^2	Average inclusion density, #/mm^2
1-A	9.1	0.9	Aged	260-275	750	809	14[a]	160	162
1-B	9.5	1.0	Aged	295-315	840	920	19[a]	77	129
			Aged	340-360	1008	1085	9[a]	60*	
1-C	8.8	1.2	Aged	300-310	720	900	23[a]	-	133
2-A	6.5	0.9	Sol. T.	205-225	445	792	45[a]	520 ± 68	187
2-B	6.6	1.2	Aged	280-290	658	792	31[a]	368	146
			Aged	335-350	800	939	16[a]	110* ± 60	
3-A	2.9	0.9	Sol. T.	210-230	306	680	27[a]	605 ± 110	147
3-B	2.9	1.2	Sol. T.	220-240	415	743	42.[a]	731 ± 111	101
3-C	2.9	1.6	Sol. T.	290-300	530	889	39[a]	240 ± 60	177
C. Cast Ce[26]	8.8	0.9	Aged	290-300	750	825	25[b]	140	245
C. Cast[23]	8.8	0.9	Sol. T.	200	452	737	64[b]	-	77
			Aged	290-300	728	795	28[b]	376 ± 69	
			Aged	350-360	873	953	20[b]	153 ± 25	

*Determined using LEFM

a – elongation determined in a 30 mm gage section

b – elongation determined in a 25 mm gage section

Error reported as sample standard deviation for a sample size greater than three

During ductile fracture, nucleation of voids can occur either at the particle/matrix interface by decohesion or by voids created at brittle particles that fracture during deformation. Ultimate failure will progress by the growth of voids due to further plastic strain of the matrix and then linkage of the voids leading to final fracture.[16]

In the presence of a sharp crack or a notch, crack progression is often dependent on inclusions and second phase particles that fracture or nucleate voids within the crack tip process zone.[4] In the case of the Heat 3-C, it is apparent that under dynamic loading the fracture strength of the Cr and Mo rich phase is less than the cohesive strength of the particle and matrix interface. In contrast, the AlN particles fail by decohesion, as shown in Figures 3 (c and e), which indicates that the fracture strength of the AlN is greater than the cohesive interface strength. Bartlett et al.[23] have shown that the dynamic fracture toughness of cast Cr and Mo steels is a function of inclusion type and fracture through TiN inclusions resulted in large void formation and reduced the dynamic toughness by 100 kJ/m^2 when compared with steels that contained globular inclusions that formed voids by decohesion from the matrix.[23] Therefore, the loss in toughness of the Heat 3-C steel is the result of low energy ductile fracture through the brittle fracture of the Cr and Mo rich phase. Tensile ductility and work hardening capacity were not severely affected by the presence of the Cr and Mo rich phase and the matrix appears to have more ductility in the stretch zone of broken DFT bars when compared with specimens from Heat 3-A which contained less carbon content as shown in Figure 3 (a and b). Thus, in the solution treated condition, increasing the amount of carbon increased the strength, ductility, and DFT. These results are consistent with those of Chang et al.[37] who show an increase in tensile strength and elongation with increasing carbon addition in a Fe-29Mn-

9Al-(0.2-1.1)C steel. Additionally, Abbasi et al.[36] show an increase in work hardening and strength with increasing carbon and a decrease in work hardening and ultimate tensile strength with increasing aluminum in a Fe-(12-14)Mn-(0-3)Al-(1.2-1.4)C Hadfield steel. Furthermore Abbasi et al. showed that yield strength increased with aluminum addition.[36] In the current study, increasing the aluminum content from 2.9 to 6.6% Al in solution treated alloys with 0.9% C resulted in an increase in both the yield and ultimate tensile strength as well as the total elongation but decreased toughness by almost 100 kJ/m2 as shown in Table 3.

Carbon and aluminum are both known to raise the stacking fault energy in Fe-Mn-Al-C steels and thus suppress mechanical twinning.[43] In the current study, mechanical twinning was only observed in solution treated specimens within favorably oriented grains and in the last areas of the bar to fail corresponding to the regions of the most intense strain (see Figure 6). Mechanical twinning was not observed in the solution treated 2.9% Al DFT specimens with the highest carbon content of 1.6% C, however, this alloy had equivalent ductility and work hardening capacity as the solution treated alloys with lower carbon contents as shown in Table 3. Increasing aluminum to 6.6% Al in solution treated specimens suppressed twinning and mechanical twins were only observed in highly strained regions in the last areas to fail of DFT bars as shown in Figure 6 (f). Increasing aluminum did not significantly decrease the work hardening capacity in solution treated steels as evidenced by a similar difference between the yield and ultimate tensile strengths with increasing aluminum content as given in Table 3. Recently, Park et al.[44] studied the effects of aluminum on the plastic deformation of Fe-22Mn-(0-6)Al-0.6C steels and determined that deformation in all steels was dominated

by planar glide before the occurrence of mechanical twinning regardless of SFE. The occurrence of planar glide in Fe-Mn-Al-C steels with rather large values of SFE, > 70 mJ/m^2, has been attributed to short range order (SRO) in the solid solution state and the phenomenon of glide plane softening.[31,44] The relationship between SRO and planar slip can be explained in the following way. The initial dislocation that moves through the FCC lattice will destroy SRO and as such, this dislocation will face a higher resistance to slip than dislocations that follow. Dislocations that follow will push against this first dislocation to help it overcome the higher resistance and this will lead to an increase in the slip velocity and the amount of plastic deformation. Slip will be easier for subsequent dislocations to follow on the same plane where the SRO has been destroyed. Thus, plastic deformation will be localized to a single slip plane and this effect is called glide plane softening.[4]

The short range ordering of Mn-C couples in solution treated high manganese steel has been suggested by many to be the principal cause of rapid work hardening and increased plasticity in *Fe-Mn-Al-C* steels.[34,43,44,46-49] Medvedeva et al[50] have shown that the formation of Mn-C couples in solid solution austenite is energetically favorable in high manganese steels and therefore adding solid solution carbon would increase the number of Mn-C couples and increase work hardening. Adding aluminum favors SRO with similarities to the $E2_1$ structure of κ-carbide and would promote glide plane softening.[50] To verify the major deformation mode in solution treated specimens, TEM thin films were prepared from sections just beneath the fracture surface of broken specimens from Heat 3-A in regions corresponding to the last areas of the test bar to fail. Specimens from Heat 3-A were chosen because this alloy contained the lowest amount of

carbon and aluminum and thus had the lowest SFE. The bright field image of the deformation structure of a specimen from Heat 3-A is shown in Figure 10. Although twins were observed in Heat 3-A in the last areas of the test bar to fail by optical microscopy (Figure 6 (b)), mechanical twins were not observed in any of the four TEM thin films that were prepared. Instead, the deformation structure in Heat 3-A consisted of a planar array of dislocations as observed in Figure 10. Thus, it is suggested that the major deformation mechanism is planar slip before the occurrence of mechanical twining even in the solution treated alloy with the lowest SFE.

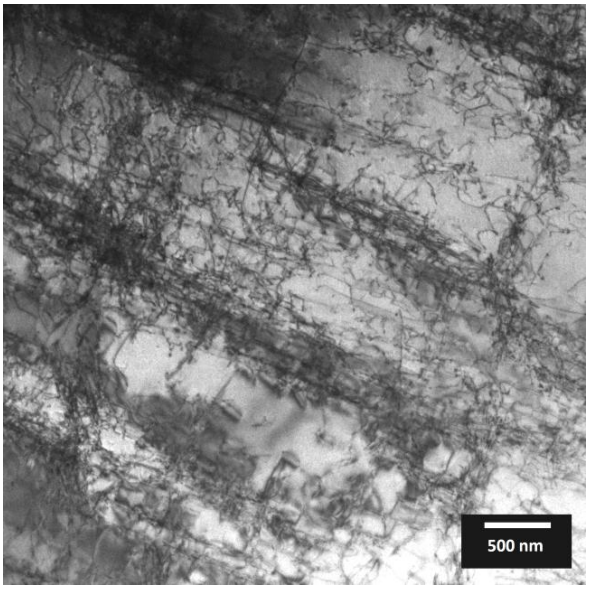

Fig. 10 The bright field TEM image of the deformation structure just beneath the fracture surface of the solution treated DFT specimen from Heat 3-A shows a planar array of dislocations in two principal directions.

Therefore the results of the current study suggest that increasing the amount of solid solution carbon in Fe-Mn-Al-C alloys increases both work hardening as well as toughness and this is the result of dynamic strain aging produced by the interaction of

dislocations with carbon in Mn-C dipoles. The effect of aluminum content on the toughness of solution treated specimens from the current study is shown in Figure 11. Aluminum was found to decrease toughness in both solution treated and aged alloys. Increasing the amount of aluminum in the solution treated alloys suppressed twinning and is thought to have reduced the number of Mn-C pairs leading to a reduction in toughness. These results are consistent with the work of Hwang et al.[51] who report a decrease in the dynamic strain aging as the amount of aluminum was increased from 0 to 6% Al in a solution treated Fe-22Mn-XAl-0.6C steel. They report that the microstructure of the aluminum containing steels was dominated mainly by planar glide.[51] Park et al.[44] report a decrease in work hardening, tensile strength, and ductility with increasing aluminum content in a solution treated Fe-22Mn-(0-6)Al-0.6C steel. Aluminum additions have also been shown to reduce the work hardening rate in Fe-Mn-C steels by reducing the carbon mobility and thus decreasing the ability by which Mn-C pairs can re-arrange to pin dislocations.[46,49] A study by Buckholz on the same alloys presented here showed that as the amount of aluminum was increased from 2.9% to 9% Al in solution treated alloys the total elongation to fracture increased from 27 to 50% and the work hardening coefficient decreased from 0.47 to 0.28.[41] The dynamic load carrying capacity of solution treated steels in the present study decreased with increasing aluminum content, as shown in Figure 2 (a and b) and this is most likely related to a decrease in work hardening ability with increasing aluminum additions. Short range ordering of Fe-Al-C clusters in aluminum alloyed high manganese steels is energetically preferable and has been suggested to promote planar slip and glide plane softening resulting in enhanced ductility.[50]

A study by Park et al. showed evidence of SRO in a solution treated Fe-28Mn-9Al-0.8C steel corresponding to Fe-Al-C clusters as evidenced by $E2_1$ superlattice reflections and deformation by planar glide prior to mechanical twining regardless of the amount of aluminum.[44]

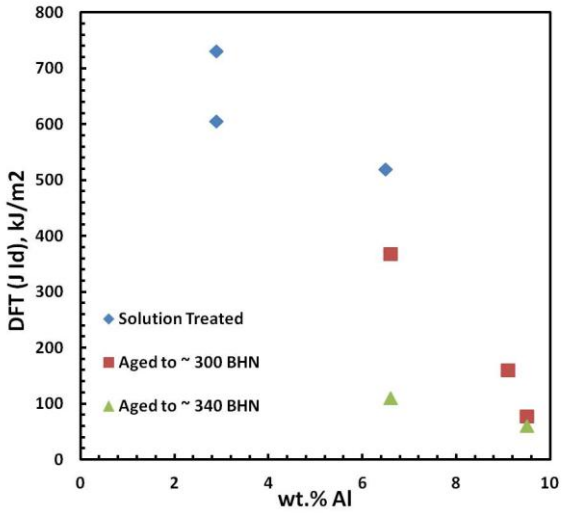

Fig. 11 Aluminum is shown to decrease the dynamic fracture toughness in both solution treated and aged steels.

Increasing the amount of aluminum and carbon greatly increased the age hardening kinetics at 530°C and thus the precipitation of κ-carbide. Alloys with less than 6% Al and 1% C showed no appreciable hardening. Increasing the aluminum content decreased the dynamic fracture toughness in aged alloys by as much as 300 kJ/m^2 as shown in Figure 11. Although carbon increased the solution treated toughness, increasing carbon in aged alloys sharply reduced toughness, as shown in Figure 12, and produced brittle cleavage-type fracture in a specimen from Heat 1-C that was aged to a hardness of 300 BHN. Although there are limited studies on the effect of carbon and

aluminum additions on the toughness of aged steels, it has been shown that age hardening results in a significant reduction in work hardening[2] and toughness.[24] Acselrad et al.[24] reported a 250 MPa√m decrease in toughness in a Fe-28Mn-8.5Al-1C alloy after aging for 15hrs at 550°C and this was attributed to intense κ-carbide precipitation in the matrix.

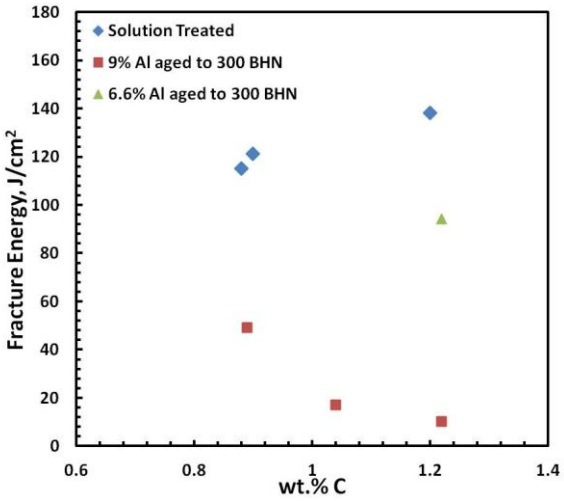

Fig. 12 Increasing the amount of solid solution carbon in solution treated steels increased the average fracture energy. However, in aged steels increasing the amount of carbon sharply reduced the toughness and promoted brittle failure. At equivalent carbon content, decreasing the amount of aluminum increased the toughness.

Acslerad and co-workers reported that aging produced a brittle transgranular cleavage-like fracture in which cleavage facets were found to contain linear markings along two or three different directions.[24] They proposed that the mechanism of brittle cleavage fracture with aging was the result of "slipping off" along the slip plane producing a {111} type fracture facilitated by planar slip and shear strain localization in shear bands resulting from κ-carbide precipitation.[24] This type of brittle cleavage fracture has been observed in nitrogen bearing austenitic steels and is facilitated by planar slip arising from

short range ordering of nitrogen.[52-54] Short range order and shearable precipitates both promote planar slip and dislocations are concentrated in narrow shear bands.[53] The accumulation of dislocation induced defects in shear bands will weaken the band to such an extent that the tensile component of the force on the band will cause cracking and final decohesion of the glide plane.[53] κ-carbide is known to be a weak dislocation barrier and cyclic softening in an aged Fe-30Mn-8.7Al-1C steel was reported by Ho et al. to be the result of planar slip facilitated by the shearing of coherent κ-carbide particles.[55] The fracture surfaces of the aged specimens from Heat 1-C (Figure 4 (d)) and Heat 2-B (Figure 5 (d) show linear markings on cleavage facets that are similar to the ones observed in the study by Acslerad et al.[24] and others.[52,53] Thus, it is suggested that age hardening and the precipitation of κ-carbide contributes to planar slip and localization of dislocations in narrow slip bands that promote cleavage fracture by the glide plane "slipping off" mechanism. Carbon and aluminum decrease the toughness of aged alloys and this may be the result of increased κ-carbide precipitation contributing the removal of carbon from solid solution as well the tendency of brittle fracture from shear localization and glide plane decohesion.

The mechanical properties of the aged specimens from Heat 1-A with 9% Al and 0.9% C are shown in Table 3 and compared with two steels of similar composition that were commercially cast with[26] and without[23] cerium addition in the form of misch metal. It is shown that the cerium treated steels have similar dynamic fracture toughness values of 160 kJ/m^2 and 140 $kJ.m^2$ when aged in the hardness range of 300 BHN. However, the commercially cast steel without cerium additions obtained more than twice the fracture toughness at an equivalent hardness level as shown in Table 3. These results appear to be

correlated to cerium treatment. In most cases, steels that were cerium treated contained more than twice the total inclusion density as the commercially cast steel without misch metal addition as shown in Table 3. Additionally, the commercially produced castings with cerium treatment contained topologically close packed silicides that are brittle and promote low energy ductile fracture.[26]

An attempt was made to model the effects of inclusion density, size, volume fraction, and spacing on the dynamic fracture toughness of the Fe-Mn-Al-C steels reported here. The fracture energy will be somewhat dependent on the size of the plastic zone and the type and distribution of second phase inclusions.[42] The plastic zone size increases with the applied stress and is controlled by the yield strength and fracture toughness. Crack propagation occurs when the plastic zone size equals the spacing of the second phase inclusions. Large plastic zones in front of the crack tip increase the chance of fracture taking place by direct linkup of voids during fibrous rupture of the matrix. The size of the plastic zone increases with decreasing yield strength and this correlates with an increase in toughness.[42] When inclusion spacings are large, the limited interaction between the plastic zones of the individual particles will permit large strains to occur before void coalescence and failure. Low energy ductile fracture is favorable if there is high density of voids or fractured particles with small spacings between them as observed in the solution treated specimen from Heat 3-C in Figure 3 (f). Broek[56] determined that larger inclusions with greater inclusion spacing produced considerable void growth before failure while smaller and closer spaced particles nucleated smaller voids, which grew quickly to failure. Broek[56] suggested that toughness would be expected to linearly increase with decreasing particle density. In addition, Deimel et al.

show that the toughness of high Cr and Mo pressure vessel steel was inversely proportional to the total inclusion density.[57] A plot of DFT vs total inclusion density as a function of heat treatment is given in Figure 13 (a) and shows a linear decrease in DFT as the total density of inclusions increases in solution treated specimens.

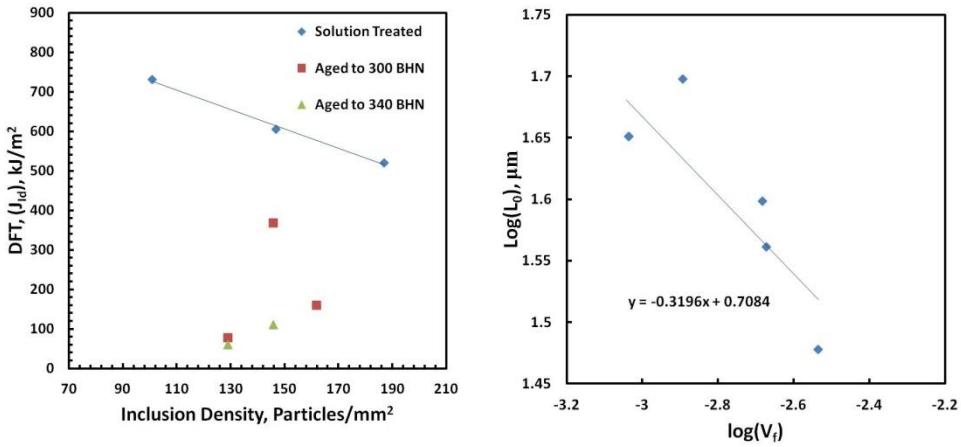

(a) (b)

Fig. 13 (a) Solution treated specimens show a decrease in toughness with increasing total inclusion density, however, aged specimens show no correlation between DFT and the total amount of inclusions. (b) Inclusion spacing decreased as the volume fraction of inclusions increased. The slope of the line gives a value of -0.32 which is comparable to the expected value of -0.33.[87,59]

However, aged specimens show no correlation between total inclusion density and DFT. The effect of inclusion diameter (D_0), spacing (L_0), and volume fraction (V_f) on the toughness of aluminum alloys was modeled by Hahn et al.[58,59] The model by Hahn et al. uses an ideal case consisting of a regular array of spherical particles with $L_0 = D_0 (\pi/6)^{1/3} V_f^{-1/3}$.

The fracture toughness was shown to fit the following model.

$$K_{IC} \sim V_f^{-1/6} [2(\pi/6)^{1/3} YE D_0]^{1/2} \quad (5)$$

Where Y is the tensile yield strength and E is Young's modulus. The relationship between inclusion spacing and the volume fraction of inclusions is given in Figure 13 (b) and shows and increase in particle spacing with decreasing volume fraction of inclusions. The slope of the regression line in Figure 13 (b) gives a value of -0.32 which is in agreement with the value of -0.33 given by Hahn et al.[58,59] To determine the relationship between toughness, volume fraction and inclusion diameter, K_{Id} was converted to an appropriate J_{Id} value by use of equation (3). Substituting equation (3) into (5) yields the following relationship between J_{Id} and the volume fraction of inclusions.

$$J_{Id} = V_f^{-1/3} [2 (\pi/6)^{1/3} YD_0] \quad (6)$$

Therefore toughness should be function of $V_f^{-1/3}$. Figure 14 (a) shows the dependence of dynamic fracture toughness on the volume fraction of inclusions as a function of heat treatment. The results show an excellent fit to the model for the solution treated specimens; however, aged specimens do not fit the model.

Fracture toughness (K_{Ic}) is a parabolic function of the inclusion spacing as given in the following relationship.[58]

$$K_{IC} \sim [2EYL_0]^{1/2} \quad (7)$$

Combining Equations (3) and (7) gives a linear relationship between J_{Id} and the average inclusion spacing.

$$J_{Id} \sim 2YL_0 \quad (8)$$

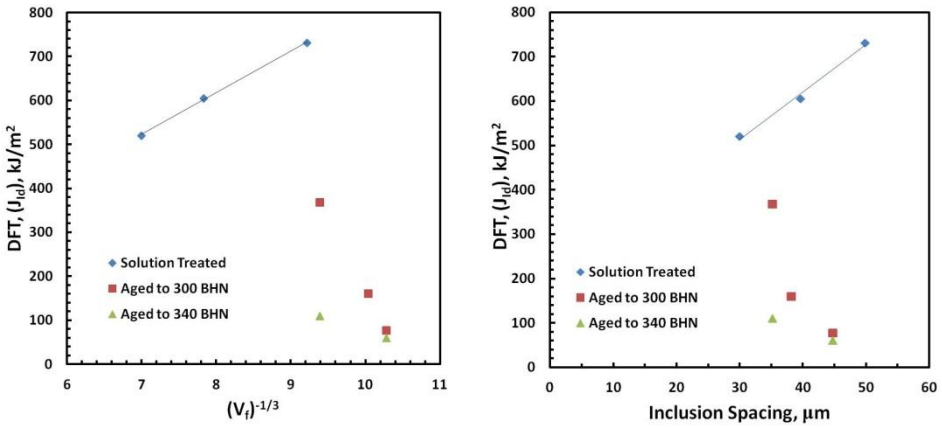

(a) (b)

Fig. 14 (a) Solution treated specimens show a linear relationship between DFT and $V_v^{-1/3}$ and (b) inclusion spacing, L_0. Aged specimens however, do not fit the model and show little correlation between the volume fraction and spacing of inclusions.

Figure 14 (b) shows the relationship between particle spacing and DFT. Again, the solution treated specimens are consistent with the model and show a linear relationship between increasing DFT and increasing inclusion spacing. However, aged specimens show no correlation with average inclusion spacing.

According to Equation (6) the relationship between D_0 and J_{Id} should also be linear. A plot of average inclusion diameter vs DFT for the high strength steels is shown in Figure 15 (a). Toughness was found to increase linearly with D_0 for solution treated specimens as well as aged specimens and results fit the model by Hahn et al.[58,59] Therefore for solution treated specimens, toughness was influenced by both carbon and aluminum content as well as total inclusion density. However, for aged specimens there is less of a correlation between toughness and total inclusion density. Notch toughness in Fe-Mn-Al-C steels has been shown by Schulte et al.[27] to be a function of AlN density. A plot of DFT vs AlN density for specimens aged in the hardness range of 300 BHN is shown in Figure 15 (b) for laboratory heats and commercial heats with similar

chemistries. Results show that the toughness in the aged specimens is a strong function of AlN content. Increasing the amount of AlN sharply reduced toughness when compared to the commercially cast steel without cerium additions.

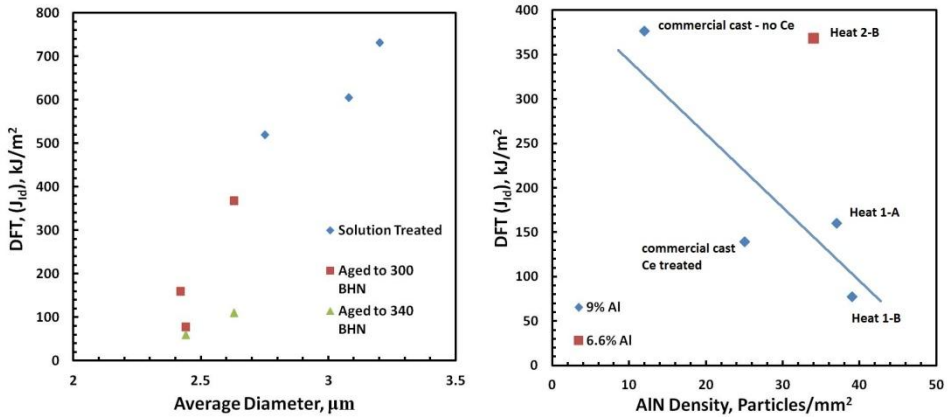

(a) (b)

Fig. 15 (a) Both solution treated and aged specimens show a linear relationship between DFT and the average inclusion diameter. (b) For specimens of the same nominal chemistry and age hardened in the range of 300 BHN, DFT is a strong function of the amount of AlN. It is shown that decreasing the amount of aluminum to 6.6% in age hardened specimens of equivalent hardness and AlN content increased the toughness by more than 200 kJ/m^2.

The toughness values of the aged specimens from laboratory heats are comparable to a value of 140 kJ/m^2 for a commercially cast and cerium treated alloy of the same nominal composition and aged to a similar hardness. The decrease in toughness observed in the cerium treated castings when compared to the commercially cast steel without cerium addition is directly related to the greater amount of AlN. The amount of AlN in the cerium treated castings was two or three times as great as the amount of AlN in the castings without cerium treatment, see Figure 8 (a). AlN in the commercially produced castings without cerium additions was mainly of the complex type and were coated with a

"shell" of MnO or MnS that heterogeneously nucleated on the AlN during solidification. In the cerium treated castings, the high chemical activity of cerium in the melt essentially tied up all of the S and O as complex rare earth inclusions. Although AlN was found in combination with rare earth inclusions, they did not form a shell around the AlN. The reduced toughness in the cerium treated castings is the result of a large population of un-coated AlN. The facetted nature of the un-coated AlN would be more efficient at causing large stress concentrations at the particle/matrix interface and therefore would lower the critical stress for void nucleation. Cerium additions restrict MnS and MnO formation and thus result in a larger percentage of AlN that is not coated with a protective oxide or sulfide shell leading to a reduction in toughness. However, if cerium addition is required for control of phosphorus, additions of 0.2 wt.% Ce or less should be made in the furnace to prevent the formation of brittle rare earth silicides.[26]

Dynamic fracture toughness of Fe-Mn-Al-C steel castings is therefore a complex combination of aluminum and carbon content as well as AlN content. In the solution treated condition, the addition of aluminum reduces the density while simultaneously increasing ductility; however, increasing aluminum additions promotes κ-carbide precipitation and a commensurate decrease in dynamic toughness in the age hardened condition. Carbon in solid solution increases both the work hardening capacity as well as the toughness whereas, increasing the amount of carbon in aged alloys produced a 80 kJ/m^2 decrease in toughness as shown in Table 2. For maximum toughness, these alloys should be used in the solution treated condition and aluminum additions should be kept to a minimum while simultaneously adding as much carbon in solid solution as possible without precipitating carbides. However, decreasing the amount of aluminum in these

steels negates their effectiveness as lightweight materials. A reasonable compromise can be formulated based upon the results reported here. A good combination of high strength and toughness is obtained with aluminum additions between 6 and 7% and carbon below 1.2% with a corresponding density reduction of 10 to 12%.[15] Aging the cerium treated alloy of this composition in the hardness range of 300 BHN was shown to produce a toughness of 368 kJ/m^2. It should be noted that this toughness is well above the trend line for the 9% aluminum materials in Figure 15 (d). Projecting along a similar trend line to lower AlN concentrations would predict an increase in toughness of nearly 200 kJ/m^2. It is therefore suggested that a clean casting of Fe-30Mn-7Al-1Si-1C-0.5Mo steel will produce a dynamic fracture toughness greater than 500 kJ/m^2 when aged to 300 BHN with as much as a 12% reduction in density when compared with traditional steels.

CONCLUSIONS

The dynamic fracture toughness of cerium treated Fe-Mn-Al-C castings was determined with respect to different aluminum and carbon additions. In the solution treated condition, increasing the amount of carbon in solution increased toughness by 130 kJ/m^2 and suppressed mechanical twining. Increasing the amount of aluminum in solution treated castings reduced the toughness by around 100 kJ.m^2. Evidence suggests that short range ordering of Fe-Al-C clusters promotes planar slip and glide plane softening and this effect is the major mechanism for the enhanced ductility in aluminum alloyed high manganese austenitic steels. Adding carbon in solution is believed to increase the number of Mn-C pairs and contributes to higher strain hardening while adding aluminum reduces the diffusivity of C in austenite and promotes short range ordering of Al and subsequent precipitation of the $E2_1$ κ-carbide structure. During age

hardening, carbon is removed from solution and this contributes to a reduction in toughness. In age hardened alloys the addition of carbon and aluminum produced a significant reduction in toughness and transitioned the fracture mode from ductile rupture to both intergranular and transgranular cleavage fracture. The transgranular cleavage fracture observed in aged specimens is suggested to be the result of glide plane decohesion produced by extensive planar slip and cracking within slip bands due to a high density of dislocations concentrated onto the slip plane. For solution treated specimens, toughness was a function of total inclusion density, size, and distribution. However, in aged specimens of the same nominal chemistry, toughness was a function of aluminum nitride content. Cerium treated castings contained a higher density of AlN and this reduced the toughness when compared to commercially produced castings without cerium treatment. However, at a constant carbon content of 1.2% C and for castings with a similar amount of AlN, decreasing the aluminum from 9% to 6.6% Al resulted in a 200 kJ/m^2 increase in dynamic fracture toughness. It is expected that limiting the amount of AlN to less than 13 particles/mm^2 while keeping the aluminum and carbon content between 6 and 7%, and 1 and 1.2%, respectively, will produce a dynamic fracture toughness greater than 500 kJ/m^2 in aged castings with a simultaneous reduction in density of 10 to 12% over traditional steel castings.

ACKNOWLEDGEMENTS

This work was supported in part by Army Research Laboratory under contracts from Battelle Memorial Institute (contract W911NF-07-D-0001) and Benet Laboratories (contract W15QKN-07-2-0004). Laura Bartlett was also supported by a U.S. Department of Education GAANN fellowship under contract P200A0900048. The FEI Tecnai F20 scanning/transmission electron microscope was obtained with a Major Research Instrumentation grant from NSF under contract DMR-0922851. The authors gratefully acknowledge Mr. Sam Buckholz for help with casting the alloys used in this study as well as Mr. Joey Brookshire and Mr. Zach Henderson for help with specimen preparation. Dr. Kai Song is also gratefully acknowledged for his help with operation of the transition electron microscope.

REFERENCES

1. Frommeyer, G. and Brux, U., "Microstructures and Mechanical Properties of High Strength Fe-Mn-Al-C Light-weight TRIPLEX Steels," *Steel Research Int.*, Vol. 77, pp. 627-633 (2006).

2. Howell, R.A., Weerasooriya, T. and Van Aken, D.C., "Tensile, High Strain Rate Compression and Microstructural Evaluation of Lightweight Age Hardenable Cast Fe-30Mn-9Al-XSi-0.9C-0.5Mo Steel," *AFS Trans*. Vol. 117, pp. 751-763 (2009).

3. Ham, J. L., Cairns, R. E., "Manganese Joins Aluminum to Give Strong Stainless," *Product Engineering*, Dec, pp. 51-52 (1958).

4. Brady, G.S., Clauser, H.R., "Manganese Aluminum Steel," Materials Handbook, 11th Ed., p. 497 (1977).

5. Acelrad, O., Pereira, L.C., Amaral, M.R., "Processing Condition, Microstructure and Strength of an Austenitic FeMnAlC Alloy," *Proceedings of Proc. And Prop. Of Mats*., pp. 829-834 (1992).

6. Kayak, G. L., *Met. Sc. And Heat Tr*., Vol. 11, pp. 95-97 (1969).

7. Howell, R. A., Lekakh, S. L., Van Aken, D. C., Richards, V. L., *AFS Transactions*, Vol. 116, pp. 867-878 (2008).

8. Sato, K., Igarashi, Y., Inoue, Y., Yamazaki, T., Yamanaka, M., "Microstructure and Age Hardening in Spinodally Decomposed Austenitic Fe-Mn-Al-C Alloys," *Proceedings of the International Conference on Stainless Steels* (1991).

9. Ishida, K., Ohtani, H., Naoya, S., Kainuma, R., Nishizawa, T., *ISIJ*, Vol. 30, pp. 680-686 (1990).

10. Han, K. H., Choo, W. K., Choi, D. Y., Hong, S. P., *TMS-AIME*, pp. 91-106 (1987).

11. Acselrad, O., Kalashnikov, I. S., Silva, E. M., Simao, R. A., Achete, C. A., Pereira, L. C., *Metallurgical and Materials Transactions A* , Vol. 33A, pp. 3569-3572 (2002).

12. Ikarashi, Y., Sato, T., Yamazaki, T., Inoue, Y., and Yamanaka, M., *Journal of Materials Science Letters*, Vol. 11, pp. 733-735 (1992).

13. Han, K.H., Yoon, J.C., and Choo, W.K., *Scripta Metallurgica*, Vol. 20, pp. 33-36 (1986).

14. L.N. Bartlett, A.M. Schulte, D.C. Van Aken, K.D. Peaslee, and R.A. Howell. "A Review of the Physical and Mechanical Properties of a High Strength and Lightweight FeMnAlC Steel." *in MS&T10: Steel Product Metallurgy and Applications*, pp.1941-1953, October 17-21, 2010 Houston, TX.

15. Howell, R.A., "Microstructural Influence on Dynamic Properties of Age Hardenable FeMnAl Alloys," *PhD dissertation, Missouri University of Science and Technology*, (2009).

16. T.L. Anderson. "Fracture Mechanics: Fundamentals and Applications, third edition". Taylor and Francis, New York, (2005).

17. ASTM E813-89, "Standard Test Method for Jic, a Measure of Fracture Toughness", ASTM Committee on Standards 1916 Race Street Philadelphia, PA 19103 (1989).

18. H.J. Schindler, "Estimation of the Dynamic J-R Curve from a Single Impact Bending Test". Mechanisms and Mechanics of Damage and Failure: proceedings of the 11th ECF. (1996).

19. ASTM E 1820-08 "Standard Test Method for Measurement of Fracture Toughness," ASTM Committee on Standards, 100 Barr Harbor Drive, PO Box C700, West Conshohocken, PA 1928-2959 (2008).

20. Bohme W. and Schindler H., "Single Specimen Methods to Evaluate J-R Curves from Instrumetned Charpy Tests: Results of a Round Robin," *Mechanisms and Mechanics of Damage and Failure, Proceeds of the 11th annual European Conference on Fracture* (1996).

21. G. Magudeeswaran, V. Balasubramanian, S. Sathyanarayanan, G. Reddy, A. Moitra, S. Venugopal, and G. Sasikala. "Dynamic Fracture Toughness Behavior of Armor-Grade Q&T Steel Weldments: Effect of Weld Metal Composition and Microstructure." *Met. Mater. Int.*, Vol. 15, No. 6, pp. 1017 – 1026 (2009).

22. Sreenivasan P.R., Shastry C.G., Mathew M.D., Rao K., and Mannan S.L., "Dynamic Fracture Toughenss and Charpy Transition Properties of a Serivce Exposed 2.25Cr-1Mo Reheater Header Pipe," *Journal of Engineering Materials and Technology*, Vol. 125 (2003).

23. Bartlett, L., Dash, A., Van Aken, D., Richards, V., and Peaslee, K., "Dynamic Fracture Toughness of High Strength Steels," *AFS Transactions*, 120, pp. 469-486 (2012).

24. O. Acelrad, J. Dille, L.C. Pereira, and J. Delplancke, "Room Temperature Cleavage Fracture of FeMnAlC Steels," *Met. Trans A*, Vol. 35A, pp. 3863-3866 (2004).

25. Bartlett, L., Van Aken, D., Peaslee, K., and Howell, R., "Effect of Phosphorus and Silicon on the Precipitation of k-carbides in the Fe-30Mn-9Al-XSi-0.9C-0.5Mo Alloy," *AFS Transactions*, 118, pp. 413-423 (2010).

26. Bartlett, L., Van Aken, D., Lekakh, S., and Peaslee, K., "Mechanical Properties of Cerium Treated Fe-Mn-Al-C Steel Castings," *AFS Transactions*, 119, pp. 545-560 (2011).

27. Schulte, A.M., Lekakh, S.N. , Van Aken, D.C., and Richards, V.L., "Phosphorus Mitigation in Cast Lightweight *Fe-Mn-Al-C* Steel," *AFS Trans*. 118, pp. 451- 463 (2010).

28. Grassel O, Frommeyer G, Derder C., and Hofmann, H., *Journal of Physics IV France* Vol. 7 p. 383 (1997)

29. Frommeyer G, Brux, U., and Neumann, P., "Supra-Ductile and High-Strength Manganese TRIP/TWIP Steels for High Energy Absorption Purposes," *ISIJ* Int. Vol. 43 p. 438 (2003).

30. Allain S, Chateau J, Bouaziz O, Migot S, and Guelton N. *Materials Science and Engineering* Vol. 387-389 p. 158 (2004).

31. Yoo, J., Hwang, S., and Park K., *Metallurgical and Materials Transactions A* Vol. 40 p.1520 (2009).

32. A. Dumay, J. Chateau, S. Allain, S. Migot, and O. Bouaziz, "Influence of Addition Elements on the Stacking Fault Energy and Mechanical Properties of an Austenitic Fe-Mn-C Steel," *Materials Science and Engineering A* Vol. 483 pp. 184-187 (2008).

33. Canadinc, D., Sheitoglu, H., Maier, H., and Chumlyyakov, Y., *Acta Mater*. Vol. 53 p. 1831 (2005).

34. Y. Dastur and W. Leslie, "Mechanism of Work Hardening in Hadfield Manganese Steel," *Metallurgical Transactions A*, Vol. 12 pp. 749-759 (1981).

35. H.K. Lai and C.M. Wan, "The Study of Work Hardening in Fe-Mn-Al-C Alloys," *Journal of Materials Science* Vol. 24 pp. 2449-2453 (1989).

36. M. Abbasi, S. Kheirandish, J. Kharrazi, and J. Hejazi, "The Fracture and Plastic Deformation of Aluminum Alloyed Hadfield Steels," *Materials Science and Engineering A* Vol. 513 pp. 72-76 (2009).

37. S.C. Chang and Y.H. Hsiau, "Tensile and Fatigue Properties of Fe-Mn-Al-C Alloys," *Journal of Materials Science* Vol. 24 pp. 117-1120 (1989).

38. J.F. Kalthoff, and M. Gregor. "Instrumented Impact Testing of Subsize Charpy V-notch Specimens". *Small Specimen Test Techniques*, ASTM STP 1329. (1998).

39. ASTM E 399-09 "Linear-Elastic Plane-Strain Fracture Toughness K_{Ic} of Metallic Materials," ASTM Committee on Standards, 100 Barr Harbor Drive, PO Box C700, West Conshohocken, PA 1928-2959 (2009).

40. Gebhardt, T., Music, D., Kossmann, D., Ekholm, M., Abrikosov, I., Vitos, L., and Schneider, J., "Elastic Properties of FCC Fe-Mn-X (X = Al, Si) Alloys Studied by Theory and Experiment," *Acta Materialia*, Vol. 59 pp. 3145-3155 (2011).

41. Buckholz, S.A., "The Influence of Aluminum and Carbon on the Abrasion Resistance of High Manganese Steels," Missouri University of Science and Technology, M.S. Thesis (2012).

42. T.H. Courtney. "Mechanical Behavior of Materials, second edition", Waveland Press, pp. 459 – 461. (2005).

43. Bouaziz, O. and Guelton, N., "Modelling of TWIP Effect on Work-hardening," *Materials Science and Engineering A* Vol. 319-321 pp. 246-249 (2001).

44. Park, K., Jin, K., Han, S., Hwang, S., Choi, K., and Lee, C., "Stacking Fault Energy and Plastic Deformation of Fully Austenitic High Manganese Steels: Effect of Al addition*," Materials Scinece and Engineering A* Vol. 527 pp. 3651-3661 (2010).

45. Gerold, V. and Karnthaler, H., "On the Origin of Planar Slip in FCC Alloys," *Acta Metall*. Vol. 37 pp. 2177-2183 (1989).

46. Shun, T., Wan, C., and Byrne, J., "A Study of Work Hardening in Austenitic Fe-Mn-C and Fe-Mn-Al-C Alloys," *Acta Metall. Mater.* Vol. 40 pp. 3407-3412 (1992).

47. Lee, S., Kim, J., Kane, S., and De Cooman, B., "On the Origen of Dynamic Strain Aging in Twinning Induced Plasticity Steels," *Acta Materialia* Vol. 59 pp. 6809-6819 (2011).

48. Hutchinson, B. and Ridley, N., "On Dislocation Accumulation and Work Hardening in Hadfield Steel," *Scripta Materialia* Vol. 55 pp. 299-302 (2006).

49. Zuidema, B., Subramanyam, D., and Leslie, W., "The Effect of Aluminum on the Work Hardening and Wear Resistance of Hadfield Manganese Steel," *Metallurgical and Materials Transactions A* Vol. 18 p. 1629 (1987).

50. Medvedeva,N.I., Park, M.S., Van Aken, D.C., and Medvedeva, J.E., "First-principles study of the Mn, Al and C distribution and their effect on the stacking fault energies in austenite," arXiv:1208.0310v1 [cond-mat.mtrl-sci], 2012.

51. Hwang, S., Ji, J., and Park, K., "Effects of Al Addition on High Strain Rate Deformation of Fully Austenitic High Mn Steels," *Materials Science and Engineering A* Vol. 528 pp. 7267-7275 (2011).

52. Tomota, Y., Xia, Y., and Inoue K., "Mechanism of Low Temperature Brittle Fracture in High Nitrogen Bearing Austenitic Steels," *Acta Meter*. Vol. 46 pp. 1577-1587 (1998).

53. Tobler, R. and Meyn, D., "Cleavage Like Fracture Along Slip Planes in Fe-18Cr-3Ni-13Mn-0.37N," *Metallurgical Transactions A* Vol. 19 p. 1626 (1988).

54. Tomota, Y., Nakano, J., Xia, Y., and Inoue, K., "Unusual Strain Rate Dependence of Low Temperature Fracture Behavior in High Nitrogen Bearing Austenitic Steels," *Acta Mater*. Vol. 46 pp. 3099-3108 (1998).

55. Ho, N., Chen, C., and Tjong, S., "Cyclic Softening of Age Hardened Fe-Mn-Al-C Alloys Containing Coherent Precipitates," *Scripta Metallurgica* Vol. 21 pp. 1319-1322 (1987).

56. D. Broek, "Engineering Fracture Mechanics", Pergamon Press (1973).

57. P. Deimel and E. Sattler, "Non-metallic Inclusions And Their Relation to the J-integral at Physical Crack Initiation for Different Steels and Weld Metals." *Journal of Materials Science,* Vol. 33. pp. 1723 – 1736 (1998).

58. G.T Hahn, M.F. Kanninen and A.R. Rosenfield,"Fracture toughness of materials", *Annual Review of Materials Science,* vol. 2, pp. 381-404 (1972).

59. G.T. Hahn and A.R. Rosenfield, "Metallurgical factors affecting fracture toughness of Aluminum alloys," *Met. Trans. A*, Vol. 6A pp. 653-667 (1975).

3. CONCLUSIONS

Silicon has been shown to increase the hardness of high manganese and aluminum steels during aging; however, until now the mechanism for this was not understood. Silicon has little effect on the size or volume fraction of κ-carbide precipitated, which was in agreement with first principles modeling. In addition, hardening was found not to be the result of manganese partitioning. Silicon was found to have no effect on the distribution of manganese and the κ-carbide was depleted of manganese regardless of silicon content. Silicon increased the activity of carbon in solution and increasing the silicon content from 0.59 to 1.56 wt.% was found to increase the partitioning of carbon in the κ-carbide from 5.2 to 6.6 at.%. The results of this study suggest that the increase in strength during aging of high manganese and aluminum steels is directly related to the increase in the compositional amplitude of carbon with silicon addition. The model predicts a 120 MPa increase in strength with a 1wt.% increase in silicon for alloys aged for 60 hrs at 530° C and this is in excellent agreement with previously determined mechanical property data.

Precipitation of κ-carbide was determined to form first by ordering of Fe-Al-C into the $E2_1$ structure and this was followed by spinodal decomposition involving mainly the diffusion of carbon along austenite <100>. Phosphorus was shown to increase the prevalence of the ordering into the $E2_1$ κ-carbide structure. Increasing the amount of phosphorus resulted in a dramatic increase in the concentration amplitude of carbon during aging when compared with low phosphorus specimens of equivalent composition and this was determined to be the mechanism behind the increase in the hardening rate with increasing phosphorus. However, long range diffusion of phosphorus was not

involved in the observed increase in the hardening rate and the phosphorus distribution was random. It is therefore suggested that phosphorus increases the initial ordering reaction and that this greatly accelerates the later stage of spinodal decomposition.

The dynamic fracture toughness of cerium treated Fe-Mn-Al-C castings was determined with respect to different aluminum and carbon additions. In the solution treated condition, increasing the amount of carbon in solution increased toughness by 130 kJ/m^2 and suppressed mechanical twining. Increasing the amount of aluminum in solution treated castings reduced the toughness by about 100 $kJ.m^2$. Evidence suggests that short range ordering of Fe-Al-C clusters promotes planar slip and glide plane softening and this effect is the major mechanism for the enhanced ductility in aluminum alloyed high manganese austenitic steels. Adding carbon in solution is believed to increase the number of Mn-C pairs and contributes to higher strain hardening while adding aluminum reduces the diffusivity of C in austenite and promotes short range ordering of Al and subsequent precipitation of the $E2_1$ κ-carbide structure. During age hardening, carbon is removed from solution and this contributes to a reduction in toughness. In age hardened alloys the addition of carbon and aluminum produced a significant reduction in toughness and transitioned the fracture mode from ductile rupture to both intergranular and transgranular cleavage fracture. The transgranular cleavage fracture observed in aged specimens is suggested to be the result of glide plane decohesion produced by extensive planar slip and cracking within slip bands due to a high density of dislocations concentrated onto the slip plane.

4. SUGGESTED FUTURE STUDIES

In current study, an Avrami approach was used to model transformation kinetics (Paper 1) in a Fe-30Mn-9Al-0.9C-0.5Mo steel. Assumptions of the Avrami model include: nucleation and growth occur simultaneously throughout transformation, nucleation is homogeneous, a constant nucleation rate, a constant growth rate, and that the transformation product grows as a sphere. The Avrami approach has been used to accurately model the kinetics of a variety of different transformations despite the fact that most real systems can deviate significantly from these assumptions. Avrami kinetic modeling of Fe-Mn-Al-C alloys suggested that increasing the amount of phosphorus from 0.001 to 0.018% P and greater decreased the activation energy for homogeneous nucleation of κ-carbide from 300 kJ/mol to 180 kJ/mol. The activation energies for κ-carbide precipitation and growth were compared with values of 183 kJ/mol for the interdiffusion of phosphorus in austenitic iron (950 to 1250°C), 235 kJ/mol for the diffusion of aluminum in austenitic iron, and activation energies of between 120 and 150 kJ/mol for the diffusion of carbon in austenite (750 to 1300°C).[22,64] Thus, in the higher phosphorus alloys, it was suggested that phosphorus increased the kinetics of the initial spinodal decomposition and later stages of growth and that this was related mainly to the diffusion of phosphorus and carbon. Subsequent investigations utilizing local electrode 3-D atom probe (LEAP) tomography and TEM (Paper 3) have shown that the formation of κ-carbide occurs via concurrent ordering and spinodal decomposition and that the distribution of phosphorus is homogeneous between the κ-carbide and austenite and therefore long range diffusion of phosphorus is not involved and hardening during aging is the result of an increase in the strain amplitude as the concentration amplitude of

carbon increases during spinodal decomposition. Additionally, TEM observations show a high number density of ordered domains corresponding to the $E2_1$ κ-carbide structure that with time coalesce into cuboidal particles aligned along elastically soft <100> directions in the austenite matrix. These results suggest that the volume fraction of κ-carbide is set during the early stages of transformation and that the kinetics may be more accurately modeled using a coarsening model involving volume diffusion of mainly carbon. In fact, for diffuse transformations such as in spinodally decomposing systems, there is often no energy barrier to nucleation in framework of classical nucleation and growth theory as modeled by the Avrami approach. Sato et al.[22] studied the kinetics of the growth of the wavelength of spinodal decomposition in a Fe-30Mn-9Al-0.9C (0.016P) alloy utilizing XRD and electron diffraction. The growth of the wavelength of the modulated structure during spinodal decomposition was shown to fit a coarsening model according to the following.

$$\lambda^n - \lambda_0^n = kt \qquad (1)$$

Where λ_0 is the initial wavelength and λ is the wavelength at a time t.

Coarsening of the spinodally decomposing structure should have an Arrhenius relationship with temperature corresponding to the following relationship.

$$\lambda = \mathrm{At}\exp\frac{-\mathrm{Q}}{\mathrm{RT}} \qquad (2)$$

Where A is a constant, t is time, Q is the activation energy for coarsening, and T is temperature. Future studies will use a combination of resistivity measurements and x-ray diffraction experiments to model kinetics of κ-carbide precipitation in Fe-Mn-Al-C alloys with respect to silicon and phosphorus. Additionally, Fourier transforms of the full LEAP reconstructions will be used in combination with phase field modeling and experimental results to further advance the knowledge of phase transformations in Fe-Mn-Al-C steels.

APPENDIX: DYNAMIC FRACTURE TOUGHNESS CALCULATIONS

The following is a calculation procedure developed by Schindler[54] to determine the dynamic J-R curve using a single specimen technique. Table A1 lists the required experimental parameters in reference to the DFT test specimen shown in Figure A1.

Table A1. Experimental parameters used in the Schindler[54] method for calculating DFT

Term	**Discription**	**Units**
W	Specimen width	mm
b_0	Unbroken ligament	mm
a_0	Initial crack size	mm
B	Specimen thickness	mm
η	Shape factor	none
Δa_m	Crack extension at max load	mm
E_{max}	Energy consumed at max load	J
E_{tot}	Total energy	J
F_{max}	Max force	N

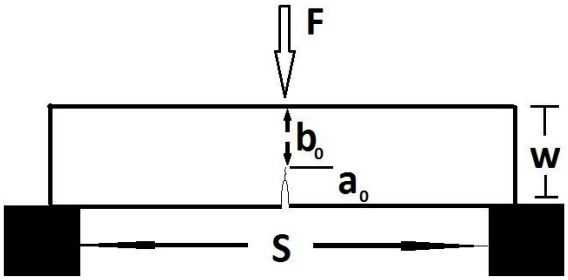

Figure A1. The geometry of the DFT specimen as per the Shindler[4] method consists of a Charpy-type test bar which has been fatigue pre-cracked in three point bending.

Phase I of the J-R curve is called the J controlled region and is limited to $\Delta a<\Delta a_m$. Phase I includes the beginning of loading, crack tip blunting, crack initiation, and first stage propagation. Phase I is calculated by the power-law relationship as given in Equation (1). In Equation (1) *C* and *p* are material dependent parameters and $\Delta a<\Delta a_m$.

$$J(\Delta a) = C \cdot \Delta a^p \qquad (1)$$

Phase II is essentially stable tearing or crack growth and is governed by the crack tip opening angle, CTOA, which is assumed to be constant. The Phase II portion of the J-R curve is given by the following relationship.

$$J(\Delta a) = J_{mp} + s_2 \left[(\Delta a - \Delta a_m) - \frac{(\Delta a - \Delta a_m)^2}{2b_0}\right] \qquad (2)$$

where J_{mp} is analogous to the plastic contribution of J evaluated at maximum load as given by Equation (3) and s_2 is a material parameter given by Equation (4). For a complete derivation of these equations, one should consult Schindler[54]

$$J_{mp} = \frac{\eta \cdot E_{max}}{B \cdot b_0} \qquad (3)$$

$$s_2 = \frac{2 \cdot \eta \cdot (E_{tot} - E_{max})}{B \cdot (b_0 - \Delta a_m)^2} \qquad (4)$$

In the former equations, η is a shape factor that is dependent on the specimen geometry and initial crack size. For deeply cracked specimens, η is given by the following relationship.

$$\eta\left(\frac{a_0}{W}\right) = 1.90 + 0.138\frac{a_0}{W} \quad \text{for } 0.275 < \frac{a_0}{W} < 1 \qquad (5)$$

The material parameters *C*, Δa_m, and *p* depend on the experimental energy inputs obtained from the instrumented load vs. displacement curve and are calculated according to Equations (6), (7), and (8).

$$C = \left(\frac{2}{p}\right)^p \cdot \frac{\eta}{B(W-a_0)^{1+p}} \cdot E_{tot}^{p} \cdot E_{max}^{1-p} \qquad (6)$$

$$\Delta a_m = \frac{E_{max} \cdot p \cdot b_0}{2 \cdot E_{tot}} \qquad (7)$$

$$p = \frac{3}{4} \cdot \left[1 + \frac{E_{max}}{E_{tot}}\right]^{-1} \qquad (8)$$

The resulting equations for phase I and II are plotted verses crack extension to obtain the required J-R curve. The dynamic fracture toughness is then determined from the calculated curve using a 0.2 mm offset method similar to the evaluation of the quasistatic case given in ASTM E813. The intersection of the 0.2 mm offset line and the calculated J-R curve gives the value of J_{1d}. The slope of the line, s_1, is given by Equation (9) which is equivalent to three times the dynamic flow stress, $3\sigma_{fd}$.

$$s_1 = 3 \cdot \frac{F_{max} \cdot S}{b_0 \cdot B} \qquad (9)$$

BIBLIOGRAPHY

1. R. Howell, T. Weerasooriya, and D. Van Aken, Tensile, High Strain Rate Compression and Microstructural Evaluation of Lightweight Age Hardenable Cast Fe-30Mn-9Al-XSi-0.9C-0.5Mo Steel, *Transactions of the American Foundry Society*, (2008).

2. Howell, R. A., Lekakh, S. L., Van Aken, D. C., Richards, V. L.,"The Effect of Silicon Content on the Fluidity and Microstructure of Fe-Mn-Al-C Alloys," *AFS Transactions*, Vol. 116, pp. 867-878 (2008)

3. Acselrad, O., Kalashnikov, I. S., Silva, E. M., Simao, R. A., Achete, C. A., Pereira, L. C., *Metallurgical and Materials Transactions A* , Vol. 33A, pp. 3569-3572 (2002).

4. L. Bartlett, R.A. Howell, A. Schulte, D. Van Aken, and K. Peaslee, "A Review of the Physical and Mechanical Properties of a Cast High Strength and Lightweight *Fe-Mn-Al-C* Steel," MS&T 2010 Conference Proceedings

5. Seol, J., Raabe, D., Choi, P., Park, H., Kwak, J., and Park, C., "Direct evidence for the formation of ordered carbides in a ferrite based low density Fe-Mn-Al-C alloy studied by transmission electron microscopy and atom probe tomography," Submitted to Scripta Materialia, (2012).

6. O. Acselrad, I.S. Kalashnikov, E.M. Silva, M.S. Khadyev, and R.A. Simao, "Diagram of Phase Transformations in the Austenite of Hardened Alloy Fe-28Mn-8.5Al-1C-1.25Si as a result of Aging Due to Isothermal Heating", *Metal Science and Heat Treatment* Vol. 48, pp. 543-553 (2006).

7. Howell, R.A., "Microstructural Influence on Dynamic Behavior of Age Hardenable FeMnAl Steel Alloys" Ph.D. Dissertation (2009).

8. Medvedeva, N.I., Howell, R.A., Van Aken, D.C., and Medvedeva, J.E. "Effect of Phosphorus on Cleavage Fracture in κ-carbide," Physical Review B. Vol. 81, p. 012105 (2010).

9. H.K. Lai and C.M. Wan, "The Study of Work Hardening in Fe-Mn-Al-C Alloys," *Journal of Materials Science* Vol. 24 pp. 2449-2453 (1989).

10. M. Abbasi, S. Kheirandish, J. Kharrazi, and J. Hejazi, "The Fracture and Plastic Deformation of Aluminum Alloyed Hadfield Steels," *Materials Science and Engineering A* Vol. 513 pp. 72-76 (2009).

11. S.C. Chang and Y.H. Hsiau, "Tensile and Fatigue Properties of Fe-Mn-Al-C Alloys," *Journal of Materials Science* Vol. 24 pp. 117-1120 (1989).

12. O. Acelrad, J. Dille, L.C. Pereira, and J. Delplancke, "Room Temperature Cleavage Fracture of FeMnAlC Steels," *Met. Trans A*, Vol. 35A, pp. 3863-3866 (2004).

13. J. Ham and R. Cairns, "Manganese Joins Aluminum to Give Strong Stainless," *Product Engineering*, Dec, pp. 51-52 (1958).

14. G. Frommeyer and U. Brux, "Microstructures and Mechanical Properties of High-Strength Fe-Mn-Al-C Light-Weight TRIPLEX Steels," *Steel Research Int*., Vol. 77, pp. 627-633 (2006).

15. I. Kalashnikov, O, Acselrad, A. Shalkevich, L. Chumokova, and L. Pereira, "Heat Treatment and Thermal Stability of FeMnAlC Alloys," *Journal of Materials Processing Technology*, vol 136, pp. 72-79 (2003).

16. G. Kayak, Fe-Mn-Al Precipitation-Hardening Austenitic Alloys, *Met. Sc. And Heat Tr*., Vol. 11, pp. 95-97 (1969).

17. O. Acselrad, L. Pereira, and M. Amaral, "Processing Conditions, Microstructure and Strength of an Austenitic FeMnAlC alloy," *The Processing, Properties and Applications of Metallic and Ceramic Materials*, 09-07 pp. 829-834 (1992).

18. Y. Sutou, N. Kamiya, R. Umino, I. Ohnuma, and K. Ishida, "High-strength Fe-20Mn-Al-C Based Alloys with Low Density," *ISIJ International*, vol 50, pp. 893-899 (2010).

19. Hale, G. E., Baker, A. J., "Carbide Precipitation in Austenitic Fe-Mn-Al-C Alloys," *Conf. on Alt. Alloying for Env. Res.* New Orleans, LA., (1986).

20. Kimura, Y., Handa, K., Hayashi, K., and Mishima, Y., Intermetallics, vol 12, pp. 607-617 (2004).

21. Sato, K., Tagawa, K., and Inoue, Y., "Modulated Structure and Magnetic Properties of Age-hardenable Fe-Mn-Al-C Alloys," *Met. Trans A*, vol. 21A, pp 5-11 (1990).

22. Sato, K., Igarashi, Y., Inoue, Y., Yamazaki, T. and Yamanaka, M., "Microstructure and age hardening in spiodally decomposed austenitic femnalc alloys," Proceedings of the international conference on stainless steels, pp. 503-509 (1991).

23. Goretskii, G. P., Gorev, K. V., "Phase Equilibria in Fe-Mn-Al-C Alloys," Russian Met., Vol. 2, pp. 217-221 (1990).

24. James, P. J., "Precipitation of the carbide $(Fe,Mn)_3AlC$ in an Fe-Al Alloy," J. Iron and Steel Inst., Jan, pp. 54-57 (1969).

25. Han, K. H., Choo, W. K., Choi, D. Y., Hong, S. P., "Age Hardening in Fe-Mn-Al-C Austenitic Alloys," TMS-AIME, pp. 91-106 (1987).

26. Choo, W. K., Kim, J. H., "Microstructural and Mechanical Property Changes on Precipitation of Intermetallic κ' Cubic Carbide Phase in the Fe-Mn(Ni)-Al-C Solid Solution," Conf. on Thermo-mechanical Process. of Steels and Other Mats., pp. 1631-1637 (1997).

27. Han, K.H., Yoon, J.C., and Choo, W.K., *Scripta Metallurgica*, vol 20, pp. 33-36 (1986)

28. Han, K. H., Choo, W. K., "Phase Decomposition of Rapidly Solidified Fe-Mn-Al-C Austenitic Alloy," Met. Trans. A., Vol. 20A, pp. 205-214 (1989).

29. Choo, W., Kim, J., and Yoon, J., "microstructural change in asuteitic Fe-30Mn-7.8Al-1.3C initiated by spinodal decomposition and its influence on mechanical properties," Acta mater. Vol. 45, pp. 4877-4885 (1997).

30. Park, K., Kwang, J., Han, S., Hwang, S., Choi, K., and Lee, C., "Stacking Fault Energy and Plastic Deformation of Fully Austenitic High Manganese Steels: Effect of Al addition," Materials Science and Engineering A, Vol 527. pp. 3651-3661 (2010).

31. Karakishev S. and Kalashnikov, I., "Short range ordering of aluminum atoms in the austenite lattice of steel 90G29Yu9MVB," Phys. Met. Metall. Vol. 62, pp. 187-190 (1986).

32. Medvedeva,N.I., Park, M.S., Van Aken, D.C., and Medvedeva, J.E., "First-principles study of the Mn, Al and C distribution and their effect on the stacking fault energies in austenite," arXiv:1208.0310v1 [cond-mat.mtrl-sci], (2012).

33. Prodhan, A., and Chakrabarti, K., "A study on age hardening in cast Fe-Mn-Al-Si-C alloys," Journal of Materials Science Vol. 25 pp. 1856-1862 (1990).

34. Sato, K., Tagawa, K. and Inoue, "Spinodal decomposition and mechanical properties of an austenitic Fe-30Mn-9Al-0.9C alloy" Materials Science and Engineering A 111 pp. 45-50 (1989).

35. Kato, M., Mori, T., and Schwartz, L., "Hardening by Spinodal Modulated Structure," Acta Metallurgica Vol. 28. Pp. 285-290 (1980).

36. Chao, C. Hwang, C. and Liu, T., "Grain boundary precipitation in an Fe-7.8Al-31.7Mn-0.54C alloy," Scripta Metal. et Mat. Vol. 28, pp. 109-114 (1993).

37. Tan J., Lin J., Yang W., and Liu T., "Phase transformations in an Fe-10Al-30Mn-1.2Si-0.5C alloy," Annual Conf. of the Chinese Soc. For Mat. Sci.

38. Chu, S., Kao, P., and Gan, D., "growth kinetics of k-carbide particles in Fe-30Mn-10Al-1C-1Si alloy," Scripta Met. Vol. 26, pp. 1067-1070 (1992).

39. C.Y. Chao and T.F. Liu, "Grain Boundary Precipitation in an Fe-28.6Mn-9.8Al-0.8Si-1.0C Alloy", Scripta Metallurgica, Vol. 25 pp. 1623-1628 (1991).

40. Hwang, C., Chao, C., Liu, T., "Grain boundary precipitation in a Fe-8Al-31.5Mn-1.05C alloy," Scripta Met. et Mat. Vol. 28, pp. 263-268 (1993).

41. Dumay, A., J. Chateau, S. Allain, S. Mingot, and O. Bouaziz, "Influence of addition elements on the stacking fault energy and mechanical properties of and austenitic Fe-Mn-C steel," Materials Science and Engineering A, 483-484 pp. 184-187 (2008).

42. S. Allain, J. Chateau, O. Bouaziz, S. Migot, and N. Guelton, "Correlations between the calculated stacking fauld energy and plasticity mechanisms in Fe-Mn-C alloys," Materials Science and Engineering A 387-389 pp 158-162 (2004).

43. O. Grassel, L. Kruge, G. Frommeyer, L. Meyer, Int. J. Plast. 16 pp. 1391-1409 (2000).

44. X. Tian, R. Tian, and Y. Zhang, "Effect of Al Content on Work Hardening in Austenitic Fe-Mn-Al-C Alloys" Canadian Metallurgical Quarterly, Vol 43, No 2 pp 183-192 (2004).

45. J.D. Yoo and K.T. Park, Materials Science and Engineering A 496 pp. 417-424 (2008).

46. B. Zuidema, D. Subramanyam, and W. Leslie, "The effect of aluminum on the work hardening and wear resistance of hadfield manganese steel," Metallurgical Transactions A Vol. 18 pp. 1629-1639 (1987).

47. B. Hutchinson and N. Ridley, "On dislocation accumulation and work hardening in Hadfield steel," Scripta Materialia 55 pp. 299-302 (2006).

48. Y. Dastur and W. Leslie, "Mechanism of Work Hardening in Hadfield Manganese Steel," Metall. Trans. A, vol. 12A, pp. 749 – 759 (1981).

49. Schulte, A., Lekakh, S., Van Aken, D., and Richards, V., "Phosphorus Mitigation in Cast Lightweight Fe-Mn-Al-C Steel," Transzctions of the American Foundry Society, (2010).

50. Bartlett, L., Van Aken, D., Lekakh, S., and Peaslee, K., "Mechanical Properties of Cerium Treated Fe-Mn-Al-C Steel Castings," *AFS Transactions*, 119, pp. 545-560 (2011).

51. T.L. Anderson. "Fracture Mechanics: Fundamentals and Applications, third edition". Taylor and Francis, New York, 2005.

52. ASTM E813-89, Standard Test Method for J_{IC}, a Measure of Fracture Toughness.

53. ASTM E 1820. Standard Test Method for Measurement of Fracture Toughness.

54. H.J. Schindler, "Estimation of the Dynamic J-R Curve from a Single Impact Bending Test". *Mechanisms and Mechanics of Damage and Failure: proceedings of the 11th ECF*. (1996)

55. M. Gintalas, A. Ziliukas, and K. Kalnins, "Dynamic J-integral Evaluation of Three-point-bend Beams with Various Geometrical Dimensions," Key Engineering Materials Vol. 488-489 pp 630-633 (2012).

56. S. Sathyanarayanan, G. Sasikala, S. Ray, "Evaluation of Dynamic Fracture Toughness of Cold Worked 9Cr-1Mo Steel," International Journal of Presure Vessels and Piping, 81 pp. 419-425 (2004).

57. P. Sreenivasan, C. Shastry, M. Mathew, K. Rao, S. Mannan, "Dynamic Fracture Toughness and Charpy Transition Properties of a Service Exposed 2.25Cr-1Mo Reheater Header Pipe," Journal od Engineering Materials and Technology, Vol. 125 pp. 227-233.

58. G. Magudeeswaran, S. Sathyanarayanan, G. Reddy, A. Moitra, S. Venugopal, G. Sasikala, and V. Balasubramanian, "Effect of Welding Consumables and Processes on Dynamic Fracture Toughness of Armor Grade Q&T Steel Joints," Iron and Steelmaking Vol. 36 pp. 50-61 (2009).

59. P. Mullner, C. Solenthaler, P. Uggowitzer, and M. Speidel, "Brittle Fracture in Austenitic Steel," Acta Metall. Mater. Vol. 42, No. 7, pp. 2211-2217 (1994).

60. J. Ishizaka, K. Orita, and K. Terao, J. Iron Steel Inst. Japan Vol. 78, p. 1846 (1992).

61. Y. Tomota, Y. Xia, and K. Inoue, "Mechanism of Low Temperature Brittle Fracture in High Nitrogen Bearing Austenitic Steels," Acta Mater. Vol. 46, No. 5, pp. 1577-1587 (1998).

62. Y. Tomota, J. Nakano, Y. Xia, and K. Inoue, "Unusual Strain Rate Dependence of Low Temperature Fracture Behavior in High Nitrogen Bearing Austenitic Steels," Acta Mater. Vol. 46, No. 9, pp. 3099-3108 (1998).

63. R. Tobler and D. Meyn, "Cleavage-Like Fracture Along Slip Planes in Fe-18Cr-3Ni-13Mn-0.37N Austenitic Stainless Steel at Liquid Helium Temperature," Metallurgical Transactions A, Vol. 19, pp. 1626-1631, (1988).

64. Gruzin, P.L. and Mural, V.V., Phys. Metals Meatallog. Vol 16, No 4, pp. 50 (1963)

VITA

Laura Nicole Bartlett was born on February 26, 1975 in Hayti, Missouri. She attended the University of Missouri at Rolla from 1994 to 1998 and from 2005 to 2008 and received a B.S. in Metallurgical Engineering (Dec. 2008). Upon graduation, she attended Missouri University of Scinece and Technology in January 2009 studing development of high strength and lightweight steel for high energy absorbing applications. In 2010 she was awarded a G.A.A.N.N. fellowship from the U.S. Department of Education to continue her studies as a Ph.D. candidate. She received her Ph.D. in Metallurgical Engineering from Missouri University of Science and Technology in May 2013 under Dr. David C. Van Aken.